



SUCHE NACH ANOMALER  
PRODUKTION VON TOP-QUARKS  
IN DER REAKTION  $u + g \rightarrow t$  MIT  
DEM CDF EXPERIMENT

ADONIS PAPAICONOMOU

DIPLOMARBEIT

*bei Prof. Dr. Th. Müller  
Institut für Experimentelle Kernphysik*

*Korreferent Prof. Dr. M. Feindt  
Institut für Experimentelle Kernphysik*

AN DER FAKULTÄT FÜR PHYSIK  
DER UNIVERSITÄT KARLSRUHE

12. JANUAR 2005

# Zusammenfassung

Das Standard Modell ist bisher der erfolgreichste Versuch der Elementarteilchenphysik eine Theorie zur Beschreibung der Natur zu erstellen. Es berücksichtigt drei der vier fundamentalen Kräfte, die elektromagnetische Kraft, die schwache und die starke Kernkraft und macht Aussagen über die Wechselwirkung derer Träger miteinander. Die vierte Kraft, die Gravitation, konnte bisher nicht in diesem Modell eingebaut werden und tritt allein in einer anderen Theorie auf, der Allgemeinen Relativitätstheorie. Bis zu diesem Zeitpunkt hat sich das Standard Modell in diversen Experimenten weltweit gut bewährt und hat zusätzlich Vorhersagen getroffen, die später experimentell bestätigt wurden. Jedoch gibt es etliche Fragen, die das Standard Modell nicht im Stande ist zu beantworten, was darauf hinweist, dass es eine Erweiterung oder eine komplett neue Theorie geben kann.

Im Jahr 1995 wurde am Tevatron-Beschleuniger das Standard Modell erneut bestätigt, in dem das Top-Quark nach einer langen Suche entdeckt wurde. Nach der Modellvorhersage sollte dieses Elementarteilchen der Partner des zu dieser Zeit schon entdeckten Bottom-Quarks in der dritten Generation der Fermionen (Materie-Teilchen) sein. Überraschenderweise war die Masse des Top-Quarks viel grösser als zuerst vermutet ( $m_t \simeq 175 \text{ GeV}$ ), ca. 35 mal die Masse des Bottom-Quarks. Somit ist die Top-Quark-Masse von der gleichen Grössenordnung wie die Skala der Elektroschwachen Symmetriebrechung ( $v = 246 \text{ GeV}$ ). Unterhalb dieser Energieschwelle sind die elektromagnetische Wechselwirkung von der schwachen Wechselwirkung entkoppelt. Diese Feststellung führt dazu, dass der Top-Quark-Sektor als Test für die Erzeugung der Massen von Eichbosonen dienen kann.

Das Top-Quark wird im Standard Modell entweder durch die starke oder durch die schwache Wechselwirkung produziert. Der Mechanismus im ersten Fall wird Paar-Produktion genannt, da das Top-Quark dadurch mit seinem Anti-Teilchen erzeugt wird. Im Fall der schwachen Produktion wird das Top-Quark (oder das Anti-Top-Quark) allein erzeugt, deswegen heisst der Prozess Einzel-Top Produktion. Das Standard Modell beinhaltet also nicht die Möglichkeit, dass ein Einzel-Top-Quark durch die starke Wechselwirkung produziert wird. Das wäre mittels einer Art von Wechselwirkungen möglich, genannt *Flavor*-ändernde Neutrale Ströme (FCNC), die aber im Standard Modell nicht in führender Ordnung vorkommen. Sie tauchen auf nur in höheren Ordnungen durch Strahlungskorrekturen. Da FCNC Prozesse im Standard Modell unterdrückt und ihre Effekte minimal erwartet werden, würden grosse detektierte FCNC Effekte ein Mittel sein, um neue Physik zu studieren. Nach theoretischen Erwartungen könnten solche 'anomale' FCNC Kopplungen eine signifikante Rolle in diversen Theorien spielen, die eine Erweiterung zum SM darstellen. Die Super-Symmetrie (SUSY) ist ein Beispiel einer möglichen Erweiterung. In Proton-Antiproton-Kollisionen, gemessen mit dem CDF-Experiment am Tevatron-Speicherring, kann man nur versuchen eine obere Grenze auf den Wirkungsquerschnitt solcher FCNC Prozesse zu setzen, da deren Effekte sehr klein sind, um mit grosser Effizienz detektiert zu werden. Die Beiträge der anomalen FCNC Kopplungen könnten aber theoretisch in zukünftigen Teilchenbeschleuniger (z.B. am LHC)

## II

gemessen werden.

Im Rahmen dieser Diplomarbeit wird ein spezieller FCNC Top-Quark-Produktionsprozess studiert. Es handelt sich um die Top-Up-Gluon Kopplung ( $t$ - $u$ - $g$ ). In diesem Szenario wird ein s-Kanal Top-Quark produziert, in dem ein Up-Quark und ein Gluon aus den kollidierenden Protonen/Anti-Protonen miteinander wechselwirken. Nach der Produktion zerfällt das Top-Quark und die Zerfallsprodukte können detektiert werden. Damit man die Kopplungsstärke des anomalen Prozesses messen kann, muss man erst die neue Produktionsmoden in die Theorie einbauen. Da es sich um eine starke Wechselwirkung handelt, muss man die QCD-Lagrange-Terme des SMs geeignet modifizieren. Mit diesem Trick erhalten wir eine effektive Theorie, die nur bis zu einer bestimmten Energieskala gültig ist. Somit brauchen wir keine komplett neue Theorie zu erstellen. Man muss doch dabei berücksichtigen, dass mit einer solchen Änderung der Phasenraum einen weiteren Zerfallskanal für das Top-Quark erlaubt. Da wir nur den SM-Zerfall ( $t \rightarrow Wb$ ) anschauen, wählen wir die Kopplungsstärke  $\kappa_u$  in einem Bereich, in dem der zusätzliche Zerfallskanal von geringer Bedeutung ist. Somit besteht unsere Signalsignatur aus einem Bottom-Quark Jet, einem Lepton und fehlender Energie (Neutrino). Das Lepton und das entsprechende Neutrino stammen von dem Zerfall des W-Bosons.

Das Hauptziel dieser Analyse ist eine obere Grenze auf den Wirkungsquerschnitt der anomalen Top-Quark Produktion im Kanal  $u + g \rightarrow t$  zu setzen. Anhand von dem erhaltenen Ergebnis wird die Möglichkeit gegeben, eine obere Grenze auf die Kopplungsstärke  $\kappa_u$  in einer zukünftigen Analyse zu setzen.

Diese Diplomarbeit besteht aus 5 Kapiteln. Am Ende der Arbeit gibt es einen Anhang mit relevanten Informationen.

Kapitel 1 beschäftigt sich mit dem theoretischen Hintergrund und erklärt die Motivation für diese Analyse. Das Standard Modell der Teilchenphysik wird am Anfang des Kapitels kurz vorgestellt. Einige der Schwächen des SMs werden dann angesprochen. Im Unterkapitel 1.3 wird auf die Top-Quark Produktion eingegangen. Erst wird die SM Version der Top-Quark Produktion diskutiert und dann folgt die Beschreibung des anomalen Kanals. Auf Grund der schweren Top-Quark Masse wird argumentiert, dass man die Studie solcher Anomalien im Top-Quark Sektor als Suche nach neuer Physik deuten kann. Am Ende des Kapitels wird eine Methode gezeigt, um die anomale Produktion  $u + g \rightarrow t$  in eine effektive Theorie unter Modifikation der QCD-Terme des SMs einzubauen. Es handelt sich um eine Theorie, die nicht fundamental, sondern nur bis zu einer bestimmten Energieskala gültig ist. Anhand der oben erwähnten Modifikationen ergeben sich entsprechend modifizierte Ausdrücke für die Zerfallsbreite, das Matrixelement und den Wirkungsquerschnitt der direkten Top-Quark Produktion. Das Kapitel endet mit einer Diskussion über die theoretisch optimalen Bedingungen, anomale FCNC Prozesse im Top-Quark Sektor zu untersuchen. Der im modifizierten QCD-Lagrange-Term auftauchende Faktor  $\kappa_u/\Lambda$ , der die Kopplungsstärke  $\kappa_u$  der Anomalie beinhaltet, wird nach diesen Überlegungen besser im Produktionskanal des Top-Quarks als in den Zerfallsmoden zu messen sein. In dieser Studie, wird der spezielle Wertebereich  $\kappa/\Lambda \lesssim 0.2 \text{ TeV}^{-1}$  gewählt, da nach theoretischen Vorhersagen die anomale Top-Quark Produktion somit messbar ist, im Gegensatz zum anomalen Zerfall, der gegenüber dem SM Zerfall unterdrückt ist. Infolgedessen kann man die SM Signalsignatur für den Top-Quark Zerfall ( $t \rightarrow bW$ ) verwenden, um Ergebnisse über den Wirkungsquerschnitt der anomalen Pro-

duktion zu erhalten.

Im Kapitel 2 wird eine Monte Carlo Studie des anomalen Prozesses im Partonniveau vorgeführt. Im Unterkapitel 2.1 wird der Monte Carlo Generator PYTHIA präsentiert, womit wir unsere Ereignisse für die Studie produzieren. Anschliessend wird die Modifizierung des Codes diskutiert, womit wir es geschafft haben unseren Prozess zu simulieren, anhand der schon eingebauten Produktion des angeregten Up-Quarks. Diese Modifizierung wurde vom T. Sjöstrand empfohlen, den Haupt-Ersteller des PYTHIA-Generators. Der Rest des Kapitels befasst sich mit der Studie der anomalen Produktion und der kinematischen Verteilungen des anomal produzierten Top-Quarks und dem gleichzeitigen Vergleich zu den SM-Top-Produktionsprozesse. Als Überprüfung für unsere Simulation plotten wir die Top-Masse-Verteilung und untersuchen die Polarisation des Zerfalls. Wie erwartet, erhalten wir die gleichen Verteilungen wie bei den SM Produktionskanälen. Damit werden wir von der Effektivität der Modifizierung überzeugt und entscheiden, dass PYTHIA uns weiter in der Studie helfen kann.

Im Kapitel 3 wird das CDF Experiment kurz beschrieben. Der Beschleuniger am Fermilab und seine Bestandteile werden skizziert. Anschliessend wird der CDF Detektor und seine Detektionssysteme beschrieben.

Im Kapitel 4 wird der Hauptteil der Analyse präsentiert. Das Kapitel besteht aus zwei Unterkapiteln. Der erste davon befasst sich mit der Simulation unseres Prozesses im CDF Detektor. Die Basis-Schnitte werden angesprochen und die Untergründe werden berücksichtigt. Ziel dieses Unterkapitels ist die Anzahl der erwarteten Ereignisse für die anomale Produktion im 1-Jet-bin zu berechnen. Das passiert indem wir die Methode der CDF-Single-Top-Gruppe verfolgen. Wir wählen die rekonstruierte Top-Masse als Variable mit der besseren Trennung von Signal-Untergrund Ereignissen. Wir schneiden auf  $120 < M_{\ell\nu b} < 230 \text{ GeV}/c^2$  und erhalten die Anzahl  $1.035 \pm 0.050$  für die erwarteten Ereignisse des anomalen Prozesses. Der Gesamtuntergrund beträgt  $61.334 \pm 7.22$  erwartete Ereignisse. Im zweiten Unterkapitel folgen wir wieder die Methode der CDF-Single-Top-Gruppe und fitten unsere Variable mit einer Wahrscheinlichkeits-Fit Funktion. Damit erhalten wir apriori Grenze auf den Wirkungsquerschnitt der anomalen Top-Produktion. Anschliessend setzen wir eine obere Grenze von 14.7 pb auf die anomale Produktion. Diese Ergebnisse sind erklärbar und liegen im Bereich unserer Erwartung. Eine bessere Grenze könnte eventuell mit LHC Daten gesetzt werden, wenn der Hadron-Beschleuniger am CERN vollendet ist.

Anhand der mit dieser Diplomarbeit gesetzten Grenze kann man leicht in einer zukünftigen Analyse die obere Grenze für die anomale Kopplungsstärke  $\kappa_u$  ableiten.

# Introduction

The discovery of the top quark in 1995 at Fermilab completed the puzzle of the third family of the Standard Model (SM). The mass of this particle, though, turned out to be much larger than first expected ( $m_t \simeq 175$  GeV), about 35 times that of the bottom quark, the top's weak isospin partner in the third family. The top mass is of the order of the Electro-Weak Symmetry Breaking (EWSB) scale  $v = 246$  GeV and therefore provides a probe of the physics associated with the generation of the masses for the weak gauge bosons. The top quark is produced either via strong (pair production) or via electroweak interactions (single production) in the SM.

The possibility of a single top production via the strong interaction is not implemented in the SM. This could occur through FCNC (flavor changing neutral currents) this means through interactions, by which a quark flavor is transformed to another quark flavor in the final state, while the charge of the initial quark state remains the same for the final quark state. However, the SM does not contain FCNC at tree level, though they can occur at higher order through radiative corrections. Because of the loop suppression, these SM effects will be small, and so, large FCNC provide a window to physics beyond the SM.

According to theoretical predictions, the anomalous FCNC couplings may be significant in many extensions to the SM (eg. supersymmetry (SUSY)) and could be detected at hadron colliders. At the Tevatron, the hadron collider that delivers our data, it is possible to set an upper limit for the cross section of such anomalous processes, in case they are too small to be efficiently detected. In this analysis, we are specifically interested in the top-up-gluon ( $t$ - $u$ - $g$ ) coupling, one of the possibilities to produce a top quark via 'anomalous' FCNC couplings. In this scenario, an up quark and a gluon from the colliding hadrons combine to form an s-channel top quark, which then decays.

In order to measure the strength of the anomalous coupling, we have first to insert this production mode in our theoretical expressions concerning the strong interaction. We do this by modifying the SM QCD-Lagrangian terms, so that an effective theory is created, which is valid up to certain energy scale. When doing this modification, we have to consider that we also allow the decay channel of a top quark decaying to an up quark and a gluon. To avoid this, since we want to get information only for the production, we have to investigate a certain region of parameter space in which the production mode is allowed, while the decay mode is much smaller than the SM decay mode of the top quark ( $t \rightarrow bW$ ). In that way the signal signature is a bottom quark jet, a lepton and missing energy (neutrino). The lepton and its corresponding neutrino originate from the  $W$  boson decay.

The main goal of our analysis is to set an upper limit on the cross section of the anomalous top production channel ( $u + g \rightarrow t$ ). The result can be then used in a further analysis to deduce an upper limit for the coupling which is related to the cross section.

In Chapter 1, the theoretical framework of our study is presented, starting with the SM and the questions remaining unanswered by the model. In section 1.3, the top quark production mechanism in the SM channels as well as in the anomalous FCNC couplings is further on discussed and finally, a method to incorporate new physics in the SM La-

grangian, creating an effective theory, is shown.

In Chapter 2 we use the Monte Carlo (MC) event generator PYTHIA to study the anomalous FCNC interaction at parton level. The study starts with the investigation of the production and the kinematic of the anomalous top quark, and continues with the investigation of its decay products. Purpose of this parton level study is the correct simulation of the FCNC production mode at pure MC level, since this interaction does not exist in the generator options and therefore the program code had to be manually modified. We apply a cross check including the decay mode of the anomalous top compared to that of the SM produced top quarks, since it is expected to be the same. We find that the MC event generator PYTHIA is useful for our purpose.

In Chapter 3 the CDF experiment is presented and the most important parts of the detector systems are briefly explained.

Chapter 4 is divided in two main sections, the detector simulation and the likelihood fit. In the detector simulation we investigate our process and its background sources, based on the CDF software. In the likelihood fit we set a-priori limits as well as upper limits on the anomalous top cross section based on the CDF II data. Conclusion (Chapter 5) follows, and an Appendix ends this diploma thesis.

# Contents

<b>1</b>	<b>Theoretical Framework</b>	<b>1</b>
1.1	The Standard Model (SM) . . . . .	1
1.2	Questions concerning the Standard Model . . . . .	3
1.3	Top Quark Production . . . . .	4
1.3.1	Top Quark Production in SM channels . . . . .	4
1.3.2	Anomalous FCNC as a Window to New Physics . . . . .	4
1.3.3	Creating an Effective FCNC Theory . . . . .	7
<b>2</b>	<b>Anomalous Top Quark Study at Parton Level</b>	<b>10</b>
2.1	Modelling with PYTHIA . . . . .	10
2.2	Top Quark Production and Kinematic Distributions . . . . .	10
2.2.1	Top Quark Production at Parton Level . . . . .	11
2.2.2	Top Quark Kinematic Distributions . . . . .	15
2.3	Top Quark Decay . . . . .	16
2.3.1	Transverse momenta distributions . . . . .	17
2.3.2	Angular Correlations in Top Quark Decay . . . . .	18
<b>3</b>	<b>The CDF Experiment</b>	<b>25</b>
3.1	Fermilab and Tevatron . . . . .	25
3.2	The Collider Detector at Fermilab . . . . .	29
3.2.1	The Tracking Systems . . . . .	31
3.2.2	The Calorimeter Systems . . . . .	34
3.2.3	The Muon Systems . . . . .	35
3.2.4	The Trigger Systems . . . . .	37
<b>4</b>	<b>Data analysis</b>	<b>41</b>
4.1	Detector Simulation . . . . .	41
4.1.1	Monte Carlo Samples and Selection Requirements . . . . .	41
4.1.1.1	Baseline Cuts . . . . .	41
4.1.1.2	Top Mass Reconstruction . . . . .	41
4.1.2	Signal Acceptances . . . . .	43
4.1.2.1	Cut Flow . . . . .	43
4.1.3	Background . . . . .	44
4.1.3.1	SM Top Quark Background . . . . .	44
4.1.3.2	Di-Boson Background . . . . .	46
4.1.3.3	Further Non-Top Background . . . . .	46
4.1.4	Event Detection Efficiency . . . . .	48

4.1.4.1	Determination of $\epsilon_{\text{evt}}^{\text{MC}}$ . . . . .	49
4.1.4.2	Determination of $\epsilon_{\text{evt}}$ . . . . .	49
4.1.4.3	Non-Top Background Estimate . . . . .	50
4.1.4.4	Number of Expected Events . . . . .	54
4.1.4.5	Top Mass Templates . . . . .	54
4.2	Likelihood Fit . . . . .	57
4.2.1	Likelihood Function . . . . .	58
4.2.2	A-priori Limits . . . . .	60
4.2.3	Data . . . . .	62
<b>5</b>	<b>Conclusion and Outlook</b>	<b>64</b>
<b>A</b>	<b>Appendix</b>	<b>71</b>



# List of Figures

1.1	Feynman diagrams of the channels predicted by the standard model to produce top quarks: top pair ( $t\bar{t}$ ) production (left), single top $t$ -channel (middle) and single top $s$ -channel (right). . . . .	4
1.2	The cosmological Standard Model. The evolution of the universe is shown according to modern knowledge. Today's particle colliders are simulating such a Big Bang at a smaller scale. One can see the energies reached by Tevatron compared to the EWSB scale. This scheme is a modified version of a figure taken from [24]. . . . .	6
1.3	Feynman diagram for direct anomalous top quark production and subsequent decay into $b\ell\nu_\ell$ . . . . .	9
2.1	Center-of-mass energy in the parton system divided by the center-of-mass energy of the hadrons: $\frac{\sqrt{\hat{s}}}{\sqrt{s}} = \sqrt{x_{up} * x_{gluon}}$ for anomalously produced top quarks. . . . .	13
2.2	Center-of-mass energy in the parton system on a logarithmic scale. . . . .	13
2.3	Logarithm of the momentum fractions $x_1$ and $x_2$ of the participating initial state partons. . . . .	14
2.4	Transverse momentum distribution of top quark. . . . .	15
2.5	Rapidity and pseudorapidity distributions of the top quark. . . . .	16
2.6	$Q \cdot \eta$ and invariant mass distribution of the top quark. . . . .	16
2.7	Transverse momentum (W-boson and bottom quark) . . . . .	17
2.8	Cosine of the angle built by the momenta of the W boson and the bottom quark as seen in the top rest frame and in the lab frame. . . . .	19
2.9	Decay configuration of the top quark. The arrows point out the spin directions of the particles before (top quark) and after the decay ( $W^+$ boson and bottom quark). Red arrows stand for the spin configuration that leads to the helicity state $h_W = +1$ of the $W^+$ boson which is forbidden in the SM. Black arrows show the allowed spin orientations, according to the SM, which produce the two helicity states $h_W = 0$ and $h_W = -1$ . Another possibility to build the $h_W = 0$ state would be the configuration with $s_W \uparrow$ but we only refer to the $s_W \downarrow$ -configuration, since the argumentation involves the cosine of the angle between spins and momenta towards which the two different configurations ( $s_W = \uparrow, \downarrow$ ) behave symmetrically. . . . .	19
2.10	$W^+$ boson decay configuration. . . . .	20
2.11	Spin orientations relative to the momenta in the top rest frame for $h_W = 0$ (left and centered box) and $h_W = -1$ (right box). . . . .	20

2.12	Partial and total probability densities. (a) $\frac{dP_0}{d(\cos\alpha)} = \frac{1}{2}(1 - \cos^2\alpha)$ (top left), (b) $\frac{dP_-}{d(\cos\alpha)} = \frac{1}{4}(1 - \cos\alpha)^2$ (top right), (c) $\frac{dP_+}{d(\cos\alpha)} = \frac{1}{4}(1 + \cos\alpha)^2$ (bottom left) and (d) $\frac{dP_{tot}}{d(\cos\alpha)}$ (bottom right). . . . .	22
2.13	$\bar{\ell}$ helicity angle in $t\bar{t}$ -channel and in $t$ -channel . . . . .	23
2.14	$\bar{\ell}$ helicity angle in $s$ -channel and in anoTop-channel . . . . .	23
3.1	Aerial shot of the Fermilab site. Two rings of the accelerator system, the Tevatron and the Main Injector can be seen. . . . .	25
3.2	Schematic view of Fermilab's accelerators for Run II. . . . .	26
3.3	Average peak luminosity per store number. . . . .	27
3.4	Live integrated luminosity delivered (red) and written to tape (blue) since the start of Run II. . . . .	28
3.5	The CDF detector (while rolling in for Run II). . . . .	29
3.6	The CDF detector (cutaway view). . . . .	30
3.7	Inner parts of the CDF detector (cutaway view). . . . .	30
3.8	Longitudinal view of the CDF II tracking system. . . . .	31
3.9	SVX bulkhead end view (left) and L00 end view (right). . . . .	32
3.10	Run II readout functional block diagram. . . . .	39
3.11	A simulated anomalous top event as it would be seen in the COT and the calorimeter (bottom). The color code is blue for the hadronic calorimeter and magenta for the electromagnetic calorimeter, see section 3.2.2. The size of the colored clusters is proportional to the energy deposition. In this event, the highest cluster contains 60.73 GeV resulting mostly from electro- magnetic energy. This is the tower that the isolated electron, originating from the W decay, deposited its energy. The missing $E_T$ vector, that points to the upper right side, represents the neutrino. At the top, the same event is demonstrated on the $\eta$ - $\phi$ plane. The energy is given by the vertical-axis. . . . .	40
4.1	Top-mass templates of the SM top production (top left), the $W$ +heavy flavor channels (top right), the di-boson channels (bottom left) and the sum over the $W$ +heavy flavor channels added to the di-boson channels (bottom right). . . . .	55
4.2	Top-mass templates of all the involved background channels compared to the anomalous top production. . . . .	56
4.3	$Q \cdot \eta$ of the top quark gained from pure MC study compared to the same variable as seen in the detector simulation. . . . .	57
4.4	On the left: Top mass distributions of the signal and background processes in the region of $120 \text{ GeV} < M_{\ell\nu b} < 230 \text{ GeV}$ . On the right: Data versus stacked Monte Carlo templates weighted by the number of expected events. . . . .	58
4.5	A-priori sensitivity for $\sigma_{ano} = 5.0 \text{ pb}$ (top left), for $\sigma_{ano} = 10.0 \text{ pb}$ (top right) and for $\sigma_{ano} = 1.0 \text{ pb}$ (bottom). . . . .	61
4.6	The most probable value for $\sigma_{ano} = 5.0 \text{ pb}$ (top left), for $\sigma_{ano} = 10.0 \text{ pb}$ (top right) and for $\sigma_{ano} = 1.0 \text{ pb}$ (bottom). . . . .	62
4.7	Posterior probability density for the anomalous top quark production. . . . .	63
A.1	helicity angle $\theta^*$ . . . . .	71

A.2 Some of the variables that were at first considered as possible for the fit,  
see section 4.2. . . . . 73

# List of Tables

1.1	The four fundamental forces in nature and their most important characteristics [4]. . . . .	1
1.2	The fermions ordered in three generations and their properties taken from Reference [25]. . . . .	2
1.3	The gauge bosons and some of their properties [25]. . . . .	2
2.1	Example of a particle list of a PYTHIA $u + g \rightarrow t$ event. $I$ is the line number of the particle; $KS$ is the status code; $KF$ is the identification (ID) number of the particle; $orig$ is the line number of the parent particle. $p_x, p_y, p_z$ are the momenta in x, y, z direction in GeV/c. $E$ is the energy in GeV, $m$ is the mass given in GeV/c <sup>2</sup> . . . . .	11
2.2	mean of $\log x_1$ and $\log x_2$ of the partons. . . . .	15
2.3	$f_0(W)$ and $f_-(W)$ values for PYTHIA using the SM parameters ( $f_+(W) = 0$ ). DEV(SM) stands for 'deviation from Standard Model value' and is given in percent. . . . .	24
3.1	Position and properties of the silicon system. . . . .	33
3.2	Overview of the calorimeter properties. The symbol $\oplus$ implies that the constant term is added in quadrature. The energy is given in GeV. The energy resolutions for the electromagnetic calorimeters are for incident electrons and photons and for the hadronic calorimeters for incident isolated pions. .	35
3.3	Segmentation and range of the different calorimeter systems. . . . .	35
3.4	$\eta$ coverage and the minimal $p_T$ for a muon to reach the detector for some parts of the muon system. . . . .	37
4.1	Monte Carlo samples used in the anomalous top analysis. . . . .	42
4.2	The baseline cuts for CEM electrons, CMUP and CMX muons for Run II analyses, taken from [35]. . . . .	42
4.3	Cut flow table of baseline event selection for anomalous top (utopg0) events.	45
4.4	Cut flow table of anomalous top search. We show the cut flow for the additional cuts applied after the $M_{\ell\nu b}$ cut. The lines with ' <b>b tag = 1</b> ' give the number of events in the 1-b-tag-bin. The lines with ' <b>Jet 1 <math>E_t \geq 30</math> GeV</b> ' give the number of the events in the 1-b-tag bin after the extra cut on the leading jet $E_T$ . The lines named ' <b>b tag = 2</b> ' give the number of events in the double-tag-bin. . . . .	46
4.5	Cut flow table of anomalous top events selection summed over all jet bins.	47
4.6	Cross section predictions used in our analysis to predict the number of di-boson background events. . . . .	47

4.7	Correction factor for b-tagging efficiency of the various samples. . . . .	49
4.8	Number of Monte Carlo events after event selection in the 1-jet bin. . . . .	50
4.9	Branching ratio efficiency of the various samples. . . . .	50
4.10	Electron and muon trigger efficiencies, ID efficiency scale (correction) factors and z vertex cut efficiency. . . . .	50
4.11	$\epsilon_{\text{evt}}^{\text{MC}} \cdot \epsilon_{\text{BR}}$ for background and signal samples. The statistical error on the efficiencies is 0.01% or less. . . . .	51
4.12	$\epsilon_{\text{corr}}$ for single top, $t\bar{t}$ and di-boson events . . . . .	51
4.13	$\epsilon_{\text{BR}} \cdot \epsilon_{\text{evt}}^{\text{MC}} \cdot \epsilon_{\text{corr}} \cdot \epsilon_{\text{trig}}$ . . . . .	52
4.14	Number of expected events for single top, $t\bar{t}$ and di-boson Monte Carlo samples. . . . .	53
4.15	Number of Monte Carlo events after event selection in the 1-jet bin. . . . .	53
4.16	Scale factor for 1-jet bin. . . . .	53
4.17	Relative errors on scale factors for different cut scenarios. . . . .	53
4.18	Predicted number of background events for $t\bar{t}$ cross section analysis. . . . .	53
4.19	Cross section predictions used in our analysis to predict the number of background events. . . . .	54
4.20	Number of expected non-top events in anomalous top analysis. W+HF stands for the sum over all W+heavy flavor events. $\Sigma$ stands for the sum over all non-top background processes (other than di-boson). . . . .	54
4.21	Number of background and signal events in the 1-jet bin. SM top production stands for the standard model predicted $t\bar{t}$ pair and the two single top production channels. W+HF stands for 'W+heavy flavor', di-boson stands for WW, WZ, ZZ. . . . .	55
4.22	Signal and background processes considered in the likelihood function. . . . .	58
4.23	Cross section uncertainties for each process. . . . .	58
4.24	Systematic uncertainties for the signal. . . . .	59

# Chapter 1

## Theoretical Framework

### 1.1 The Standard Model (SM)

There are four fundamental forces considered by the physicists to be the generators of any known interaction in nature: The strong force, the electromagnetic force, the weak force and gravitation. The four forces and their most significant features are shown in Table 1.1.

force	couples with	effect	rel. strength	reach
1. strong	color charge	binds quarks and gluons	$10^0$	$10^{-15}$ m
2. electro-magnetic	electric charge	interaction between el. charged particles	$10^{-2}$	infinite
3. weak	weak charge	radioactive decay	$10^{-5}$	subnuclear
4. gravitation	mass	attraction of masses	$10^{-38}$	infinite

Table 1.1: The four fundamental forces in nature and their most important characteristics [4].

Three<sup>1</sup> of these forces, the strong, weak and electromagnetic forces (also called interactions), have been successfully combined in a complete theory. Each element of this theory is described as a Quantum Field Theory (QFT)<sup>2</sup> and these QFTs have very similar structure as gauge theories coupled to the constituents of matter. A variety of experiments contribute to the physicists' faith in this  $SU(3) \times SU(2) \times U(1)$  gauge theory, also referred to as the 'Standard Model' (SM). The SM is an elegant mathematical framework based on the QFTs mentioned above, the spin statistic theorem and three elemental symmetries: the Charge, the Parity and the Time reversal (CPT). In this model, as previously discussed, there are two kinds of particles, the constituents of matter named after the Fermi-statistic<sup>3</sup> (fermions) and the carriers of the forces explained above. The particles of the second category are referred to as gauge bosons, because they all have spins used

---

<sup>1</sup>Gravitation could not yet be combined with the other three forces. One can study this force in the frame of a separate theory, called General Relativity.

<sup>2</sup>quantum field theory: a theoretical structure based on the concepts that come from fusing special relativity, quantum mechanics and fields

<sup>3</sup>statistic for particles with spins  $s = \frac{1}{2}, \frac{3}{2}, \frac{5}{2}, \dots$

for the particles in the Bose-statistic<sup>4</sup>. The fermions, shown in Table 1.2, consist of the quarks and the leptons and can be ordered in three generations. One generation differs from another only in the mass of the particles, since all other quantum numbers are the same when comparing the corresponding members. Each generation involves a quark and its weak partner (that is 2 quarks in all), and a lepton and its corresponding neutrino. For every constituent of matter we also have to consider the existence of its anti-particle. The gauge bosons are introduced in Table 1.3.

generation	fermion	category	symbol	el. charge [e]	spin	mass [ $1/c^2$ ]
1.	down	quark	$d$	$-\frac{1}{3}$	$\frac{1}{2}$	(4-8) MeV
1.	up	quark	$u$	$\frac{2}{3}$	$\frac{1}{2}$	(1.5-4) MeV
1.	electron	lepton	$e$	-1	$\frac{1}{2}$	0.5109 MeV
1.	$e$ -neutrino	lepton	$\nu_e$	0	$\frac{1}{2}$	< 3 eV
2.	strange	quark	$s$	$-\frac{1}{3}$	$\frac{1}{2}$	(80-130) MeV
2.	charm	quark	$c$	$\frac{2}{3}$	$\frac{1}{2}$	(1.15-1.35) GeV
2.	muon	lepton	$\mu$	-1	$\frac{1}{2}$	105.6583 MeV
2.	$\mu$ -neutrino	lepton	$\nu_\mu$	0	$\frac{1}{2}$	< 0.19 MeV
3.	bottom	quark	$b$	$-\frac{1}{3}$	$\frac{1}{2}$	(4.1-4.4) GeV
3.	top	quark	$t$	$\frac{2}{3}$	$\frac{1}{2}$	$174.3 \pm 5.1$ GeV
3.	tau	lepton	$\tau$	-1	$\frac{1}{2}$	1776.99 MeV
3.	$\tau$ -neutrino	lepton	$\nu_\tau$	0	$\frac{1}{2}$	< 18.2 MeV

Table 1.2: The fermions ordered in three generations and their properties taken from Reference [25].

force	boson	symbol	el. charge [e]	spin	mass [ $\text{GeV}/c^2$ ]
strong	gluon	$g$	0	1	0
electro- magnetic	photon	$\gamma$	0	1	0
weak	W-boson	$W^\pm$	$\pm 1$	1	$80.425 \pm 0.038$
	Z-boson	$Z^0$	0	1	$91.1876 \pm 0.0021$

Table 1.3: The gauge bosons and some of their properties [25].

It should be mentioned that the quarks have to carry an additional quantum number in the SM, the color charge. This is of three different types (red, green or blue). Since the color cannot be detected in nature, the quarks must be confined into colorless particles, which are classified into baryons (three quark states) and mesons (quark-anti-quark states). In addition, the different quark-types are called flavors. The interactions between charged particles can be described by Feynman diagrams in the SM. During the processes the forces couple on the interacting particles and so gauge bosons are emitted and re-absorbed. Such diagrams are shown in section 1.3.1. The diagrams can be translated into a formula by means of the Feynman rules. This formula provides the amplitude  $\mathcal{M}$  which is needed for the calculation of the cross section of a process. When dealing with

---

<sup>4</sup>that would be for spins  $s = 0, 1, 2 \dots$

electroweak processes containing quarks, one has to be aware of the fact that the mass eigenstates are not equivalent to the flavor eigenstates. This was experimentally found and is implemented in the theory by a flavor-mixing matrix. The mass eigenstates  $s$ ,  $d$  and the flavor eigenstates  $s'$ ,  $d'$ , which participate at the weak interaction, are related as follows:

$$\begin{pmatrix} d \\ s \end{pmatrix} = \begin{pmatrix} \cos \theta_C & \sin \theta_C \\ -\sin \theta_C & \cos \theta_C \end{pmatrix} \begin{pmatrix} d' \\ s' \end{pmatrix} \quad (1.1)$$

$\theta_C$  stands for the Cabbibo-angle and is about  $13^\circ$ . The extension of this matrix for all three quark generations form the Cabbibo-Kobayashi-Maskawa matrix (CKM-matrix) [5]. It is expressed by a  $3 \times 3$  unitary matrix  $V$ :

$$\begin{pmatrix} d' \\ s' \\ b' \end{pmatrix} = \begin{pmatrix} V_{ud} & V_{us} & V_{ub} \\ V_{cd} & V_{cs} & V_{cb} \\ V_{td} & V_{ts} & V_{tb} \end{pmatrix} \begin{pmatrix} d \\ s \\ b \end{pmatrix} \quad (1.2)$$

The single elements of this matrix have to be determined experimentally.  $V_{q_1 q_2}$  are proportional to the coupling of two quarks  $q_1, q_2$  to a  $W$ -boson. The current values (90% confidence level) [25] for the different elements  $V_{q_1 q_2}$  are given in 1.3.

$$\begin{pmatrix} 0.9739 \text{ to } 0.9751 & 0.221 \text{ to } 0.227 & 0.0029 \text{ to } 0.0045 \\ 0.221 \text{ to } 0.227 & 0.9730 \text{ to } 0.9744 & 0.039 \text{ to } 0.044 \\ 0.0048 \text{ to } 0.014 & 0.037 \text{ to } 0.043 & 0.9990 \text{ to } 0.9992 \end{pmatrix} \quad (1.3)$$

## 1.2 Questions concerning the Standard Model

Even if the SM explains and predicts many procedures in nature, it is already known that the model is incomplete. Many fundamental questions remain unanswered and the SM seems to be unable of answering them, at least based on the structure it has today. One of the problems has already been mentioned and refers to the implementation of gravity in the SM. A promising quantum field theory for gravitation has not yet been accomplished. Because gravitation is a very weak force on small scales, it is also difficult to make experimental tests. On the other hand, the electromagnetic force and the weak force have been successfully combined into the so-called electro-weak force in the frame of the GWS<sup>5</sup>-theory. This theory requires the existence of a new particle, the Higgs boson, which has not yet been found. In case that it won't be discovered in the future, one should be looking for alternative theories. Even if the Higgs boson will be detected and the electromagnetic force proves out to be compatible with the weak force, there is still no guarantee that combining afterwards the strong force with the electroweak force will be possible. Furthermore, the SM has problems in predicting the masses of particles, in fact it makes no predictions about them at all. Moreover, the increase of the masses in every next fermion generation (hierarchy problem) remains unexplained. One would also ask oneself why there have to be three generations of fermions, since the matter in our world seems to be consisting of the particles of just the first generation. Another universal problem is the discrepancy of matter-antimatter. The current amount of CP violation is not enough to motivate it. We so conclude that extensions to the SM in the nearest future will be inevitable.

---

<sup>5</sup>GWS: named after the theorists Glashow, Weinberg and Salam



## 1.3 Top Quark Production

### 1.3.1 Top Quark Production in SM channels

The standard model predicts two ways in which a top quark may be produced: (1) the top pair production, also called  $t\bar{t}$  production and (2) the single top production, occurring in two different channels, the  $t$ -channel (also called  $W$ -gluon-fusion) and the  $s$ -channel (also called  $W^*$ ). Top pair production occurs via the strong interaction and has already been detected at the Tevatron [1, 2, 3]. In fact, that is the only top quark production mode observed until now. In addition, top quarks are expected to be produced singly by the electroweak interaction via  $t$ -channel or  $s$ -channel exchange of an off mass shell  $W$  boson. The Feynman diagrams of both top pair and single top production are shown in Figure 1.1.

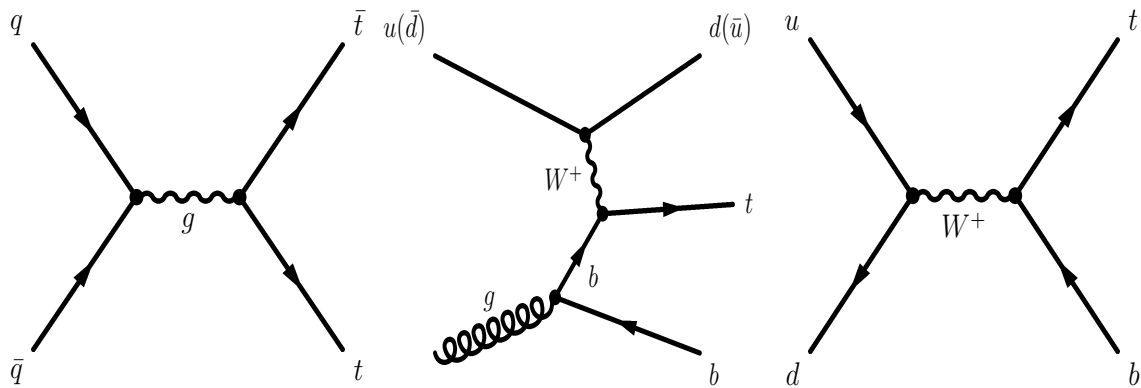


Figure 1.1: Feynman diagrams of the channels predicted by the standard model to produce top quarks: top pair ( $t\bar{t}$ ) production (left), single top  $t$ -channel (middle) and single top  $s$ -channel (right).

### 1.3.2 Anomalous FCNC as a Window to New Physics

The top quark is very heavy, with a mass about 35 times that of the next heaviest quark in the Standard Model (SM), the bottom quark. For this reason it is a likely place to search for new physics. If new physics is found in the top quark sector, it is possible that this could explain why the top is so heavy and how its mass is generated. This could in turn provide us with clues as how the other quark masses arise, which is a question the SM makes no effort to address. Perhaps there is new physics specific to the third family, physics which can explain why the top, bottom and tau lepton are so much heavier than their first and second family counter-parts. In addition, there could be new interactions that are not really involved in producing the large masses, but coupling more significantly to particles with large mass, and thus can be detected by studying the top, while only affecting the other quarks insignificantly.

The top mass is of the order of the Electro-Weak Symmetry Breaking (EWSB) scale  $v = 246$  GeV, see Figure 1.2, and thus provides a probe of the physics associated with the generation of the masses for the weak gauge bosons. The Higgs mechanism of the SM requires a neutral scalar particle, the Higgs boson, which has yet to be directly detected experimentally, but could affect low energy experimental results through loop effects. If the Higgs mechanism with Yukawa interactions is responsible for the generation of the fermion masses, the Higgs boson should have a coupling with the top quark of the order of  $m_t/v$ , and so, interactions involving the top quark may provide a probe of the Higgs physics.

FCNC (Flavor-Changing Neutral Currents) stands for an interaction, during which a quark flavor in the initial state changes to another in the final state, while its charge remains the same. The SM does not contain tree-level FCNC, though they can occur at higher order through radiative corrections. Because of the loop suppression, these SM effects will be small, and so large FCNC provide a window to physics beyond the SM. In this diploma thesis, we are specifically interested in the possibility of a top-up-gluon ( $t$ - $u$ - $g$ ) coupling. It has been argued that anomalous FCNC couplings, see section 1.3.3, may be significant in many extensions to the SM, such as:

- supersymmetry (SUSY)
- other models with multiple Higgs doublets [6]-[14]
- models with new dynamical interactions of the top quark [15, 16]
- models where the top quark has a composite structure [17]
- models where the top quark has a soliton structure [18, 19].

It has been suggested that supersymmetric contributions to such couplings may be large enough to measure at a future hadron collider. In this analysis we will examine FCNC chromomagnetic operators in a model-independent way using direct top quark production at the Fermilab Tevatron. In this scenario, an up quark and a gluon from the colliding hadrons combine to form an s-channel top quark, which then decays. The production of a single, unaccompanied top quark or top antiquark is very small in the SM. We will take as our signal only the case where the top quark decays to a bottom quark and a  $W$  boson.

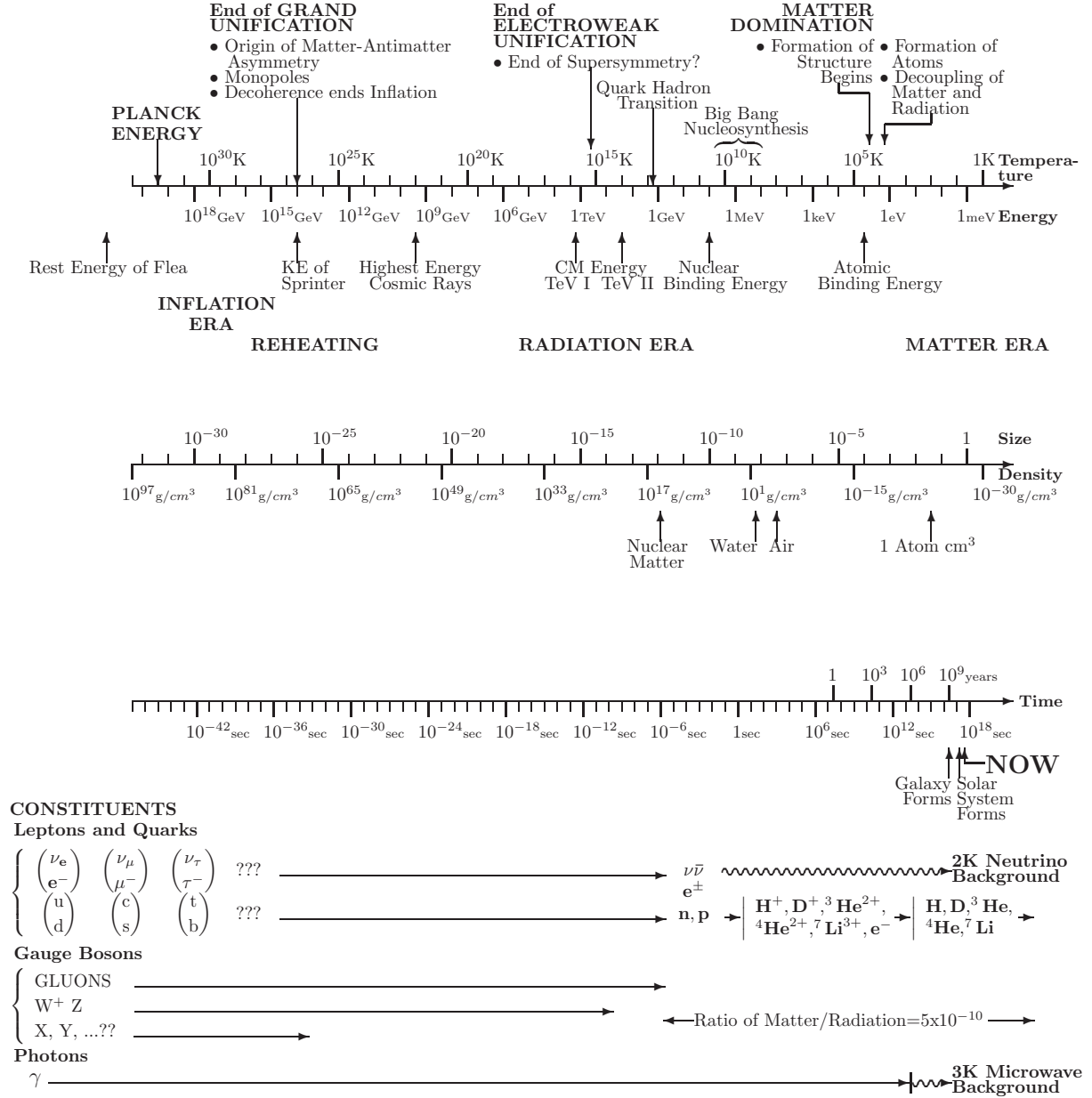


Figure 1.2: The cosmological Standard Model. The evolution of the universe is shown according to modern knowledge. Today's particle colliders are simulating such a Big Bang at a smaller scale. One can see the energies reached by Tevatron compared to the EWSB scale. This scheme is a modified version of a figure taken from [24].

### 1.3.3 Creating an Effective FCNC Theory

In order to study the anomalous FCNC coupling it is not necessary to create a whole new theory. We may incorporate new physics in the SM considering an effective Lagrangian [21, 22]:

$$\mathcal{L}_{eff} = \mathcal{L}_0 + \mathcal{L}_1 \quad (1.4)$$

where  $\mathcal{L}_1$  contains operators of dimension higher than four, multiplied by coefficients with appropriate dimensions of mass to insure that the dimension of the Lagrangian as a whole remains four. Since the resultant theory is not valid to an arbitrarily high energy scale, it is not a fundamental physical theory. Instead, it represents the theory that is 'effective' at a lower energy scale where the energy is too low to allow us to see the full details of the underlying physics. The coefficients with dimensions of mass in front of the effective terms characterize the mass scale at which new physics must enter the theory if any non-SM effect is to be found. In our case, since we wish to consider the possibility of a flavor-changing gluonic current,  $\mathcal{L}_0$  will be the QCD Lagrangian, given by

$$\mathcal{L}_0 = -\frac{1}{4}G_{\mu\nu}^a G^{a\mu\nu} + \bar{q}i\gamma^\mu D_\mu q - m_q \bar{q}q \quad (1.5)$$

where  $D_\mu = \partial_\mu - ig_s \frac{\lambda^a}{2} G_\mu^a$  is the covariant derivative and  $G^{a\mu\nu}$  is the gauge field tensor of the gluon.  $\mathcal{L}_1$  is defined as follows:

$$\mathcal{L}_1 = \frac{g_s \kappa_u}{\Lambda} [\bar{u}\sigma^{\mu\nu} \frac{\lambda^a}{2} t G_{\mu\nu}^a + H.c.] \quad (1.6)$$

where  $\kappa_u$  is a dimensionless parameter that relates the strength of the 'new coupling' to the constant  $g_s$ .  $\Lambda$  is the new physics scale, related to the mass cut-off scale above which our effective theory breaks down. The parton cross section for direct top quark (or top anti-quark) production is given by [22]:

$$d\sigma = \frac{1}{4} \frac{1}{(4\pi)^5} \frac{\hat{s} - M_{\ell,\nu_\ell}^2}{\hat{s}^2} |\bar{\mathcal{M}}|^2 d\Omega_b d\Omega_\ell dM_{\ell,\nu_\ell}^2 \quad (1.7)$$

where the spin-averaged squared matrix element is

$$\begin{aligned} |\bar{\mathcal{M}}|^2 &= \frac{256\pi^3 \alpha^2 \alpha_s \kappa_u^2}{3\sin^4\theta_W \Lambda^2} \\ &\times \frac{\hat{s} (p_b \cdot p_{\nu_\ell}) [\hat{s} (q_u \cdot p_\ell) + m_t^2 (q_g \cdot p_\ell)]}{\left[ (\hat{s} - m_t^2)^2 + m_t^2 \Gamma_t^2 \right] \left[ (M_{\ell,\nu_\ell}^2 - M_W^2)^2 + M_W^2 \Gamma_W^2 \right]} \end{aligned} \quad (1.8)$$

$p_{b,\ell,\nu_\ell}$  are the four-momenta of the outgoing bottom quark, lepton and neutrino respectively,  $q_{u,g}$  are the four-momenta of the incoming up quark and gluon.  $\Gamma_W$  is the decay width of the W boson, while  $\Gamma_t$  is defined as follows:

$$\Gamma_t = \Gamma_{t \rightarrow bW} \left[ 1 + \frac{128 M_W^2 \alpha_s}{3\alpha^2 \left(1 - \frac{M_W^2}{m_t^2}\right)^2 \left(1 + 2\frac{M_W^2}{m_t^2}\right)} \left(\frac{\kappa_u^2}{\Lambda^2}\right) \right] \quad (1.9)$$

where  $\Gamma_{t \rightarrow bW}$  is the SM top quark decay width to a bottom quark and a W-boson, given by

$$\Gamma_{t \rightarrow bW} = \frac{G_F m_t^3 |V_{tb}|^2}{8\pi\sqrt{2}} \left[1 - \frac{M_W^2}{m_t^2}\right]^2 \left[1 + 2\frac{M_W^2}{m_t^2}\right] \quad (1.10)$$

$M_{\ell,\nu_\ell}^2$  in 1.8 stands for the squared invariant mass, not necessarily on shell of the W-boson, defined as

$$M_{\ell,\nu_\ell}^2 \equiv (p_\ell + p_{\nu_\ell})^2 \quad (1.11)$$

where  $\sqrt{s}$  is the parton center-of-mass energy.

As we have explained in chapter 1.3.2, it is natural to look to the top quark as a window to new physics. One could hope to learn about these anomalous FCNC couplings both by studying single top production and decays. However, it brings us back to the problem with using top decays to determine the magnitude of a coupling. The decay can provide information about the relative branching fraction of the exotic decay compared to the SM top decay  $t \rightarrow W^+b$ , but since it does not allow one to measure the top decay width, it cannot provide a limit on the size of the exotic operator without first making an assumption concerning the nature of the  $W$ - $t$ - $b$  interaction. New physics contributions to single top quark production would scale as  $(\sqrt{s}/\Lambda)^n$  [23] where  $s$  is the average center-of-mass energy of the reaction and  $n$  is a positive integer or zero. On the other hand, top decay processes scale as  $(m_t/\Lambda)^n$ . At high energy colliders such as the Tevatron,  $\sqrt{s}$  can be considerably larger than  $m_t$ , thus enhancing the relative importance of new physics in single top production. While the  $t \rightarrow ug$  decay will occur in the presence of the anomalous couplings given in Equation 1.6, it is smaller than the  $t \rightarrow bW$  decay for  $\kappa/\Lambda \lesssim 0.2 \text{ TeV}^{-1}$ . In Reference [20] a limit on the  $t$ - $c$ - $g$  coupling strength  $\kappa_c$  is placed by examining the decay of the top quark into a charm quark and a gluon. It is found that an upper limit on  $\kappa_c$  of  $0.43 \text{ TeV}^{-1}$  with  $b$  tagging (see explanation in section 4.1) for  $200 \text{ pb}^{-1}$  of data can be measured at the Tevatron. If the  $c$  and the  $u$  jets are not distinguished, their result applies equally well to  $\kappa_u/\Lambda$ , if one uses the up quark coupling alone. Given the existing upper band of the anomalous coupling,  $t \rightarrow bW$  will be the dominant decay mode of the top quark. Since the  $W$  boson decays into a charged electron or muon and its corresponding neutrino, it has an identifiable signature, we consider only the  $t \rightarrow bW \rightarrow b\ell\nu_\ell$  decay for our signal. Figure 1.3 shows the Feynman diagram for direct top quark production and subsequent decay into  $b\ell\nu_\ell$ .

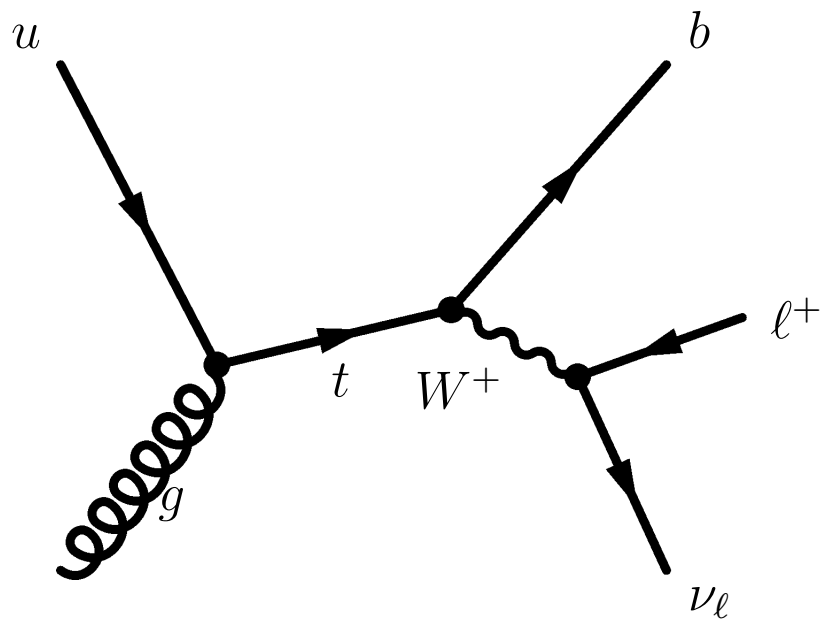


Figure 1.3: Feynman diagram for direct anomalous top quark production and subsequent decay into  $b\ell\nu_{\ell}$ .

# Chapter 2

## Anomalous Top Quark Study at Parton Level

### 2.1 Modelling with PYTHIA

PYTHIA is a general purpose Monte Carlo event generator which provides an exclusive description of individual events at the hadron level. These can be analysed in exactly the same way as experimental data and can be put through full detector simulation to predict the experimental event detection efficiency and estimate experimental systematics. PYTHIA includes approximate treatments of higher order perturbative effects, hadronisation, parton shower, secondary decays and the underlying event [27]. To generate our events we use PYTHIA version 6.221[26]. Table 2.1 shows an example of the particle list at parton level of one  $u + g \rightarrow t$  event. We use the following settings:

- The center-of-mass energy of the  $p\bar{p}$ -system is set to  $\sqrt{s} = 1960$  GeV.
- We select the subprocess:  $u + g \rightarrow u^*$ ; `MSUB = 148`.
- We change the process such that it produces a top quark. This has to be done in the PYTHIA source code. This adaption was recommended by T. Sjöstrand, the main author of PYTHIA.
- We turn on excited fermions; `MSTP(6) = 1`.

### 2.2 Top Quark Production and Kinematic Distributions

In this section we compare kinematic distributions of the top quark for  $u + g \rightarrow t$  anomalous production,  $t$ - and  $s$ -channel single top quark production and  $t\bar{t}$  production.

$I$	$KS$	$particle$	$KF$	$orig$	$p_x$	$p_y$	$p_z$	$E$	$m$
0	21	$p$	2212	-1	0	0	980	980	0.93827
1	21	$\bar{p}$	-2212	-1	0	0	-980	980	0.93827
2	21	$g$	21	0	0.502812	0.633211	20.2308	20.247	-0
3	21	$\bar{u}$	-2	1	0.511271	1.21071	-600.62	600.621	-0
4	21	$g$	21	2	2.19491	0.750702	13.9436	14.1352	0
5	21	$\bar{u}$	-2	3	4.84233	2.34851	-541.849	541.876	0
6	21	$\bar{t}$	-6	-1	7.03725	3.09921	-527.906	556.011	174.37
7	21	$W^-$	-24	6	24.2951	34.5558	-143.323	169.729	80.5108
8	21	$b$	-5	6	-17.2578	-31.4566	-384.582	386.282	4.8
9	21	$e^-$	11	7	31.6866	35.8138	-153.047	160.344	0.00051
10	21	$\bar{\nu}_e$	-12	7	-9.08685	-3.86159	6.18527	11.6508	0
11	11	$W^-$	-24	7	22.5998	31.9522	-146.862	171.995	80.5108
12	1	$e^-$	11	9	31.6866	35.8138	-153.047	160.344	0.00051

Table 2.1: Example of a particle list of a PYTHIA  $u + g \rightarrow t$  event.  $I$  is the line number of the particle;  $KS$  is the status code;  $KF$  is the identification (ID) number of the particle;  $orig$  is the line number of the parent particle.  $p_x$ ,  $p_y$ ,  $p_z$  are the momenta in x, y, z direction in GeV/c.  $E$  is the energy in GeV,  $m$  is the mass given in GeV/c<sup>2</sup>.

### 2.2.1 Top Quark Production at Parton Level

In the parton model a proton or an antiproton is regarded as a composition of quasi-free partons (quarks or gluons). The partons share the total momentum of the proton:

$$\mathcal{P}_{proton} = \sum_i \mathcal{P}_i$$

where  $\mathcal{P}_i$  is the momentum of parton  $i$ . The parton model allows to factorize the particle interaction into a hard scattering process and soft (or softer) processes, such as initial state radiation, fragmentation and the decay of unstable particles. In our case we are dealing with a hard  $2 \rightarrow 1$  process. It is instructive to investigate the momentum fraction  $x_i$  of the participating initial state partons  $i$ . In this notation the four-momenta of the partons are described by:

$$\begin{aligned}\mathcal{P}_1 &= E_{beam}(x_1; 0, 0, x_1) \\ \mathcal{P}_2 &= E_{beam}(x_2; 0, 0, -x_2)\end{aligned}$$

where  $E_{beam}$  is the beam energy. The center-of-mass energy in the parton system is then given by:

$$\sqrt{\hat{s}} = \sqrt{x_1 x_2} \cdot \underbrace{2E_{beam}}_{\sqrt{s}}$$

With a beam energy of 980 GeV and a minimum of 175 GeV for the center-of-mass energy needed to produce a top quark, a minimum of 0.0893 for  $\sqrt{x_1 x_2}$  is required to produce a top quark. Figures 2.1 and 2.2 show the  $\sqrt{x_1 x_2}$  distribution for anomalous top quark production ( $u + g \rightarrow t$ ). We observe a very sharp peak at the kinematic threshold of



$\sqrt{x_1 x_2} = 0.0893$ . That means that the top quarks are produced with very little extra energy, which is in strong contrast to the SM production mechanisms as can be seen from Fig. 2.2. In Fig. 2.3 we show the distributions of the logarithm of the individual momentum fractions of the participating partons.

1. For anomalous top quark production we denote the momentum fraction of the up quark as  $x_1$  shown in the top histogram of Fig. 2.3. The momentum fraction of the gluon is  $x_2$ .
2. For t-channel single top quark production  $x_1$  is the momentum fraction of the up quark or down quark,  $x_2$  is the momentum fraction of the bottom quark.
3. For s-channel single top quark production  $x_1$  is the momentum fraction of the up quark,  $x_2$  is the momentum fraction of the down quark.
4. For  $t\bar{t}$  production  $x_1$  is the momentum fraction of the parton coming from the proton,  $x_2$  is the momentum fraction of the parton from the anti-parton.

From the  $x$ -distributions we can make the following observations:

1. For  $t\bar{t}$  both distributions are identical (within the statistical errors), as should be expected because we do not distinguish the different flavors for the process.
2. For s-channel single top quark production the up quarks contribute on average more momentum than the down quarks. The mean of  $\log x$  is -0.77 for up quarks and -0.91 for down quarks. This is to be expected since the parton distribution function for up quarks is harder than for down quarks.
3. For t-channel single top quark production the  $x$ -distribution for the constituent quarks (up and down,  $x_1$ ) is much harder than the distribution for b quarks. This is also expected since the b quarks are sea quarks, which have in general a much softer parton distribution function than constituent quarks.
4. The  $x$ -distribution of the up quark ( $x_1$ ) for anomalous top quark production is quite similar to the one for s- and t-channel single top production. The  $x$ -distribution of the gluon, however, is very soft. The mean of  $\log x_2$  is only -1.31. This means that the main part of the energy for anomalous top quark production comes from the up quark, while the gluon merely induces the flavor change.

Table 2.2 shows the mean momentum fractions of each parton involved in the four top production processes under consideration. As expected, the lowest values are produced by the gluon of the anomalously produced top quark, to the bottom quark of the  $t$ -channel (since it comes from the sea quarks) and to the down quark of the  $s$ -channel. A greater momentum fraction ( $\log x \simeq -0.7$ ) possess the up quarks involved in the anomalous top production and the  $s$ -channel. The largest momentum fraction belongs to the up quark of the  $t$ -channel, since the latter particle is frequently a valence quark of the proton.

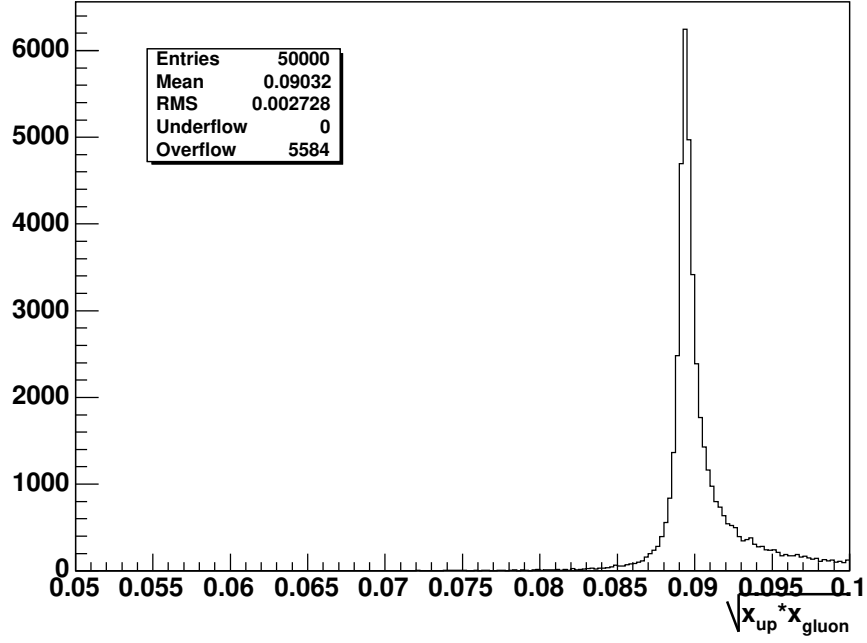


Figure 2.1: Center-of-mass energy in the parton system divided by the center-of-mass energy of the hadrons:  $\frac{\sqrt{\hat{s}}}{\sqrt{s}} = \sqrt{x_{up} * x_{gluon}}$  for anomalously produced top quarks.

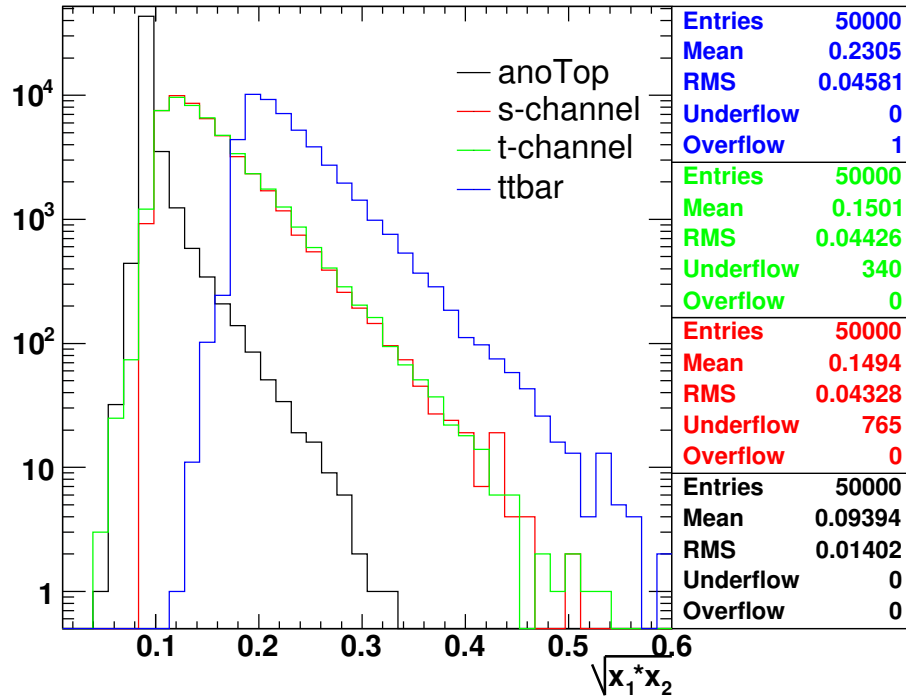


Figure 2.2: Center-of-mass energy in the parton system on a logarithmic scale.

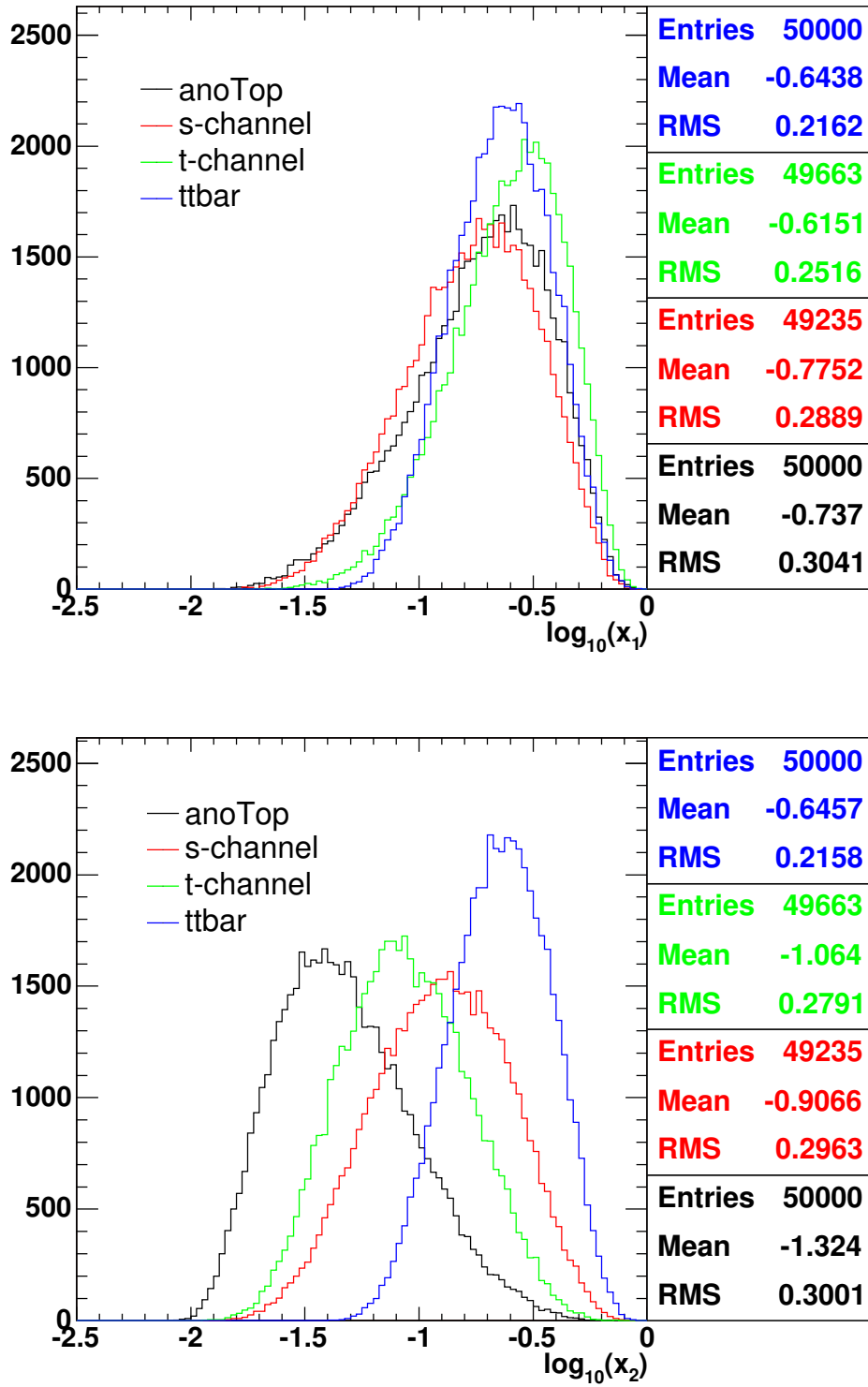


Figure 2.3: Logarithm of the momentum fractions  $x_1$  and  $x_2$  of the participating initial state partons.

channel	mean $\log x_1$	parton	channel	mean $\log x_2$	parton
$s$ -channel	-0.775	up quark	anoTop	-1.324	gluon
anoTop	-0.737	up quark	$t$ -channel	-1.064	bottom quark
$t\bar{t}$ -channel	-0.644	$q, \bar{q}$	$s$ -channel	-0.907	down quark
$t$ -channel	-0.615	up quark	$t\bar{t}$ -channel	-0.646	$q, \bar{q}$

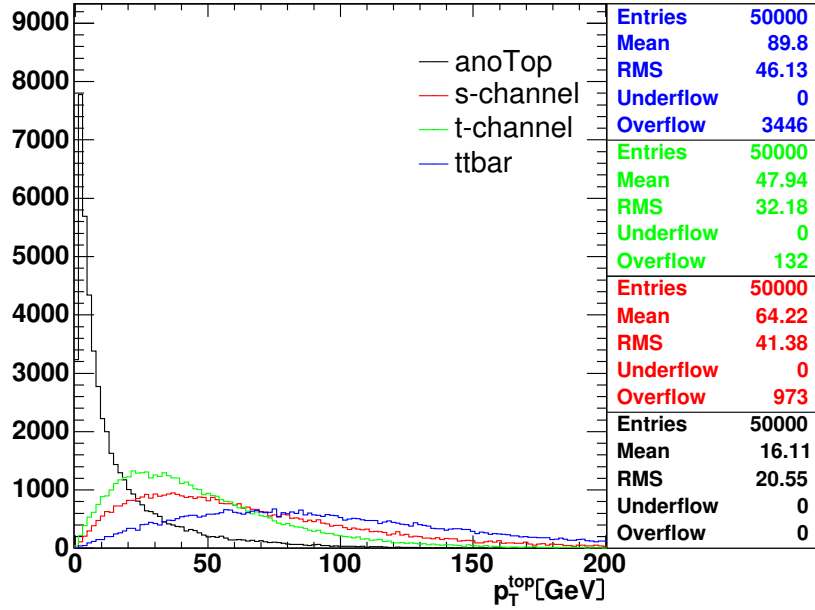
Table 2.2: mean of  $\log x_1$  and  $\log x_2$  of the partons.

Figure 2.4: Transverse momentum distribution of top quark.

### 2.2.2 Top Quark Kinematic Distributions

One important characteristic of the anomalously produced top quark is its low transverse momentum (Figure 2.4).

The anomalously produced top quark has a broader rapidity distribution than the top quarks produced in the SM channels, see Figure 2.5. The difference between anomalous top and SM top quarks is even more pronounced in the pseudorapidity ( $\eta$ ) distribution, see Figure 2.5. While the  $\eta$  distributions for SM top quark production are central and drop essentially to zero at values beyond  $|\eta| > 4$ , the  $\eta$  distribution of the anomalously produced top quarks has two peaks at  $\eta \simeq 4$  and  $\eta \simeq -4$ . There is a small asymmetry between the positive and the negative side of the  $\eta$  distribution for anomalous top quarks. The source of this asymmetry is still under investigation. Since this effect is quite small, we neglect it in the further course of this study. In Figure 2.6 we show the  $Q \cdot \eta$  distribution, which is defined as the product of the charge and the pseudorapidity of the top quark. The  $t\bar{t}$ -channel is scaled with a factor 0.5, since we add two entries per event, one from the top quark and one from the top anti-quark. The  $Q \cdot \eta$  distribution exhibits a distinct asymmetry. Figure 2.6 also shows the mass distribution for each production channel. The

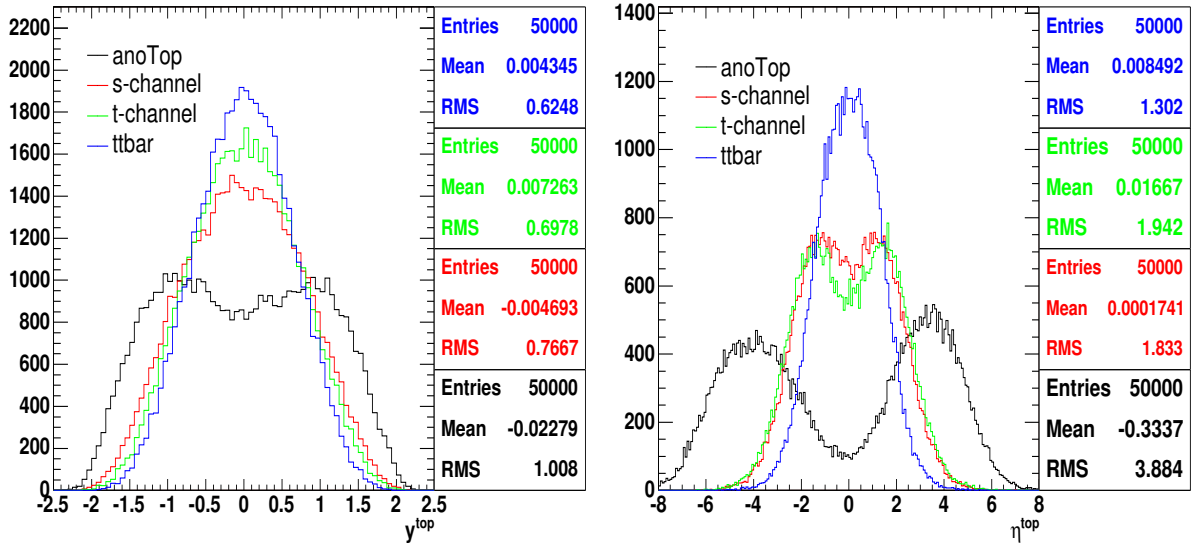
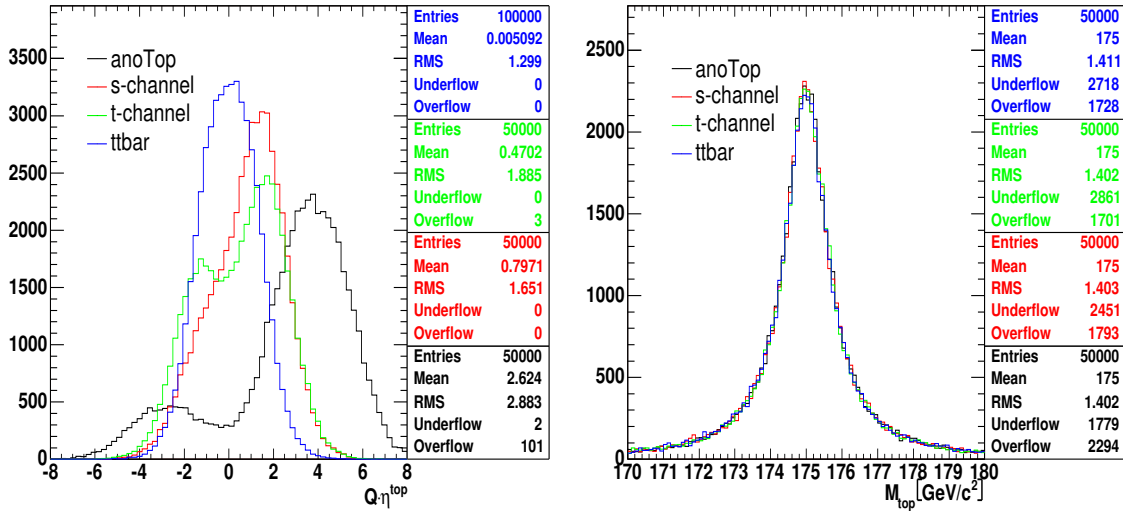


Figure 2.5: Rapidity and pseudorapidity distributions of the top quark.

top mass distribution is a cross check to prove that the anomalous top process is correctly generated.

Figure 2.6:  $Q \cdot \eta$  and invariant mass distribution of the top quark.

## 2.3 Top Quark Decay

In the SM the top quark decays by nearly 100% into a W boson and a bottom quark:  $t \rightarrow W^+ + b$ . We will follow this assumption. If a  $u + g \rightarrow t$  production mode exists, the top quark decay width will change because the decay  $t \rightarrow u + g$  will also be possible.

In our study we follow Reference [28] and assume a parameter space for  $\kappa_u$  such, that the FCNC decay mode can be neglected. Experimentally, we classify top quark events according to the decay modes of the W boson coming from the top quark decay. The W boson can decay to quark-anti-quark pairs  $W^\pm \rightarrow q_1 \bar{q}_2$ ,  $BR = (67.96 \pm 0.35)\%$ , or to leptons,  $BR = (32.03 \pm 0.05)\%$ , [28]. In our analysis we only consider the decay modes  $W^+ \rightarrow \mu^+ \nu_\mu$  with  $BR = (10.57 \pm 0.22)\%$  and  $W^+ \rightarrow e^+ \nu_e$  with  $BR = (10.72 \pm 0.16)\%$ . The  $W^+ \rightarrow \tau^+ \nu_\tau$  mode is not taken into account because events with hadronic  $\tau$  decays are difficult to distinguish against background. In the full analysis, presented in Chapter 4, we take into account the cross feed from  $\tau \rightarrow \mu/e$  decays contributing to the acceptance.

### 2.3.1 Transverse momenta distributions

As a consequence of the low transverse momentum of the anomalously produced top quark (Figure 2.4), almost the entire transverse momentum of its decay products, the  $W^+$  boson and the bottom quark, are due to the transformation of the top mass into energy. The transverse boost of the top quark is negligible. That is why both histograms in Figure 2.7 show the so called Jacobian peak for the  $p_T$  distribution of the top quark decay products, which is the characteristic maximum occurring in the transverse momentum spectrum of two body decays.

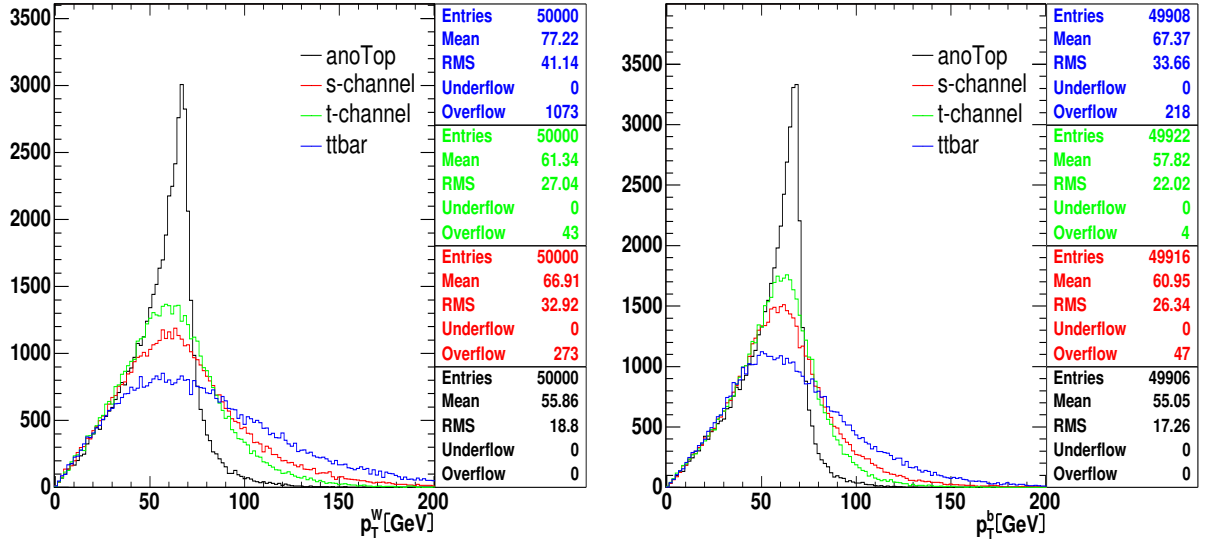


Figure 2.7: Transverse momentum (W-boson and bottom quark)

A short explanation of the origin of the Jacobi-peak should help us interpret these results. If one sets the z-axis in the top quark rest frame such that it shows in the same direction as the momentum of the decay product ( $W^+, b$ ) as seen in the lab frame, one gets the following expression for the transverse momentum of this decay product ( $p_T$  remains invariant under this transformation):

$$p_T = |\vec{p}_{lab}| \sin \theta_{lab} \quad (2.1)$$

for the lab frame, where  $\vec{p}_{lab}$  is the momentum of the decay product as seen in the lab frame and  $\theta_{lab}$  is the angle built by the  $z_{lab}$ -axis and the transverse momentum  $p_T$ . We now set the  $z$ -axis of the top quark rest frame pointing in the same direction with  $\vec{p}_{lab}$  and get:

$$p_T = |\vec{p}_{rest}| \sin \theta_{rest} \quad (2.2)$$

where  $\vec{p}_{rest}$  is the momentum of the decay product as seen in the top quark rest frame and  $\theta_{rest}$  is the angle built by the  $z_{rest}$ -axis= $\frac{\vec{p}_{lab}}{|\vec{p}_{lab}|}$  and the transverse momentum  $p_T$ . Note that the value of  $p_T$  remains the same in both expressions, only the values of the momenta  $\vec{p}_{lab}, \vec{p}_{rest}$  and the angles  $\theta_{lab}, \theta_{rest}$  vary due to the transformation. Expression (2.2) combines the knowledge of the  $p_T$  measured in the lab frame and the information about the momentum of the decay product in the rest frame of the top quark. We now build the derivative of  $p_T$  with respect to  $\cos \theta_{rest}$ :

$$\left| \frac{dp_T}{d \cos \theta_{rest}} \right| = \frac{|\vec{p}_{rest}^2 \cos \theta_{rest}|}{p_T} = \frac{|\vec{p}_{rest}|}{p_T} \sqrt{\vec{p}_{rest}^2 - p_T^2} \quad (2.3)$$

We can use (2.3) to express the differential decay width  $d\Gamma$ :

$$\frac{d\Gamma}{dp_T} = \frac{d\Gamma}{d \cos \theta_{rest}} \frac{d \cos \theta_{rest}}{dp_T} = \frac{d\Gamma}{d \cos \theta_{rest}} \frac{p_T}{|\vec{p}_{rest}|} \frac{1}{\sqrt{\vec{p}_{rest}^2 - p_T^2}}$$

One should notice that if  $p_T = |\vec{p}_{rest}|$  the  $p_T$  histogram of the correspondent decay product should show a peak. This happens for  $\theta_{rest} = \frac{\pi}{2}$  and implies that most of the energy of the decay products flows in the transverse direction for this value of  $p_T$ . We do observe the Jacobi-peak for both of the decay products and therefore, considering also the top quark's low transverse momentum, we conclude that the latter is produced practically motionless in this channel.

### 2.3.2 Angular Correlations in Top Quark Decay

In this paragraph we investigate the polarization of the top quark decay products. In particular, we check whether the polarization is correctly handled for the anomalous top quark sample. In the top rest frame the  $W^+$  boson and the bottom quark decay 'back-to-back'. The angle between the  $W^+$  boson and the bottom quark momentum is  $\theta_{Wb}^{top} = \pi$ , as is shown for our generated events in Figure 2.8 (on the left). The angle in the lab frame is denoted  $\theta_{Wb}^{lab}$  and  $\cos \theta_{Wb}^{lab}$  is shown in Figure 2.8 (on the right). In the SM the  $W^+$  boson couples only to fermions of lefthanded chirality. Due to the 5 GeV mass of the bottom quark, the latter behaves like a 'nearly' massless particle relatively to the scale set by the mass of the top quark ( $m_t \simeq 175$  GeV). Therefore, the chirality of the bottom quark translates into helicity. The bottom quark has practically always helicity  $h_b = -1$  in the top rest frame. On the other hand, spin-1-particles, such as the  $W^+$  boson, have three possible helicity states,  $h_W = 0, \pm 1$ . In the described decay, though, the  $h_W = +1$ -state is forbidden due angular momentum conservation. The spins of the  $W^+$  boson and the bottom quark have to add up to the spin of the top quark.

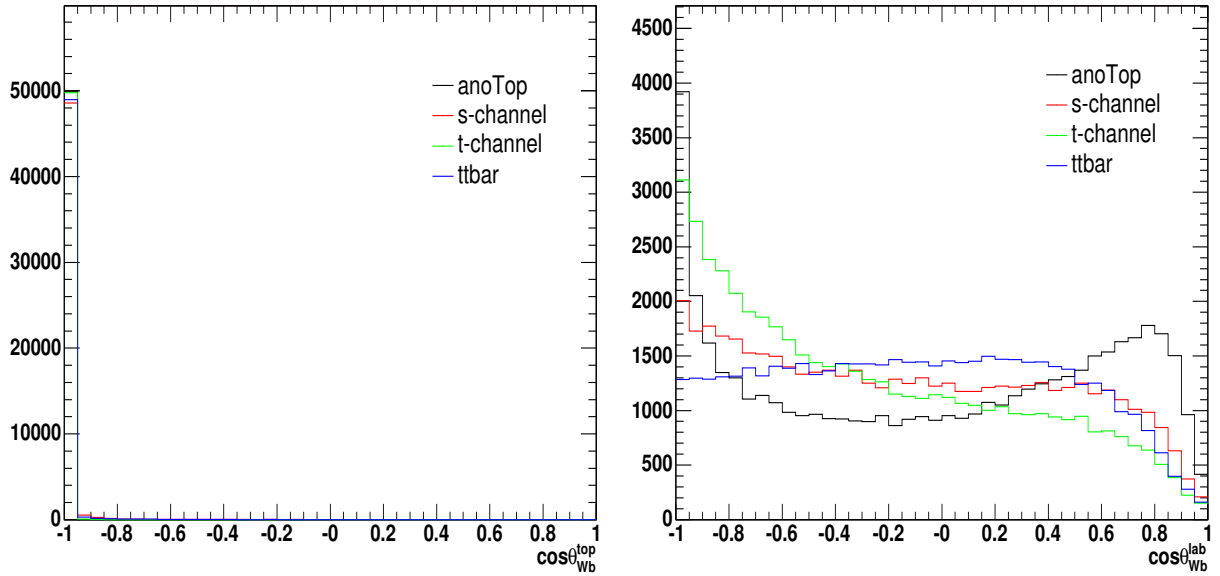


Figure 2.8: Cosine of the angle built by the momenta of the  $W$  boson and the bottom quark as seen in the top rest frame and in the lab frame.

Figure 2.9 illustrates the three possible spin configurations. As one can see, the  $h_W = +1$  state for the  $W^+$  boson would imply a final spin- $\frac{3}{2}$ -state for the system, unable to be compensated by the spin of the top quark ( $s_t = \frac{1}{2}$ ). This forces the  $W^+$  boson to be either in a  $h_W = 0$  or a  $h_W = -1$  state.

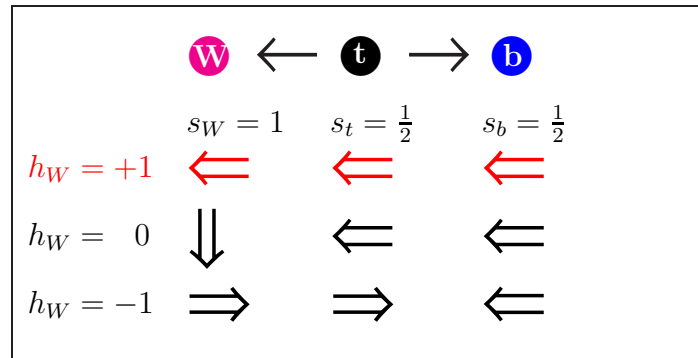


Figure 2.9: Decay configuration of the top quark. The arrows point out the spin directions of the particles before (top quark) and after the decay ( $W^+$  boson and bottom quark). Red arrows stand for the spin configuration that leads to the helicity state  $h_W = +1$  of the  $W^+$  boson which is forbidden in the SM. Black arrows show the allowed spin orientations, according to the SM, which produce the two helicity states  $h_W = 0$  and  $h_W = -1$ . Another possibility to build the  $h_W = 0$  state would be the configuration with  $s_W \uparrow$  but we only refer to the  $s_W \downarrow$ -configuration, since the argumentation involves the cosine of the angle between spins and momenta towards which the two different configurations ( $s_W = \uparrow, \downarrow$ ) behave symmetrically.



The fractional occurrences of each helicity state are

$$f_+(W) = 0 \quad (2.4)$$

$$f_0(W) = \frac{m_t^2}{2m_W^2 + m_t^2} = 0.701 \pm 0.0120 \quad (2.5)$$

$$f_-(W) = \frac{2m_W^2}{2m_W^2 + m_t^2} = 0.299 \pm 0.0012 \quad (2.6)$$

The direction of the  $W^+$  spin in the top frame determines the spin directions of the leptonic products of the  $W^+$  decay. Two criteria have to be satisfied: (1) the neutrino has to be left-handed (negative helicity) and (2) the total angular momentum (here spin) has to be conserved. This leaves us with only one possible spin configuration for  $W^+$  decay: the charged anti-lepton ( $e^+/\mu^+$ ) momentum points predominantly in the direction of the  $W^+$  spin, while the neutrino momentum is anti-parallel to the  $W^+$  spin, see Figure 2.10. The spin configuration of the decay products in the top frame is shown in Figure 2.11. If the W boson has helicity  $h_W = 0$ , the charged lepton and the neutrino decay predominantly in directions perpendicular to the bottom quark momentum. If the W boson has helicity  $h_W = -1$  the charged anti-lepton ( $\mu^+/e^+$ ) decays predominantly in the same direction as the bottom quark.

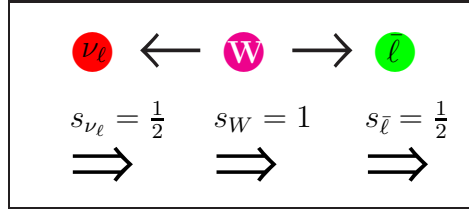


Figure 2.10:  $W^+$  boson decay configuration.

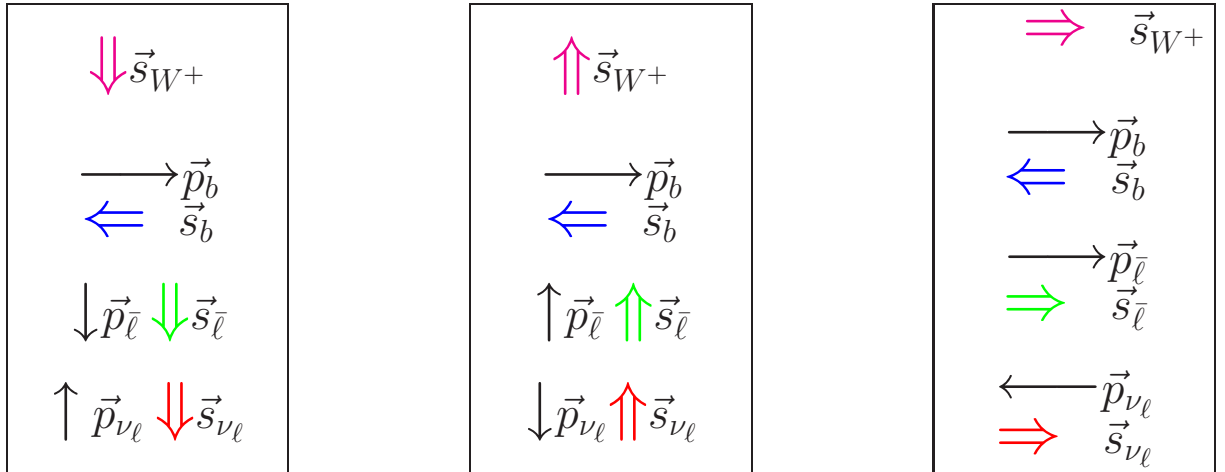


Figure 2.11: Spin orientations relative to the momenta in the top rest frame for  $h_W = 0$  (left and centered box) and  $h_W = -1$  (right box).

We denote the angle between the charged leptons and the bottom quark in the top frame as  $\alpha$ . The probability density of  $\alpha$  for the different  $W$  helicities is given below [29, 30]:

$$\frac{dP_+}{d(\cos\alpha)} = \frac{1}{4}(1 + \cos\alpha)^2 \quad (2.7)$$

$$\frac{dP_0}{d(\cos\alpha)} = \frac{1}{2}(1 - \cos^2\alpha) \quad (2.8)$$

$$\frac{dP_-}{d(\cos\alpha)} = \frac{1}{4}(1 - \cos\alpha)^2 \quad (2.9)$$

These distributions are depicted in Figure 2.12(a),(b) and (c). The SM prediction for the total probability density is composed out of the distribution for  $h_W = 0$  and  $h_W = -1$  weighted by the fractional occurrences,  $f_0(W)$  and  $f_-(W)$ , of these helicities as given in (2.4), (2.5) and (2.6). The total probability density (normalized to 1) is thus given by:

$$\frac{dP_{tot}}{d(\cos\alpha)} = f_-(W) \frac{dP_-}{d(\cos\alpha)} + f_0(W) \frac{dP_0}{d(\cos\alpha)} \quad (2.10)$$

The expected distribution of  $\frac{dP_{tot}}{d(\cos\alpha)}$  is drawn in Figure 2.12(d).

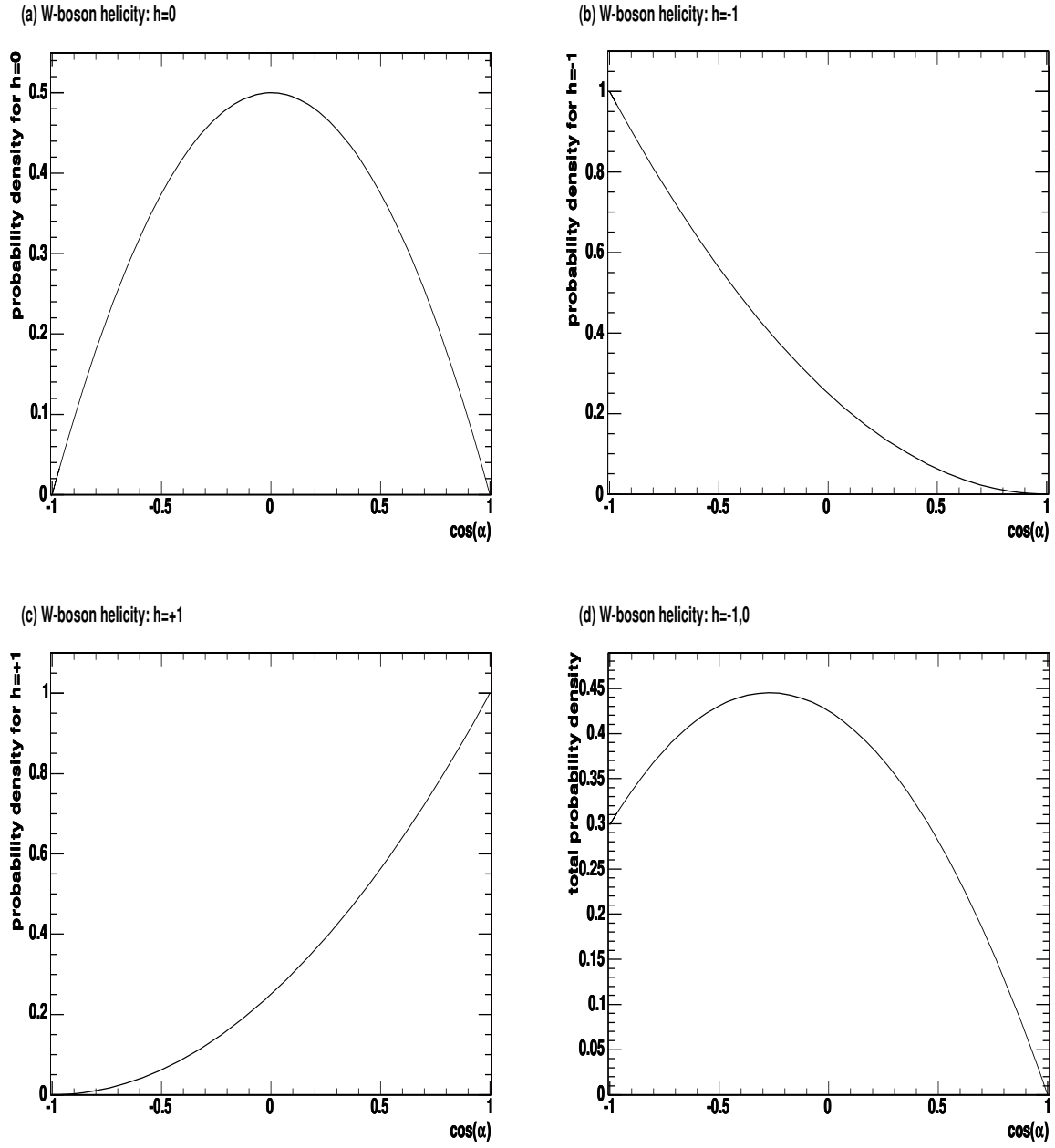
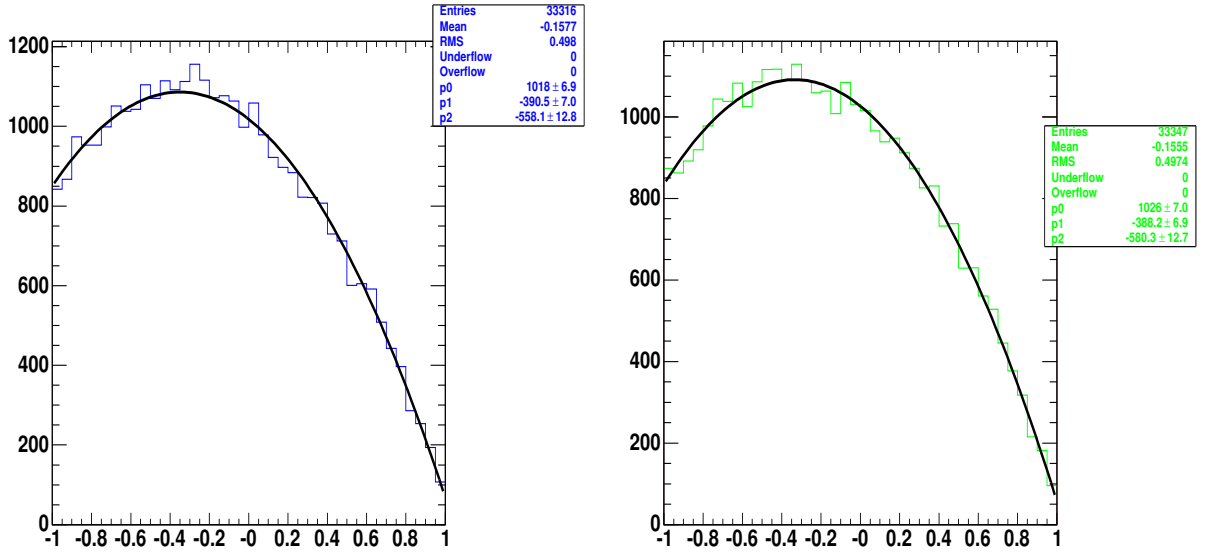
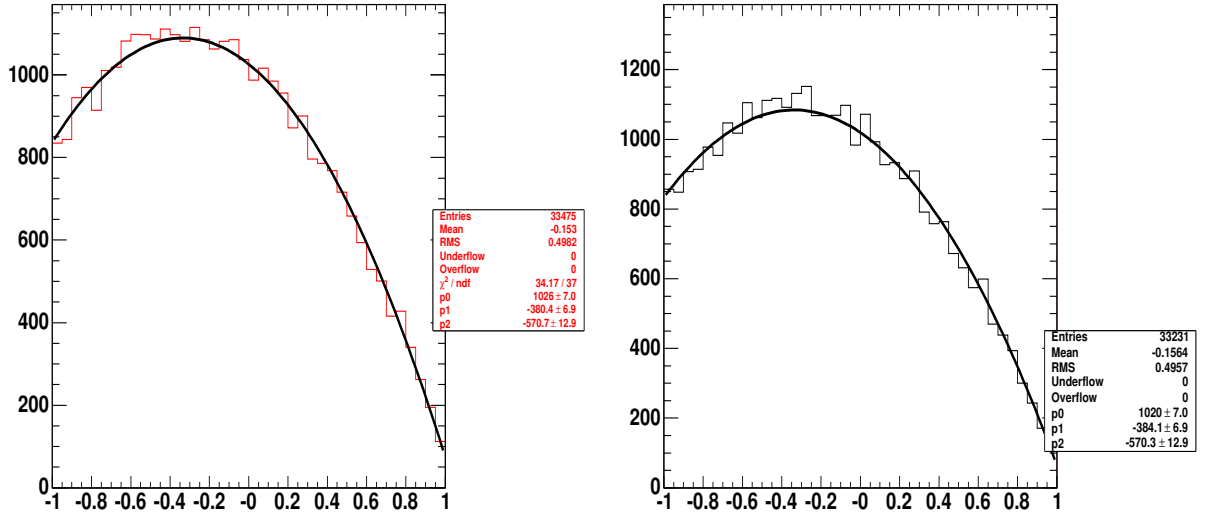


Figure 2.12: Partial and total probability densities. (a)  $\frac{dP_0}{d(\cos\alpha)} = \frac{1}{2}(1 - \cos^2\alpha)$ (top left), (b)  $\frac{dP_-}{d(\cos\alpha)} = \frac{1}{4}(1 - \cos\alpha)^2$  (top right), (c)  $\frac{dP_+}{d(\cos\alpha)} = \frac{1}{4}(1 + \cos\alpha)^2$ (bottom left) and (d)  $\frac{dP_{tot}}{d(\cos\alpha)}$ (bottom right).

Figure 2.13:  $\bar{\ell}$  helicity angle in  $t\bar{t}$ -channel and in  $t$ -channelFigure 2.14:  $\bar{\ell}$  helicity angle in  $s$ -channel and in  $\text{anoTop}$ -channel

We want to double-check whether the  $W$  polarization is properly implemented in PYTHIA and in particular whether the generation of the anomalous top quark worked properly. In Figures 2.13, 2.14 we show the distributions of  $\frac{dP_{tot}}{d(\cos\alpha)}$  for the top production processes under consideration. All of them agree well with the SM prediction. We fit the histogram with a 2nd order polynomial. The fractional occurrences used by PYTHIA can be estimated using the fit parameters of each channel and the  $\frac{dP_{tot}}{d(\cos\alpha)}$  equation. We insert (2.5), (2.6), (2.8) and (2.9) into (2.10). Under the assumption that PYTHIA has no right-handed polarization of the  $W$ ,  $f_+(W) = 0$ , the equation has one free parameter, either  $f_0(W)$  or  $f_-(W)$ . We choose here  $f_0(W)$  and replace  $f_-(W) = 1 - f_0(W)$ .

$$\frac{dP_{tot}}{d(\cos\alpha)} = \frac{1}{4}(1 + f_0(W)) + \frac{1}{2}(f_0(W) - 1)\cos\alpha + \frac{1}{4}(1 - 3f_0(W))\cos^2\alpha$$

Comparing the coefficients to those of the fit  $(p_0, p_1, p_2)$ , we are able to calculate  $f_0(W)$  and then  $f_-(W) = 1 - f_0(W)$ .

channel	$f_0(W)$	$f_-(W)$	DEV(SM) $f_0(W)$	DEV(SM) $f_-(W)$
$s$ -channel	0.687	0.313	1.6%	4.7%
$t$ -channel	0.682	0.318	2.6%	6.3%
$t\bar{t}$ -channel	0.678	0.321	3.1%	7.3%
anoTop	0.683	0.317	2.4%	5.9%

Table 2.3:  $f_0(W)$  and  $f_-(W)$  values for PYTHIA using the SM parameters ( $f_+(W) = 0$ ). DEV(SM) stands for 'deviation from Standard Model value' and is given in percent.

We find that the polarization of the top quark decay is handled correctly in our anomalous top quark sample.

# Chapter 3

## The CDF Experiment

This chapter describes the CDF Experiment situated on the accelerator at the Fermi National Accelerator Laboratory (Fermilab, FNAL). In section 3.1 the location of Fermilab as well as an overview on the accelerator facilities are presented. In section 3.2 the most important features of the CDF detector, which we use to collect the data for our analysis, are briefly discussed. These we choose to arrange in four categories: the tracking systems 3.2.1, the calorimeter systems 3.2.2, the muon systems 3.2.3 and the trigger system 3.2.4.

### 3.1 Fermilab and Tevatron



Figure 3.1: Aerial shot of the Fermilab site. Two rings of the accelerator system, the Tevatron and the Main Injector can be seen.

The Fermi National Accelerator Laboratory (Fermilab, FNAL), is located approximately 43 km west of Chicago, Illinois in the United States of America. An aerial view to the Fermilab site is shown on Figure 3.1. It covers an area of about 27.5 km<sup>2</sup>. More than 2,400 scientists from 34 states and 25 countries contribute to the research in particle

physics taking place at the Fermilab. In order to reach energies of 980 GeV per beam, a system of several accelerators is needed. Figure 3.2 gives a schematic overview of these accelerators. In the first stage of acceleration, the Cockcroft-Walton pre-accelerator is

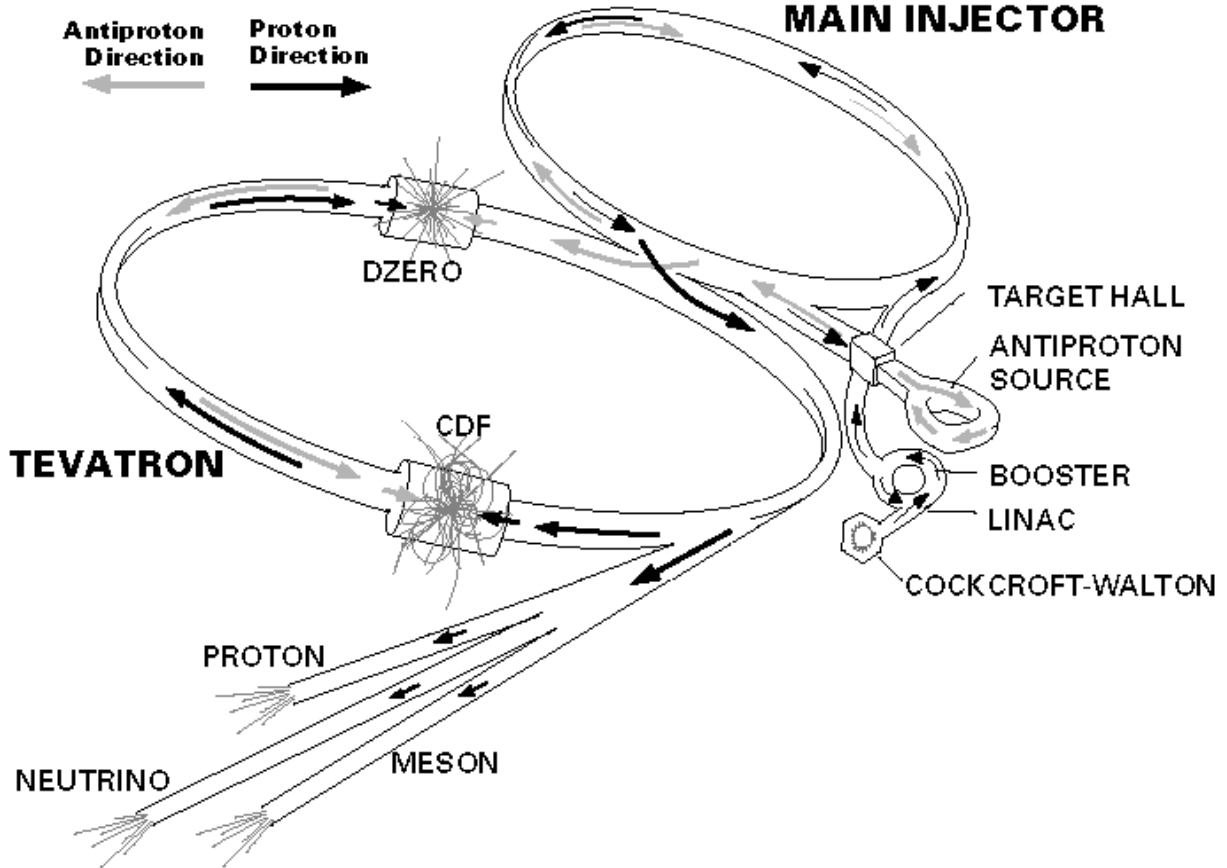
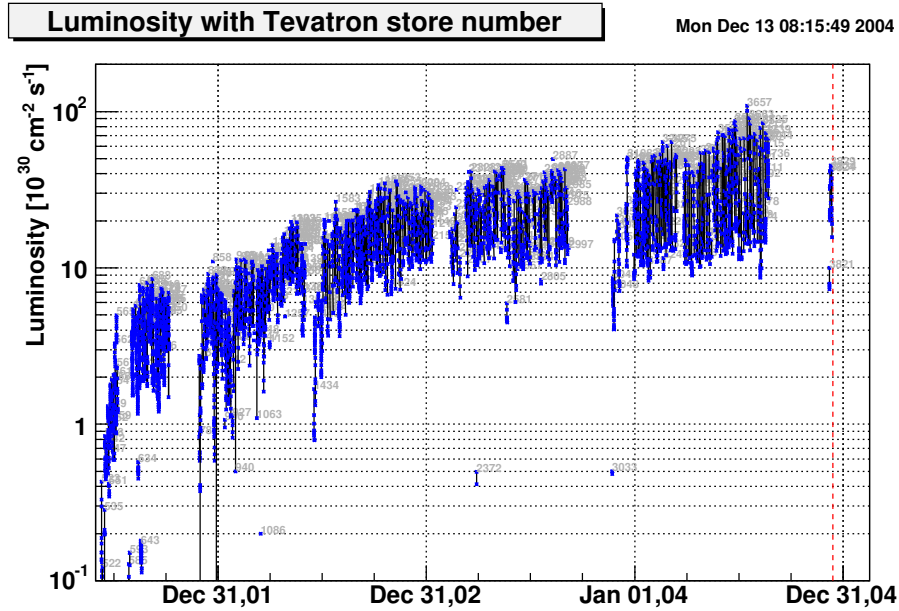


Figure 3.2: Schematic view of Fermilab's accelerators for Run II.

used to generate negative charged hydrogen ions out of hydrogen gas and then accelerate them via electric fields up to an energy of 750 keV. Afterwards, the ions enter an approximately 150 m long linear accelerator (LINAC), where they are accelerated up to 400 MeV by oscillating electric fields. Before leaving this acceleration stage, the ions pass through a carbon foil, which removes their negative charges (electrons), so that only protons remain to be promoted to the next level. Further on, the beam of protons is bent in a circular path by the magnets of a circular accelerator, called the booster. On its way out of the booster, the beam has an energy of 8 GeV. In the next stage, the protons enter the Main Injector, a multitask-accelerator completed in 1999. This machine accelerates protons up to 150 GeV, while protons with 120 GeV are used for the anti-proton production. The latters are forced to collide with a nickel target, which is installed at the Antiproton Source facility. The interactions with the target produce a variety of particles, among them many anti-protons, which are being collected, focussed and finally stored in the Accumulator Ring. As soon as a sufficient number of anti-protons has been produced, they are sent to the Main Injector, which accelerates them up to an energy of 150 GeV. In the final stage, the proton and anti-proton beams with 150 GeV

energy are injected in the Tevatron, a circular accelerator with a circumference of about 6 km, which is the most powerful operational hadron accelerator worldwide. Each beam is accelerated to an energy of 0.98 TeV which is equal to (anti-)protons reaching velocities of 0.9999995 times the speed of light. At two certain parts of the facility these beams are forced to collide with each other, producing a center of mass energy of  $\sqrt{s} = 1.96$  TeV. At each of those two collision points, experimentalists placed a detector in order to collect data from the products of the collision. One of these detectors belongs to the CDF experiment, which is also where the data for this analysis comes from. The other detector is called DØ (DZERO), also indicated in Figure 3.2. The time interval between the filling of the Tevatron with protons and anti-protons and the next filling is called a store. When dealing with colliders and their characteristics, the definition of the luminosity is useful. Luminosity is a quantity that measures the probability with which a proton collides with an anti-proton. The event rate for a certain process with cross section  $\sigma$  is given by the product  $\dot{N} = \mathcal{L} \cdot \sigma$ , while the events are given by  $N = \sigma \cdot \int \mathcal{L} dt$ .





The peak luminosity is reached at the begin of a store. Over the period of a store the luminosity slowly decreases as collisions and beam gas interactions lead to a lowering of beam currents, that is a loss of protons and anti-protons stored in the Tevatron. The maximum value of luminosity that has been achieved until December 2004 is  $11.3 \cdot 10^{31} \text{cm}^{-2} \text{s}^{-1}$ , which is 40% above the design expectation. Yet, the data that has been already understood and can be used for our analysis in Chapter 4.1 originates from the era of  $\mathcal{L}_{int} = 162 \text{ pb}^{-1}$ . The average peak luminosity in 2004 versus time, shown in Figure 3.3, is about  $6.5 \cdot 10^{31} \text{cm}^{-2} \text{s}^{-1}$ , whereas the run integrated luminosity recorded to tape (Figure 3.4) has been about  $550 \text{ pb}^{-1}$  at the end of December 2004<sup>1</sup>.

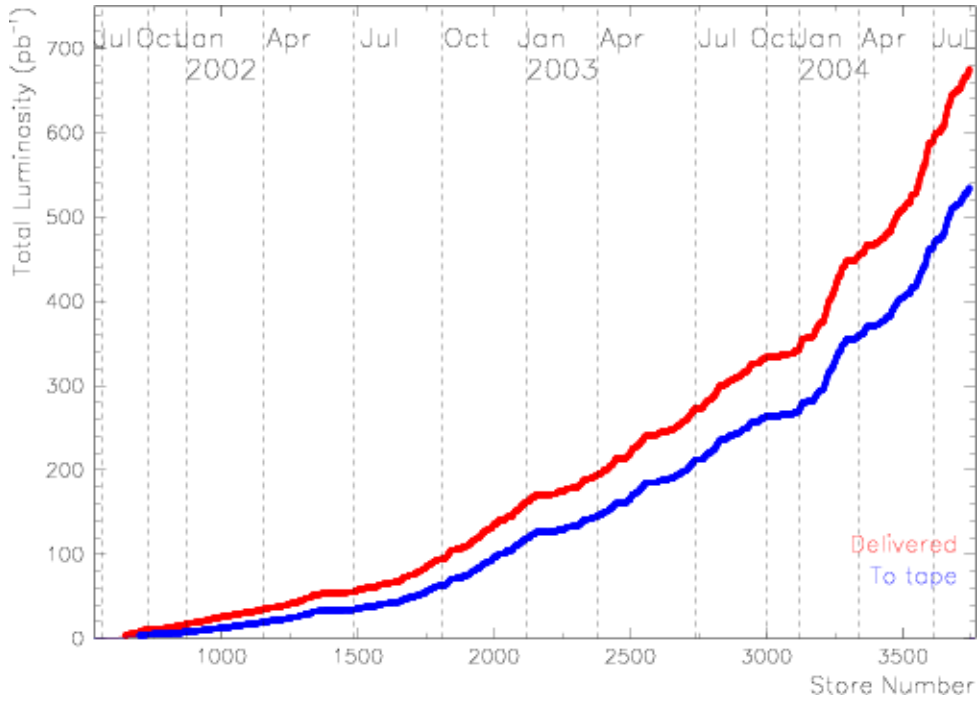


Figure 3.4: Live integrated luminosity delivered (red) and written to tape (blue) since the start of Run II.

---

<sup>1</sup>1  $\text{pb}^{-1} = 10^{36} \text{ cm}^{-2}$

## 3.2 The Collider Detector at Fermilab

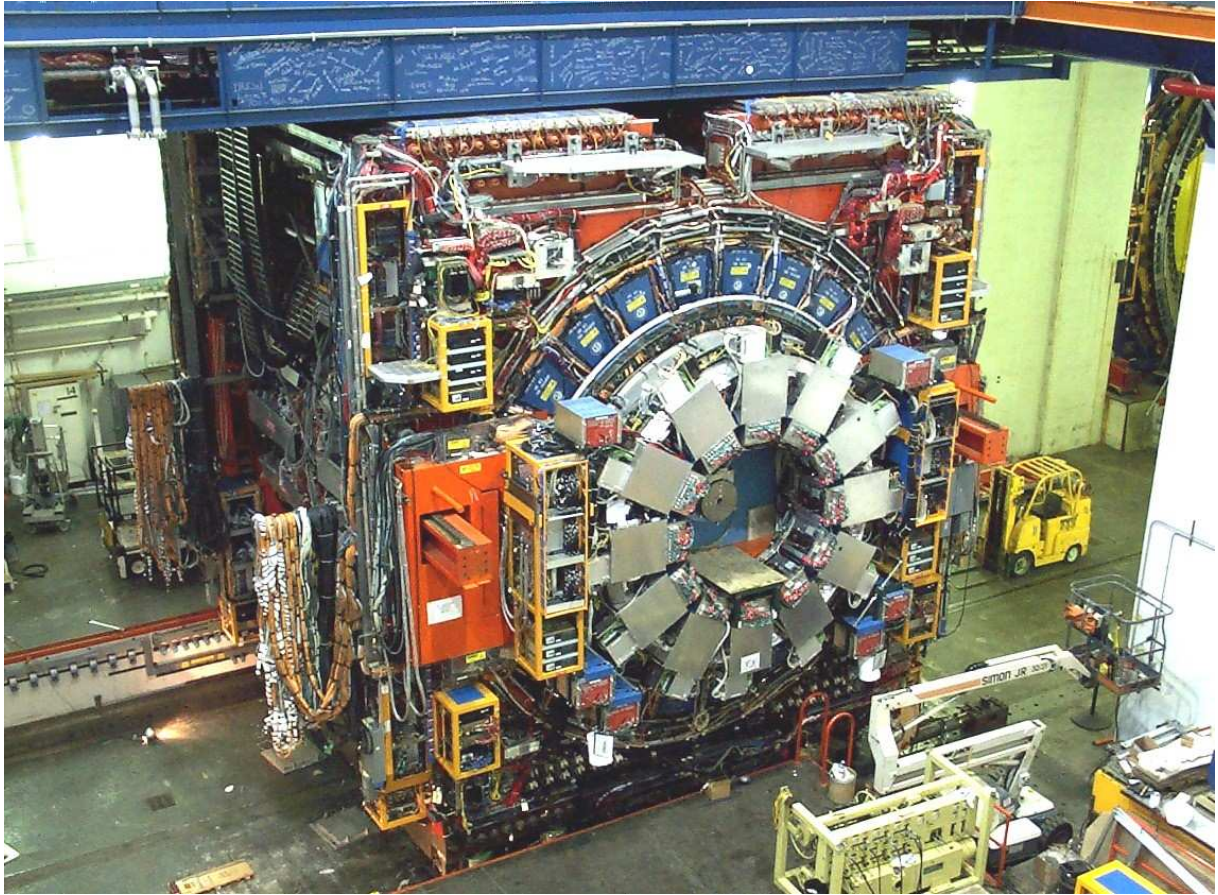


Figure 3.5: The CDF detector (while rolling in for Run II).

As already mentioned in section 3.1, the Collider Detector at Fermilab (CDF) is placed at one of the two interaction points at the Tevatron. Its purpose is to detect the resulting particles of the collisions, this means to track the charged particles and to measure the momentum and the energy of all the particles interacting with the detector material. More than 50 institutes in 11 countries build the collaboration maintaining the detector. The only German partner in this collaboration is the '*Institut für Experimentelle Kernphysik*' in Karlsruhe. Figure 3.5 shows the detector, whereas on Figures 3.6 and 3.7 a cutaway view of the detector and its inner parts is presented.

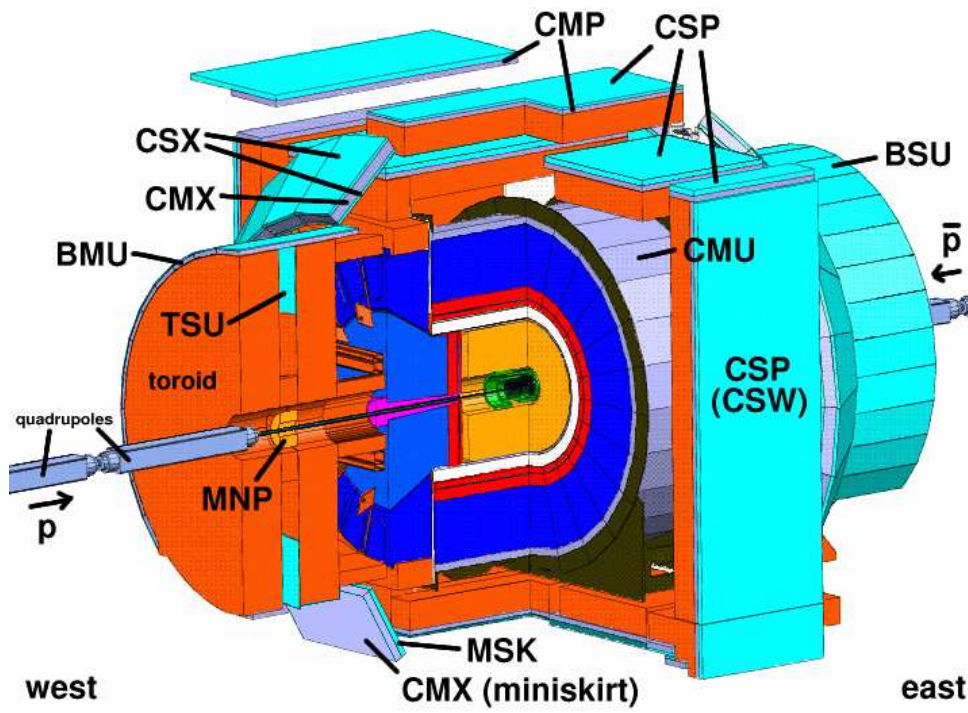


Figure 3.6: The CDF detector (cutaway view).

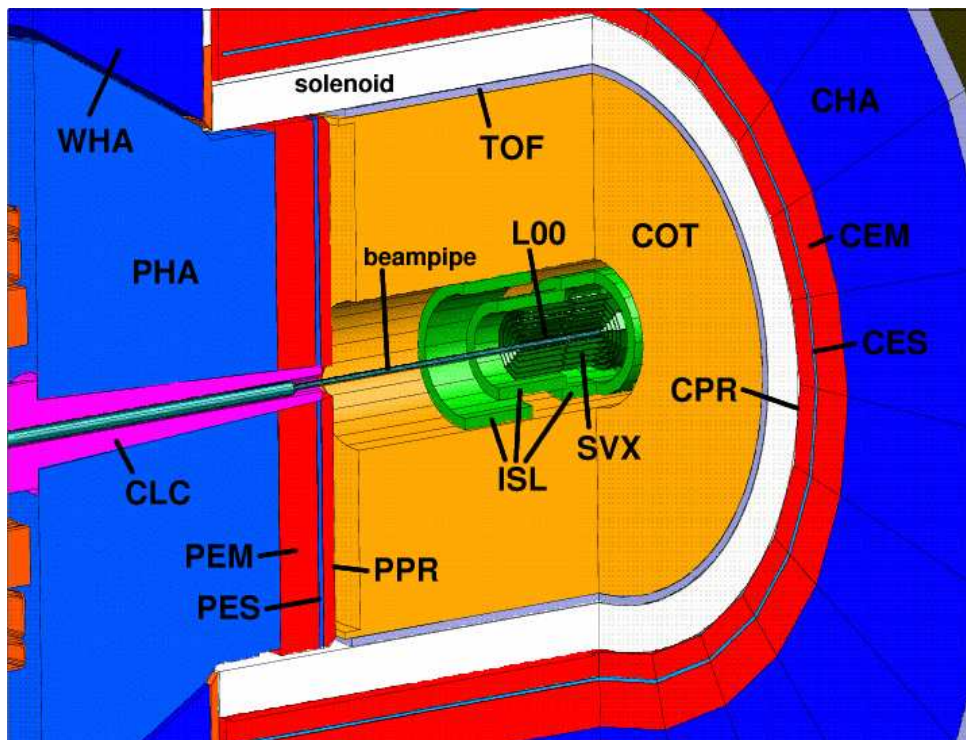


Figure 3.7: Inner parts of the CDF detector (cutaway view).



Around the Tevatron's beampipe the elements of the detector are installed cylindrically. In addition, there is a forward-backward symmetry. CDF hosts devices for tracking, for fast projective calorimetry and for muon detection. The coordinate system for CDF is defined as follows: The polar angle  $\theta$  in cylindrical coordinates is measured from the proton beam-axis (z-axis) and the azimuthal angle  $\phi$  is measured from the Tevatron plane. Instead of  $\theta$ , the pseudorapidity  $\eta$  is frequently used. The latter is defined as

$$\eta = -\ln \left( \tan \frac{\theta}{2} \right)$$

In the Technical Design Report (TDR) [31], as well as in References [32, 33, 34], a detailed description of the CDF II<sup>2</sup> detector is given. The most important parts for this analysis are summarized in the following sections.

### 3.2.1 The Tracking Systems

The devices of the tracking system are closest to the beamline. This enables them to determine the primary vertex of the event and further reconstruct charged particles. The different parts of the system are imbedded in a 1.4 Tesla magnetic field which is parallel to the beam-axis and provided by a superconducting solenoid. The solenoid is 4.8 m long and its radius is 1.5 m long. It is contained within a cryostat where it is cooled by liquid helium. The different parts of the tracking system are the silicon detectors (SVX, L00, ISL), the COT and the TOF.

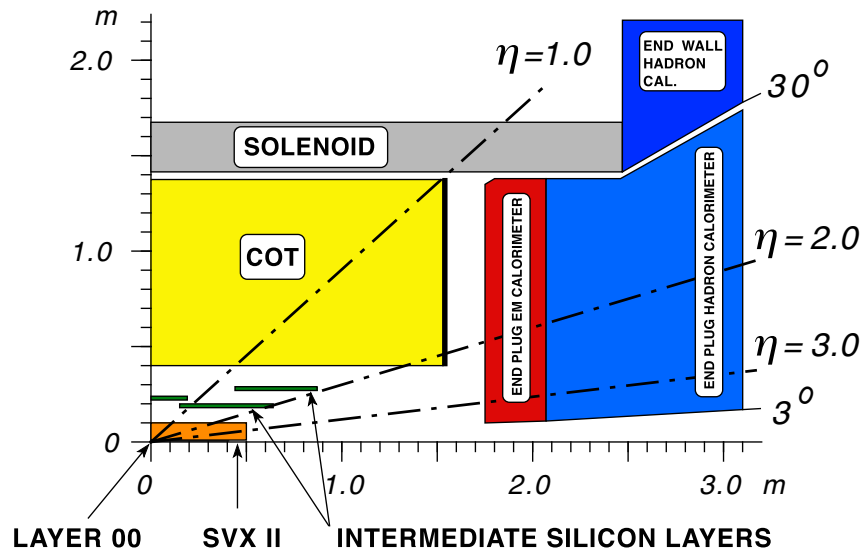


Figure 3.8: Longitudinal view of the CDF II tracking system.

- **SVX**: Silicon Vertex Detector

SVX is often called SVX II to distinguish it from its Run I predecessors, SVX and

---

<sup>2</sup>II stands for upgrade of the CDF-detector for Run II

SVX'. Its purpose is high-precision tracking and secondary vertex detection at inner radii. It extends from  $r = 2.1$  cm to  $r = 17.3$  cm and covers an area of  $|\eta| \leq 2.0$ . SVX consists of five layers of double-sided silicon microstrip detector. Strips are aligned axially on one side, with 90-degree stereo on the other side for layers 0, 1 and 3 and small-angle stereo (1.2 degrees) on the other side for layers 2 and 4. SVX's layout consists of 360 half-ladders, organized into 6 bulkheads in  $z$  (three barrels each with a bulkhead on either side), 5 layers in  $r$  and 12 wedges in  $\phi$ . Ladders in adjacent wedges overlap slightly, to provide full coverage. The individual ladders get wider in successive layers; layer 0 (the innermost layer) has 256 strips on the axial side of each ladder, while layer 4 (the outermost layer) has 896 strips on the axial side of each ladder. An end view of SVX is shown in Figure 3.9.

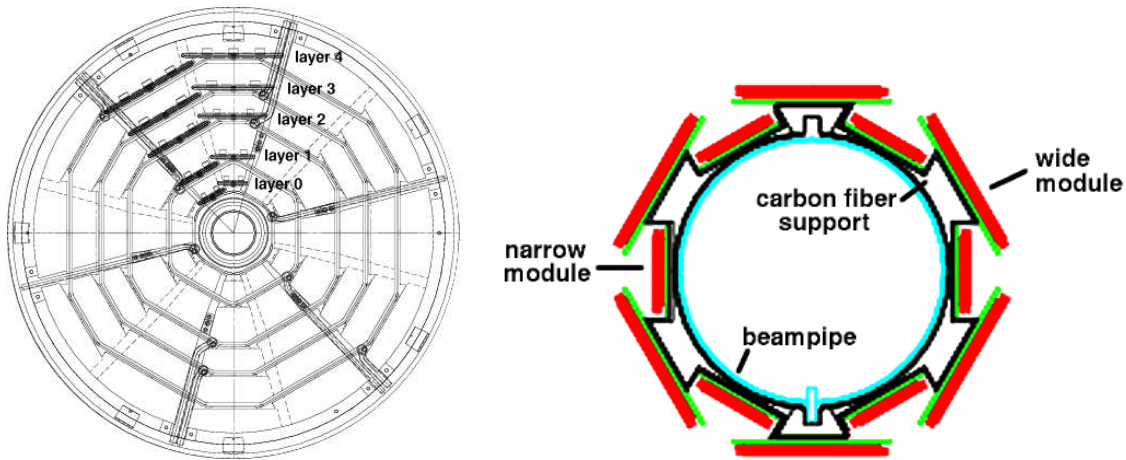


Figure 3.9: SVX bulkhead end view (left) and L00 end view (right).

- **L00:** Layer 00

L00 is used for improved precision of track measurements and b tagging efficiency. Layer 00 is placed immediately outside the beampipe at a radius of approximately  $r = 1.6$  cm and covers an area of  $|\eta| \leq 4.0$ . It was called 'Layer 00' in order to clarify that it is really the innermost layer and not confuse it with the innermost layer of SVX II (layer 0). L00 consists of 72 modules equipped with single-sided silicon microstrip detectors, with 6 modules in  $z$  and 12 staggered wedges in  $\phi$ . 6 wedges are 'narrow' modules at a radius of  $r = 1.35$  cm and 6 wedges are 'wide' modules at a radius of  $r = 1.62$  cm. The narrow and wide modules overlap for full coverage. Similar to SVX ladders, each module consists of two silicon sensors bonded together end-to-end. The narrow modules are 256 strips wide and the wide modules are 512 strips wide. Only half of these strips are read out (128 readout strips for narrow modules, 256 readout strips for wide modules). However, unlike in SVX, the readout hybrids are located outside of the tracking volume (one group on the west side to read out the west modules and one group on the east side to read out the east modules) and connected to the sensors by a fine-pitch cable. Figure 3.9 shows an end view of Layer 00.

- **ISL:** Intermediate Silicon Layer

The purpose of ISL is to provide enhanced linking of tracks between SVX II and

COT in the central region. Moreover, in the plug region, where COT coverage is incomplete, it provides improved silicon-only tracking capabilities. ISL is located between SVX II and COT. It's central layer is at  $r = 22$  cm and the forward/backward layers are at  $r = 20$  cm and  $r = 28$  cm. The central layer covers  $|\eta| < 1.0$  and the forward/backward layers cover  $1.0 < |\eta| < 2.0$ . ISL is equipped with double-sided silicon microstrip detectors (axial on one side, small-angle stereo on the other side) and also new for Run II. It consists of 296 total half-ladders. Each ladder has 1024 strips on the axial side and 768 strips on the stereo side. Only half of these are actually read out (512 axial, 384 stereo). ISL ladders are very similar to SVX, except each half-ladder consists of three silicon sensors bonded end-to-end with a single double-sided hybrid which reads out both sides of the silicon. The hybrids do not lie on the top of the silicon as they do for SVX half-ladders, but are rather attached at the end.

Table 3.1 summarizes the positions and a few important properties of the different silicon layers.

Layer	z coverage [cm]	Radius [cm]	Axial Pitch [ $\mu\text{m}$ ]	Stereo Angle [ $^\circ$ ]	Stereo Pitch [ $\mu\text{m}$ ]
00 Layer(00)	$ z  < 45$	1.35/1.62	25	-	-
0 (SVX II)	$ z  < 48$	2.53/2.98	60	90	141
1 (SVX II)	$ z  < 48$	4.11/4.56	62	90	125.5
2 (SVX II)	$ z  < 48$	6.51/6.91	60	1.2	60
3 (SVX II)	$ z  < 48$	8.21/8.71	60	90	141
4 (SVX II)	$ z  < 48$	10.13/10.68	65	-1.2	65
5 (ISL forward)	$20 <  z  < 64$	19.7/20.2	112	$\pm 1.2$	112
6 (ISL central)	$ z  < 22$	22.6/23.1	112	$\pm 1.2$	112
7 (ISL forward)	$42 <  z  < 87$	28.6/29.0	112	$\mp 1.2$	112

Table 3.1: Position and properties of the silicon system.

- **COT:** Central Outer Tracker

COT is used for general-purpose tracking in the central regions of the detector. It is placed outside of the silicon tracker, from  $r = 40$  cm to  $r = 137$  cm and covers  $|\eta| \leq 1.0$ . COT is an open-cell drift chamber with argon-ethane gas in a 50:50 mixture and provides in total 96 measurements. It replaces the Run I Central Tracking Chamber (CTC) and features a greater number of sense wires (about five times more), enhanced stereo coverage and faster drift times. It consists of 2520 cells which are divided into 8 superlayers. The number of cells in each superlayer ranges from 168 for SL1 to 480 for SL8. Superlayers 2, 4, 6 and 8 are axial (wires parallel to the beam) while superlayers 1, 3, 5 and 7 are at a small stereo angle (2 degrees). Each cell has a wire plane containing 12 sense wires and 13 potential wires, with two additional shaper wires at either end. Wire planes are separated by gold-on-Mylar field panels with stainless steel wires at either end. Cells are installed at a 35-degree Lorentz angle.

- **TOF**: Time-of-Flight Detector

TOF is designed to collect time-of-flight information in order to enhance particle identification abilities in the central detector, especially for improving  $K-\pi$  discrimination. It is placed outside of COT, at an approximate radius of 140 cm. TOF is a scintillator read out by PMTs via lightguides and new for Run II. It consists of 216 bars of scintillator, each running the length of COT, arranged cylindrically with a PMT at each end of each bar. PMTs 0 to 215 are on the east side and 216 to 431 are on the west side. The bars have a trapezoidal cross section in order to minimize empty space between them.

### 3.2.2 The Calorimeter Systems

The calorimeter systems are located outside of the magnetic field of the solenoid. We distinguish between electromagnetic and hadronic calorimeter systems. The calorimeters are designed to absorb fully the kinetic energy of the particles except for the case that these particles are muons or neutrinos. They cover the range of  $-3.6 < \eta < 3.6$  and  $0 < \phi < 2\pi$ . The whole system is built up in segments and consists of five different types of calorimeter (CEM, CHA, WHA, PEM and PHA):

- **CEM**: Central Electromagnetic Calorimeter

CEM's purpose is to measure the energy of the electromagnetic showers in the central detector. It is placed outside of the solenoid in the central part of the detector and covers the region of  $|\eta| < 1.1$ . CEM is a Pb/scintillator sampling calorimeter, 31 layers deep. It consists of 478 towers, which are organized into 24 wedges in  $\phi$  and 10 tower groups in  $\eta$  on each side. Towers 8E and 9E in wedge 5 are removed for cryogenic utilities for the solenoid. Each tower is read out by two PMTs, one at the low- $\phi$  side of the tower and one at the high- $\phi$  side. These are typically called 'left' and 'right', respectively, with the directions defined as with the wedge upright, looking from  $z=0$  towards the wedge. The cryogenic 'chimney' (a space left for cables and cryogenic utilities for the solenoid) is located in wedge 5E. Towers 8 and 9 are removed for the chimney and tower 7 is slightly bigger to compensate.

- **CHA**: Central Hadronic Calorimeter

CHA is used to measure the energy produced by hadronic showers in the central detector. It is located in the central detector outside of CEM and covers the area of  $|\eta| < 0.9$ . CHA is a Fe/scintillator sampling calorimeter, 32 layers deep. It consists of 384 towers, organized into 24 wedges in  $\phi$  and 8 tower groups in  $\eta$  on each side. Each tower is read out by 2 PMTs. The chimney also runs through wedge 5E of CHA. Towers 6 and 7 have a notch cut out and only one PMT.

- **WHA**: Endwall Hadronic Calorimeter

WHA is used as an extension of hadronic calorimeter coverage to the endwall region. It is placed along the endwall outside of the plug and covers the region of  $0.8 < |\eta| < 1.2$ . WHA is also a Fe/scintillator sampling calorimeter, but only 15 layers deep. It consists of 288 towers that are organized into 24 wedges in  $\phi$  and 6 tower groups in  $\eta$  on each side. Each tower is read out by 2 PMTs.

- **PEM**: Plug Electromagnetic Calorimeter

PEM measures the energy coming from the electromagnetic showers in the plug

region of the detector. It is placed outside the barrel end of COT, one plug on each side, and covers the area of  $1.1 < |\eta| < 3.6$ . PEM is a Pb/scintillator sampling calorimeter, 23 layers deep and is new for Run II. It consists of 480 towers per plug, organized into 12 tower groups in  $\eta$ . The innermost 4 tower groups (largest  $\eta$ /smallest  $\theta$ ) each have 24 wedges in  $\phi$  (each tower covers 15 degrees). The outermost 8 tower groups each have 48 wedges in  $\phi$  (each covering 7.5 degrees).

- **PHA:** Plug Hadronic Calorimeter

PHA is used to measure the hadronic showers in the plug region of the detector. It is placed beyond PEM and covers  $1.2 < |\eta| < 3.6$ . PHA is a Fe/scintillator sampling calorimeter, 23 layers deep and new for Run II. It consists of 432 towers per plug, organized into 11 tower groups in  $\eta$ . The arrangement is the same as for PEM except the outermost tower group (smallest  $\eta$ /largest  $\theta$ ) does not exist (this area is already covered by WHA).

Tables 3.2 and 3.3 show an overview of the calorimeter properties.

Calorimeter	abbreviation	$ \eta $ range	Energy resolution
Central Electromagnetic	CEM	$ \eta  < 1.1$	$13.7\%/\sqrt{E} \oplus 2\%$
End-Plug Electromagnetic	PEM	$1.1 <  \eta  < 3.6$	$16\%/\sqrt{E} \oplus 1\%$
Central Hadron	CHA	$ \eta  < 0.9$	$50\%/\sqrt{E} \oplus 2\%$
End Wall Hadron	WHA	$0.9 <  \eta  < 1.3$	$75\%/\sqrt{E} \oplus 4\%$
End-Plug Hadron	PHA	$1.3 <  \eta  < 3.6$	$80\%/\sqrt{E} \oplus 5\%$

Table 3.2: Overview of the calorimeter properties. The symbol  $\oplus$  implies that the constant term is added in quadrature. The energy is given in GeV. The energy resolutions for the electromagnetic calorimeters are for incident electrons and photons and for the hadronic calorimeters for incident isolated pions.

$ \eta $ range	$ \Delta\phi $	$\Delta\eta$	Calorimeter
$ \eta  < 1.3$	$15^\circ$	$\sim 0.1$	Central and End Wall
$1.1 <  \eta  < 1.2$	$7.5^\circ$	$\sim 0.1$	End-Plug Electromagnetic
$1.2 <  \eta  < 1.8$	$7.5^\circ$	$\sim 0.1$	End-Plug Electromagnetic & Hadron
$1.8 <  \eta  < 2.1$	$7.5^\circ$	$\sim 0.1$	
$1.8 <  \eta  < 2.1$	$7.5^\circ$	$\sim 0.15$	
$2.1 <  \eta  < 3.6$	$15^\circ$	$0.2-0.6$	

Table 3.3: Segmentation and range of the different calorimeter systems.

### 3.2.3 The Muon Systems

In order to reconstruct the muons with sufficient  $p_T$  which may traverse the calorimeters, muon detectors are placed outside the hadronic calorimeter systems. The most important parts of the muon detection system are the muon chambers (CMU, CMP, CMX, BMU) and the muon scintillators (CSP, CSW, CSX, MSX (MSK), BSU, TSU):



- **CMU**:Central Muon Chambers

CMU is used to detect muons in the central detector region. It is located at the outside edge of CHA wedges and covers  $|\eta| < 0.6$ . CMU is a wire chamber operated in proportional mode. It consists of 2304 cells, organized into 144 modules. There are 3 modules per CHA wedge per side. Each module is composed of 16 cells arranged in 4 radial layers of 4 cells each. Each cell contains one sense wire and runs the length of the wedge on one side.

- **CMP**:Central Muon Upgrade

The purpose of CMP is to confirm the CMU tracks. Since CMP is behind more material, CMP hits have a higher signal-to-background ratio and increase the trigger efficiency of the CMU/CMP combination. CMP is placed along the walls, floor and top surface of CDF. It also covers an area of  $|\eta| < 0.6$ . The central muon upgrade is a wire chamber operated in proportional mode. It consists of 1068 cells which are arranged in 4 layers. There are 77 stacks along the top, 65 along the bottom, 62 on the north wall and 63 on the south wall. Unlike the other detectors in CDF, which are all (mostly) cylindrically symmetric around the beampipe, CMP is roughly box-shaped. This is because CMP uses the magnet return yoke steel as absorbing steel, along with some additional pieces of steel to fill gaps in the existing steel.

- **CMX**:Central Muon Extension

CMX is used as an extension of central muon coverage to  $\eta = 1.0$ . It is a truncated cone covering the area between BMU and CMP. CMX is a wire chamber operated in proportional mode and covers  $0.6 < |\eta| < 1.0$ . CMX is divided into two parts: the upper conical section, which covers the upper 270 degrees in  $\phi$ , and the part of the lower 90 degrees in  $\phi$ , which has a slightly different geometry due to the floor. The second part is called the 'miniskirt'. The conical section contains 1632 cells, 864 on the west and 768 on the east side, divided into 18 wedges in  $\phi$  (each covering 15 degrees). The miniskirt contains 576 cells, 288 per side.

- **BMU**:Barrel Muon Chambers

BMU is used to detect muons in the forward region. It is located on the outside of the toroids and covers the area of  $1.0 < |\eta| < 1.5$ . BMU is a wire chamber operated in proportional mode and is new for Run II. It consists of 1728 chambers, 864 per toroid, arranged into 4 layers with 216 chambers per layer. Each chamber occupies 1.25 degrees of  $\phi$ . The bottom 90 degrees of the barrel are not covered due to the support structures for the toroids (these are placed outside the plugs).

- **CSP**:Central Scintillator Upgrade

- **CSW**:CSP Wall Scintillators

CSW is user for fast timing and trigger counters for CMU/CMP muons. It is located on the outside of the CMP chambers. CSW consists of 269 scintillator tiles. Each tile covers 2 CMP chambers in width and one-half chamber in length.

- **CSX**:Central Scintillator Extension

CSX serves the same purpose as CSW (CSP), only for the CMX muons (in the conical section). It is placed on both surfaces of the CMX chambers. CSX consists

of 272 scintillator tiles, with four tiles on either side of each CSX wedge. CSX Internal refers to the tiles on the inner side and CSX External refers to the tiles on the outer side. CSX only covers the upper 270 degrees of CMX, not the miniskirt (see MSK).

- **MSX (MSK):CMX Miniskirt Scintillators**

MSX has the same function as CSX, only for the muons in the miniskirt section of CMX. It is placed on the inner surface of CMX miniskirt chambers. It consists of one scintillator tile on the inner surface of each CMX miniskirt chamber and is new for Run II.

- **BSU:Barrel Scintillator Upgrade**

BSU is used for the same purpose as CSW, only for BMU muons. It is located on the outer surface of the BMU chambers. BSU consists of scintillator tiles and is new for Run II. There are in total 432 counters, 216 per side. Each tile covers 2 BMU chambers in azimuth (2.5 degree in  $\phi$ ) and half of the length of each BMU chamber. BSU Front covers the half closer to the interaction point and BSU Rear the further half.

- **TSU:Toroid Scintillator Upgrade**

TSU provides additional triggering powers for forward muons. It is placed on the inner face of the toroids. TSU consists of scintillator tiles and is also new for Run II. There are 144 counters, 72 per side, each covering 5 degrees in  $\phi$ , arranged in a circle.

The combination BSU+TSU is often referred to as **ISU** (**I**ntermediate **S**cintillator **U**ppgrade), while BSU+TSU+BMU makes the **IMU** (**I**ntermediate **M**uon **D**etector). Table 3.4 summarizes the  $\eta$  coverage and the minimal  $p_T$  the muon needs to be detectable in some of the muon detectors.

	CMU	CMP/CSP	CMX/CSX	IMU
Pseudorapidity coverage	$ \eta  < 0.6$	$ \eta  < 0.6$	$0.6 <  \eta  < 1.0$	$1.0 <  \eta  < 1.5$
Min $p_T$ of detectable $\mu$	1.4 GeV/c	2.2 GeV/c	1.4 GeV/c	1.4-2.0 GeV/c

Table 3.4:  $\eta$  coverage and the minimal  $p_T$  for a muon to reach the detector for some parts of the muon system.

### 3.2.4 The Trigger Systems

The trigger plays an important role to efficiently extract the most interesting physics' events from the large number of minimum bias events, because the collision rate will be equal to the crossing rate of 2.5 MHz, while the tape writing speed is about 75 MHz. The CDF trigger is a three level system. Each level provides a sufficient rate reduction for the processing of the next level.

The basic design of the CDF trigger upgrade consists of 2 hardware levels both of which are buffered. Figure 3.10 shows the dataflow and buffering for the DAQ and trigger paths in the upgrade. Data to be used in the Level 1 (L1) trigger is digitized every beam crossing and sent to the L1 portion of the trigger. While the L1 trigger decision is being made, all

data from the detector is stored in L1 buffers for readout and/or use at Level 2 (L2). On a L1 accept the data from the L1 buffer is passed to a L2 buffer and the event is queued for a L2 decision. On a L2 accept the L2 buffer for that event is queued for readout into the L3 processor farm. After readout or on a L2 reject the L2 buffer is freed for use by a later L1 accept. Trigger decisions are based on information from calorimeter towers (CAL), central strip chambers (CES), central tracking chamber (CTC), muon chambers and muon scintillators and silicon vertex detector.

- **Level 1:** The Level 1 trigger is a synchronous system with an event read in every beam crossing and a decision (L1 accept/L1 reject) made every beam crossing. The depth of the L1 decision pipeline is approximately  $4\ \mu s$  (L1 Latency). The L1 buffers must be at least as deep as this processing pipeline or the data associated with a particular L1 decision would be lost before the decision is made. At a bunch spacing of  $396\ ns$ , a buffer 32 events deep provides storage for  $4224\ ns$ . The L1 buffer is 42 crossings deep ( $5544\ ns$ ) to provide a margin for unanticipated increases in the L1 latency. The equivalent depth with a  $396\ ns$  bunch spacing is 14 crossings.
- **Level 2:** The Level 2 is an asynchronous system which processes events that have received a L1 accept in a time ordered fashion. It is structured as a two stage pipeline with data buffering at the input of each stage. The first stage is based on dedicated hardware processors which assemble information from a particular section of the detector (Calorimeter Clusters, SVX tracks etc.). The second stage consists of programmable processors (DEC Alpha processors) operating on lists of objects generated by the first stage. Each of the L2 stages is expected to take approximately  $10\ \mu s$  giving a latency of about  $20\ \mu s$ .
- **Level 3:** The Level 3 processor farm reconstructs the full event using the complete event data. After the reconstruction they are filtered after pre-defined criteria and written to tape permanently. Within these three trigger steps, a writing frequency of 75 events per second remains.

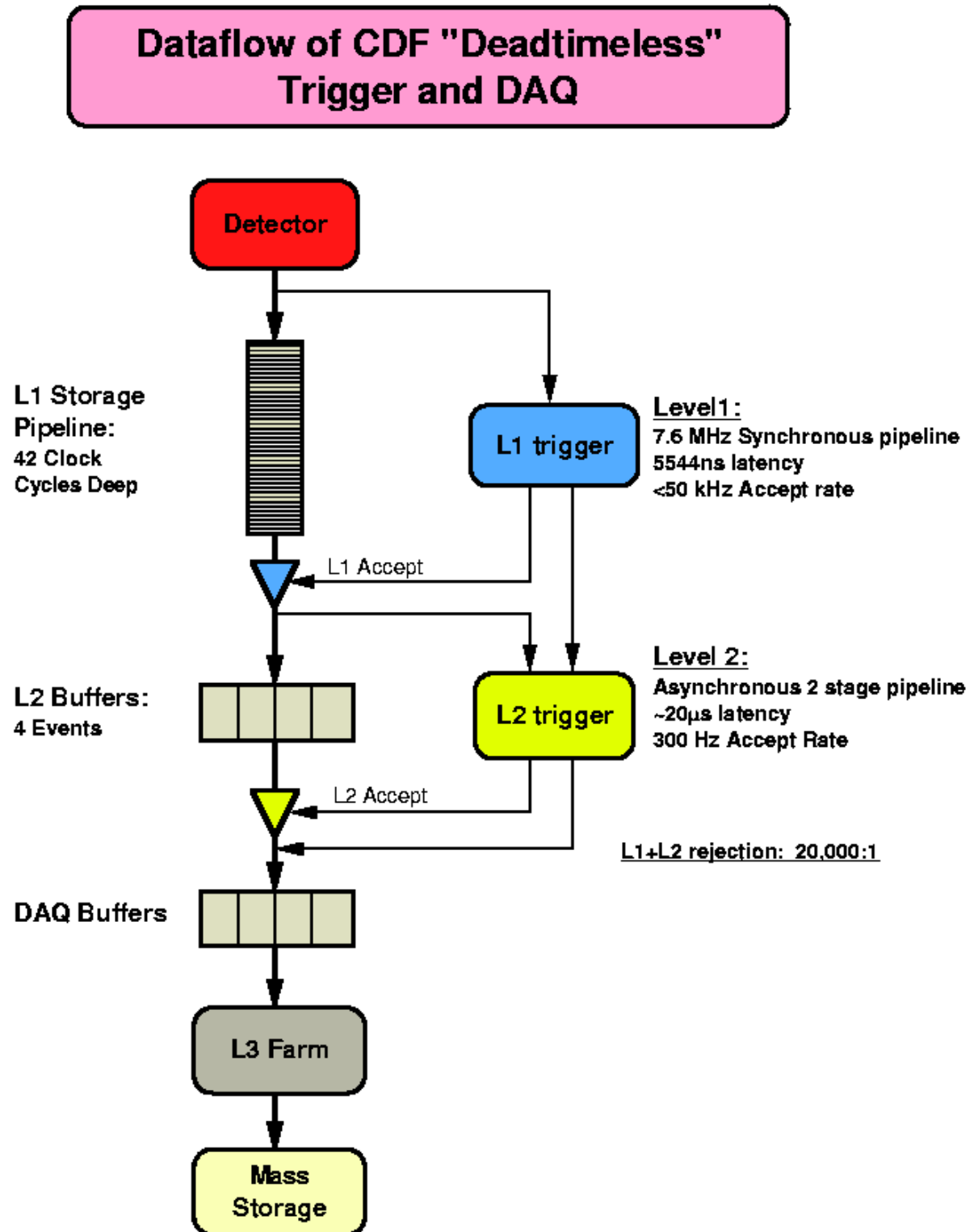


Figure 3.10: Run II readout functional block diagram.

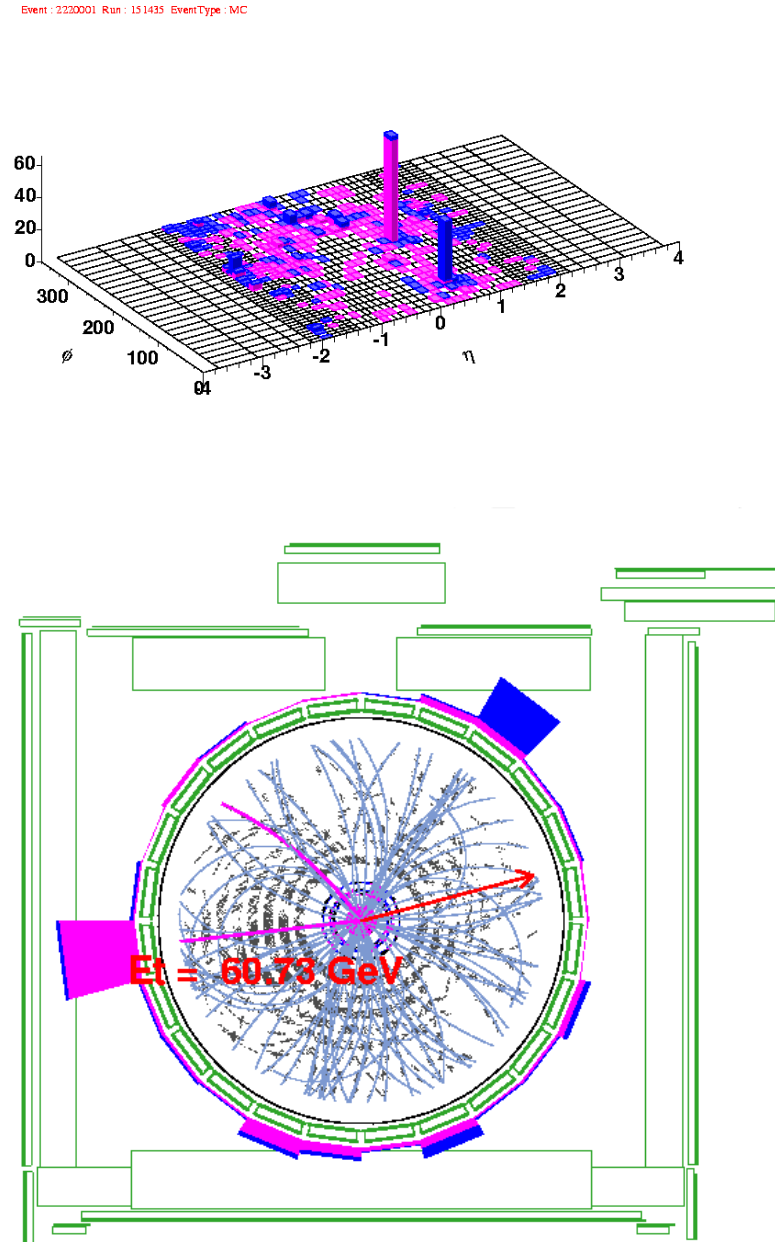


Figure 3.11: A simulated anomalous top event as it would be seen in the COT and the calorimeter (bottom). The color code is blue for the hadronic calorimeter and magenta for the electromagnetic calorimeter, see section 3.2.2. The size of the colored clusters is proportional to the energy deposition. In this event, the highest cluster contains 60.73 GeV resulting mostly from electromagnetic energy. This is the tower that the isolated electron, originating from the W decay, deposited its energy. The missing  $E_T$  vector, that points to the upper right side, represents the neutrino. At the top, the same event is demonstrated on the  $\eta$ - $\phi$  plane. The energy is given by the vertical-axis.

# Chapter 4

## Data analysis

### 4.1 Detector Simulation

In this section we follow the method and the cuts used by the CDF single top group and can be found in References [49, 50].

#### 4.1.1 Monte Carlo Samples and Selection Requirements

The anomalous top, the  $t\bar{t}$  and the di-boson Monte Carlo samples, used for this analysis, are generated with PYTHIA [26]. The single top samples are generated with MadEvent [46], whereas the  $W$ +heavy flavor and the mistags samples are generated with Alpgen [47]. Simulation and production were performed in the 4.9.1 release of the CDF offline software. We used the *runMc* executable, 4.9.1 version 11. The reconstructed events were passed through TopFind, linked against CDF software release 4.11.1, to produce TopN-tuples [48]. Table 4.1 gives an overview on the samples we use.

##### 4.1.1.1 Baseline Cuts

The selection requirements used are the standard cuts of the lepton+jets working group. We first require the events to have the OBSV vertex in the fiducial volume of the detector:  $|z_0| < 60\text{cm}$ . The tight lepton selections are given in Table 4.2<sup>1</sup>:

##### 4.1.1.2 Top Mass Reconstruction

One important requirement to establish the production of a certain elementary particle is to reconstruct one of its most distinct features, its invariant mass. In the standard model top quark decay is dominated by the mode  $t \rightarrow W^+ + b$ , which has a branching ratio close to 100%. In our analysis we reconstruct leptonic  $W$  boson decays. We therefore reconstruct  $M_{\ell\nu b}$  as an estimator for  $m_{top}$ .

**b-jet assignment:** The first step to calculate the top quark mass is to reconstruct the  $b$  quark 4-momentum vector. Our event selection criteria require at least one  $b$ -tagged<sup>2</sup> jet to be present. If there is one and only one  $b$  tagged jet in the event, this jet is used for top

---

<sup>1</sup>a more detailed description of these cuts is given in [35]

<sup>2</sup> $b$ -tagging: at least one jet must be identified as containing a  $b$  hadron from the presence of a secondary vertex

Process	MC Generator	Sample	Description	N ntup.
$anoTop$	PYTHIA	utopg0	anomalous top	695933
$t\bar{t}$	PYTHIA	ttopei	standard, no filter	398037
$t - channel$	MadEvent	mtop0s/1s	LO $2 \rightarrow 2$ /NLO $2 \rightarrow 3$	163237
$s - channel$	MadEvent	mtop2s	LO	199953
$WW0p$	PYTHIA	atop4x	$W_1 \rightarrow e, \mu, \tau$	944969
$WZ0p$	PYTHIA	atop0y	$W_1 \rightarrow e, \mu, \tau$	191011
$ZZ0p$	PYTHIA	atop0z	$W_1 \rightarrow e, \mu, \tau$	223606
$W\ell\nu BB0p$	Alpgen	atop40	$W$ leptonic decay	219847
$W\mu\nu BB0p$	Alpgen	atop46	$W$ leptonic decay	219847
$W\tau\nu BB0p$	Alpgen	atop4c	$W$ leptonic decay	219846
$W\ell\nu CC0p$	Alpgen	atop43	$W$ leptonic decay	252902
$W\mu\nu CC0p$	Alpgen	atop49	$W$ leptonic decay	252903
$W\ell\nu C10p$	Alpgen	atop0w	$W$ leptonic decay	200001
$W\mu\nu C1p$	Alpgen	atop3w	$W$ leptonic decay	179953
$W\ell\nu 2p$	Alpgen	atop02	mistags	189094
$W\mu\nu 2p$	Alpgen	atop08	mistags	260000
$W\tau\nu 2p$	Alpgen	atop2e	mistags	293736

Table 4.1: Monte Carlo samples used in the anomalous top analysis.

Selection Cut for CEM electrons	Selection Cuts for CMUP and CMX muons
CEM electron Fiducial $E_T \geq 20.0$ GeV	CMUP muon CMX muon $p_T \geq 20.0$ GeV/c
$p_T \geq 10.0$ GeV $E_{had}/E_{em} \leq 0.055 + 0.00045E$ $L_{shr} \leq 0.2$ $E/P \leq 2.0$ .OR. $p_T > 50$ GeV $ z_0  \leq 60.0$ cm $ \Delta z  \leq 3.0$ cm $-3.0 \leq Q \cdot \Delta x \leq 1.5$ (cm) $\chi^2_{strip} \leq 10.0$ Good COT Axial Segments $\geq 3$ Good COT Stereo Segments $\geq 3$	$E_{had} \leq \max(6, 6 + 0.0280(p - 100))$ $E_{em} \leq \max(2, 2 + 0.0115(p - 100))$ $ z_0  \leq 60.0$ cm CMU $ \Delta z  \leq 3.0$ cm (for CMUP muons only) CMP $ \Delta z  \leq 5.0$ cm (for CMUP muons only) CMX $ \Delta z  \leq 6.0$ cm (for CMX muons only) Good COT Axial Segments $\geq 3$ Good COT Stereo Segments $\geq 3$ $ d_0  \leq 0.2$ cm if no Si hits $ d_0  \leq 0.02$ cm if Si hits
Isolation $\leq 0.1$	Isolation $\leq 0.1$
Conversion Veto	Conversion Veto (for data only)

Table 4.2: The baseline cuts for CEM electrons, CMUP and CMX muons for Run II analyses, taken from [35].

mass reconstruction. If there are more  $b$ -tagged jets, we pick the  $b$ -jet which has maximum  $Q\eta$ .  $Q$  is the lepton charge (in units of the elementary charge  $e$ ) and is used to tag top and anti-top events.  $\eta$  is the pseudo-rapidity of the  $b$ -jet. The  $b$ -jet 3-momentum vector

$\vec{p}$  is corrected by a scale factor obtained from the jet corrections. We use jet corrections level 7, which includes all available corrections. We set the  $b$ -jet mass to  $m_{b\text{-jet}} = 5$  GeV, and calculate the energy:  $E_b^2 = m_{b\text{-jet}}^2 + \vec{p}^2$ .

The second step is to reconstruct the  $W$  boson 4-momentum. Our event selection is such that we allow one and only one tight charged lepton ( $e$  or  $\mu$ ) in our events. The neutrino remains undetected. In reasonably good approximation the transverse momentum,  $\vec{p}_T$ , of the neutrino is given by the missing transverse energy  $\cancel{E}_T$ , as obtained from calorimeter information. To improve the precision on the  $\cancel{E}_T$  measurement three corrections are applied. The first two are the same as described in section 4.1.1.1. The jet energy correction, however, has to be consistent with the fact that we use level 7 corrections for the  $b$ -jet. In contrast to the  $\cancel{E}_T$  corrections described in section 4.1.1.1 we therefore use correction level 6 for the jets. We do not use level 7 corrections because they include out-of-cone corrections. Using them in the  $\cancel{E}_T$  calculation would mean double-counting out-of-cone energies.

**Calculating the neutrino  $p_z$  component:** The  $z$ -component of the neutrino momentum is unknown. However, under the assumption that we are dealing with a real leptonic  $W$  boson event the neutrino  $p_z$  can be calculated up to a two-fold uncertainty using the following kinematic constraints:

$$p_\mu(W) = p_\mu(\ell) + p_\mu(\nu) \quad p_\mu(\nu)p^\mu(\nu) = 0 \quad (4.1)$$

Solving for  $p_z(\nu)$  gives:

$$p_z(\nu) = \frac{\kappa p_z(\ell)}{E^2(\ell) - p_z^2(\ell)} \pm \frac{1}{2(E^2(\ell) - p_z^2(\ell))} \cdot \sqrt{(2\kappa p_z(\ell))^2 - 4(E^2(\ell)p_T^2(\nu) - \kappa^2) \cdot (E^2(\ell) - p_z^2(\ell))} \quad (4.2)$$

$$\text{with } \kappa = 0.5(M_W^2 - m_\ell^2) + \cos(\phi_\ell - \phi_\nu) \cdot p_T(\ell)p_T(\nu) \quad (4.3)$$

For the calculation we use  $p_T(\nu) = \cancel{E}_T$ . Out of the two solutions we choose the one which has the smallest absolute value. If the  $p_z$  turns out to be complex with non-zero imaginary part (the expression beneath the square root is negative) we use only the real part of  $p_z$ . That happens in about 30% of the cases (for single top production; number obtained from Monte Carlo) due to detector mismeasurements (fully compatible with the detector resolution). We use  $M_W = 80.448$  GeV,  $m_\mu = 0.105658$  GeV and  $m_e = 0.000511$  GeV. We calculate the neutrino energy using:

$$E(\nu) = \sqrt{\cancel{E}_T^2 + p_z^2} \quad (4.4)$$

We calculate the invariant mass of the charged lepton, the neutrino and the  $b$ -jet  $M_{\ell\nu b}$  which for signal events estimates the top quark mass.

## 4.1.2 Signal Acceptances

### 4.1.2.1 Cut Flow

Following is a brief discussion of the sequence of cuts used in this study. The cut flow is shown in Tables 4.3, 4.4 and 4.5. The number of Monte Carlo generated events is



given in the line name **Total**. We first select events which have the OBSV vertex in the fiducial volume of the detector:  $|z_0| < 60$  cm. We then select events which have at least one tight electron according to the TopEventModule classification. Next we impose the additional lepton identification requirements. For the  $\cancel{E}_T$  selection we apply jet corrections as described in section 4.1.1.1. We require one and only one tight lepton per event, which we call **Tight Di-Lepton Veto**. After the di-lepton veto we subdivide the events in three categories according to the subsystem where the tight lepton was detected: **CEM**, **CMUP** and **CMX**. We also veto events which have an additional Phoenix electron in the plug, **PHX Veto**. For **CEM** events there is an additional conversion veto. In addition, we apply a  $Z^0$  veto which is described in Ref.[35]. The number of events passing the requirement  $\cancel{E}_T \geq 20$  GeV is given in the line **Missing Et**. The number of events that have a positive tag for at least one taggable jet is given in the line denoted **b tag $\geq 1$** . The final requirement concerns the reconstructed top quark mass  $M_{\ell\nu b}$ , and retains only events in which  $120 < M_{\ell\nu b} < 230$  (GeV/c<sup>2</sup>). We also apply an additional cut: We require at least one jet to have  $E_T > 30$  GeV.

### 4.1.3 Background

The following chapters concern the background channels considered in our analysis. These consist of the standard model top quark production channels, which are explained in section 4.1.3.1 and the non-top background channels, including the di-boson channels (section 4.1.3.2), the  $W$ +heavy flavor channels, the non- $W$  events and the mistags (section 4.1.3.3). We chose to distinguish between the di-boson and the rest non-top background, since there is a theoretical prediction for the cross section of the di-boson processes, which led us to treat them with a different method than the rest of the non-top background processes.

#### 4.1.3.1 SM Top Quark Background

The standard model predicts two ways in which a top quark may be produced as already explained in section 1.3.1. The  $t\bar{t}$  production and the single top production, which consists of the  $s$ -channel and the  $t$ -channel.

- **$t\bar{t}$  cross section**: In  $p\bar{p}$  collisions at  $\sqrt{s} = 1.96$  TeV top quark production is dominated by  $t\bar{t}$  production via the strong interaction. Quark-antiquark annihilation is the dominating sub-process, contributing about 85% of the cross section. Following the CDF single top analysis, we use  $\sigma_{t\bar{t}} = (6.70 \pm 1.32)$  pb.
- **single top cross section**: There are two single top production modes, the  $s$ -channel and the  $t$ -channel, as discussed in section 1.3.1. The theoretical cross section at  $\sqrt{s} = 1.96$  TeV is  $0.88 \pm 0.11$  pb for  $s$ -channel and  $1.98 \pm 0.25$  pb for  $t$ -channel, respectively [62] (errors on  $\sigma_{s-ch.}$  taken from [58], while errors on  $\sigma_{t-ch.}$  taken from [59]). The uncertainty due to the error in the top quark mass ( $\Delta m = \pm 5$  GeV) is about 10% [43]. The PDF uncertainty is typically 5%. In total we assume an error of 13% on both cross sections. We note that the combined single top cross section of about

Cut	0 jet	1 jet	2 jet	3 jet	4 jet	$\geq 5$ jets	all
Total	70262	321992	188209	89598	21286	4586	695933
OBSV $< 60.0$	68263	313447	180270	86246	20523	4420	673169
$\geq 1$ Tight Std. lepton	27474	126198	31536	5738	859	125	191930
$\geq 1$ with add. ID cuts	19501	91058	22805	4154	597	86	138201
CEM electrons							
Tight Di-Lepton Veto	10770	50347	12480	2264	328	46	76235
PHX Veto	10762	50343	12478	2264	328	46	76221
Z Vertex Cut	10760	50338	12476	2264	328	46	76212
Conversion veto	10732	50190	12437	2252	327	46	75984
Z veto	10658	49935	12319	2204	324	45	75485
Missing Et	9964	43924	10814	1919	294	41	66956
b tag $\geq 1$	0	14900	3831	687	111	17	19546
b-tag=1 or 2	0	14900	3831	686	111	17	19545
$140 \leq M_{b\ell\nu} \leq 210$	0	12552	2951	506	79	13	16101
$E_T(\text{Jet1}) \geq 30$ GeV	0	11719	2735	482	77	13	15026
CMUP muons							
Tight Di-Lepton Veto	5776	27688	7017	1322	177	25	42005
PHX Veto	5773	27684	7017	1322	177	25	41998
Z Vertex Cut	5773	27684	7017	1322	177	25	41998
Z veto	5752	27602	6989	1312	176	25	41856
Missing Et	5333	23977	6065	1142	158	21	36696
b tag $\geq 1$	0	8006	2125	414	65	9	10619
b-tag=1 or 2	0	8006	2125	414	65	9	10619
$140 \leq M_{b\ell\nu} \leq 210$	0	6562	1599	291	42	6	8500
$E_T(\text{Jet1}) \geq 30$ GeV	0	6195	1480	272	38	6	7991
CMX muons							
Tight Di-Lepton Veto	2939	13012	3305	568	92	15	19931
PHX Veto	2939	13012	3305	568	92	15	19931
Z Vertex Cut	2939	13012	3305	568	92	15	19931
Z veto	2931	12994	3288	566	91	15	19885
Missing Et	2733	11310	2878	497	80	12	17510
b tag $\geq 1$	0	3813	1011	172	16	3	5015
b-tag=1 or 2	0	3813	1011	170	16	3	5013
$140 \leq M_{b\ell\nu} \leq 210$	0	3257	758	122	5	2	4144
$E_T(\text{Jet1}) \geq 30$ GeV	0	3023	703	113	5	2	3846
All							
Tight Di-Lepton Veto	19485	91047	22802	4154	597	86	138171
PHX Veto	19474	91039	22800	4154	597	86	138150
Z Vertex Cut	19472	91034	22798	4154	597	86	138141
Conversion veto	19444	90886	22759	4142	596	86	137913
Z veto	19341	90531	22596	4082	591	85	137226
Missing Et	18030	79211	19757	3558	532	74	121162
b tag $\geq 1$	0	26719	6967	1273	192	29	35180
b-tag=1 or 2	0	26719	6967	1270	192	29	35177

Table 4.3: Cut flow table of baseline event selection for anomalous top (utopg0) events.

2.9 pb is roughly the half of the  $t\bar{t}$  cross section [40, 38, 39, 41].

CEM electrons							
Cut	0 jet	1 jet	2 jet	3 jet	4 jet	$\geq 5$ jets	All
b tag = 1	0	12552	2935	500	77	13	16077
Jet 1 $E_t \geq 30$ GeV	0	11719	2719	477	75	13	15003
b tag = 2	0	0	16	6	2	0	24
CMUP muons							
Cut	0 jet	1 jet	2 jet	3 jet	4 jet	$\geq 5$ jets	All
b tag = 1	0	6562	1586	286	39	6	8479
Jet 1 $E_t \geq 30$ GeV	0	6195	1467	267	35	6	7970
b tag = 2	0	0	13	5	3	0	21
CMX muons							
Cut	0 jet	1 jet	2 jet	3 jet	4 jet	$\geq 5$ jets	All
b tag = 1	0	3257	747	120	5	2	4131
Jet 1 $E_t \geq 30$ GeV	0	3023	692	111	5	2	3833
b tag = 2	0	0	11	2	0	0	13
All							
Cut	0 jet	1 jet	2 jet	3 jet	4 jet	$\geq 5$ jets	All
b tag = 1	0	22371	5268	906	121	21	28687
Jet 1 $E_t \geq 30$ GeV	0	20937	4878	855	115	21	26806
b tag = 2	0	0	40	13	5	0	58

Table 4.4: Cut flow table of anomalous top search. We show the cut flow for the additional cuts applied after the  $M_{\ell\nu b}$  cut. The lines with 'b tag = 1' give the number of events in the 1-b-tag-bin. The lines with 'Jet 1  $E_t \geq 30$  GeV' give the number of the events in the 1-b-tag bin after the extra cut on the leading jet  $E_T$ . The lines named 'b tag = 2' give the number of events in the double-tag-bin.

#### 4.1.3.2 Di-Boson Background

To predict the number of di-boson events ( $WW, WZ, ZZ$ ) in our selected data sample we use the theoretical cross sections predicted by Campbell and Ellis [44]:

Campbell and Ellis give a relative error on the cross sections of 3%. Their numbers are given for  $\sqrt{s} = 2.00$  TeV. We rescale those numbers to 1.96 TeV. We take the mean of a linear and a quadratic interpolation. We will calculate the number of expected di-boson events in the same way as for single top and  $t\bar{t}$ .

#### 4.1.3.3 Further Non-Top Background

While the SM top background and the di-boson background can be estimated using the theoretical cross section predictions and acceptance from Monte Carlo, this method does not work for  $W$  plus multi-jet backgrounds because those cross sections are not reliably predicted by theory. Five different classes of events contribute to our non-top background (other than di-boson) events:

Cut	CEM	CMUP	CMX	All	$N_i/N_{i-1}$
OBSV < 60.0				673169	–
1 Tight Std. lepton	0	0	0	191930	28.51%
Add ID cuts	0	0	0	138201	72.01%
Di-Lepton Veto	76235	42005	19931	138171	99.98%
Conversion veto	75984	41998	19931	137913	99.81%
Z veto	75485	41856	19885	137226	99.5%
Raw miss. Et (Info)	66990	36729	17491	121210	88.33%
Missing Et	66956	36696	17510	121162	88.29%
$M_W$ real (Info)	47784	28940	13441	90165	74.42%
b tag $\geq 1$	19546	10619	5015	35180	29.04%
miss tag (Info)	425	193	105	723	0.5967%
b tag = 1 (Info)	19497	10588	4994	35079	28.95%
b tag = 2 (Info)	48	31	19	98	0.08088%
b-tag=1 or 2	19545	10619	5013	35177	99.99%
b-Tag Scale Factor	16023	8710	4147	28880	82.09%
b tag Scale = 1 (Info)	15990	8686	4131	28807	82.12%
b tag Scale = 2 (Info)	33	24	16	73	74.49%
b tag Scale = 1, 2 (Info)	16023	8710	4147	28880	82.1%
$140 \leq M_{b\ell\nu} \leq 210$	16101	8500	4144	28745	81.72%
$E_T(\text{Jet } 1) \geq 30 \text{ GeV}$	15026	7991	3846	26863	93.45%

Table 4.5: Cut flow table of anomalous top events selection summed over all jet bins.

$\sqrt{s}$	WW	WZ	ZZ
2.00 TeV	13.5 pb	4.02 pb	1.60 pb
1.96 TeV	13.30 pb	3.96 pb	1.57 pb

Table 4.6: Cross section predictions used in our analysis to predict the number of di-boson background events.

- $Wb\bar{b}$
  - $Wc\bar{c}$
  - $Wc$
- $$\left. \begin{array}{l} \bullet Wb\bar{b} \\ \bullet Wc\bar{c} \\ \bullet Wc \end{array} \right\} W + \text{heavy flavor}$$
- *mistags*
  - *non* –  $W$

$W$ +heavy flavor refers to processes like  $\bar{q}_1 q_2 \rightarrow Wg$  with  $q \rightarrow b\bar{b}$  or  $q \rightarrow c\bar{c}$  and  $gq \rightarrow Wc$ . Mis-tags are processes in which a light-quark jet is erroneously identified as heavy flavor, while non- $W$  refers to direct  $b\bar{b}$  production. For the lepton+jets  $t\bar{t}$  cross section measurement a background estimate was performed which is partly based on CDF data and partly on Monte Carlo simulations (known as method 2) [45]. We base our background numbers on this estimate. To take into account differences between the  $t\bar{t}$  cross section analysis and our analysis we re-scale the numbers by cut-efficiencies obtained from Monte Carlo events ( $Wb\bar{b}$ ,  $Wc\bar{c}$ ,  $Wc$ , mis-tags) or data (non- $W$ ).

### 4.1.4 Event Detection Efficiency

The aim of our analysis is to set an upper limit on the anomalous top quark cross section  $\sigma_{ano}$ , which will be used in a future analysis for the deduction of an upper limit on  $\frac{\kappa_u}{\Lambda}$ . The calculation of  $\sigma_{ano}$  is based on the following formula:

$$\sigma_{ano} = \frac{N_{\text{signal}}}{\epsilon_{\text{evt}} \cdot \int \mathcal{L} dt} \quad (4.5)$$

Here  $N_{\text{signal}}$  is the number of observed signal events, which we obtain for example from a maximum likelihood fit.  $\epsilon_{\text{evt}}$  is the event detection efficiency which is the average probability of an anomalous top event to be detected, i.e. to be found in our selected candidate sample.  $\int \mathcal{L} dt$  is the integrated luminosity, which we will abbreviate as  $\mathcal{L}_{\text{int}}$  in the paragraphs below. In this analysis,  $\mathcal{L}_{\text{int}}$  corresponds to  $162 \text{ pb}^{-1}$ .

Since we are not able to measure  $\sigma_{ano}$  at the Tevatron, we will set an upper limit on the cross section, pretending to have a theoretical prediction for the cross section of the anomalous top production. For this (4.5) is not directly used. Instead, we will use (4.5) to calculate the number of expected signal events. For this purpose it takes the form:

$$N_{\text{signal}}^{\text{predict}} = \sigma_{ano}^{\text{theo}} \cdot \epsilon_{\text{evt}} \cdot \mathcal{L}_{\text{int}} \quad (4.6)$$

The purpose of this chapter is to document the calculation of  $\epsilon_{\text{evt}}$ , the event detection efficiency. This is done using the Monte Carlo samples listed in Table 4.1 in section 4.1.1.  $\epsilon_{\text{evt}}$  can be decomposed into 4 factors:

$$\epsilon_{\text{evt}} = \epsilon_{\text{evt}}^{\text{MC}} \cdot \epsilon_{\text{BR}} \cdot \epsilon_{\text{corr}} \cdot \epsilon_{\text{trig}} \quad (4.7)$$

Here  $\epsilon_{\text{trig}}^{\text{MC}}$  is the event detection efficiency as we obtain it from our samples of simulated events. In some of these samples the  $W$  boson was only allowed to decay into leptons:  $W \rightarrow e/\mu/\tau + \nu$ . This has to be taken into account by applying the factor  $\epsilon_{\text{BR}} = 0.3204$  [51].  $\epsilon_{\text{corr}}$  is a correction factor which takes into account the difference between simulated and data events.  $\epsilon_{\text{corr}}$  gives a measure how well the Monte Carlo simulation models the detector.  $\epsilon_{\text{trig}}$  is the trigger efficiency. The correction factor is again composed out of several parts:

$$\epsilon_{\text{corr}} = \frac{\epsilon_{z0}^{\text{data}}}{\epsilon_{z0}^{\text{MC}}} \cdot \frac{\epsilon_{\text{leptonid}}^{\text{data}}}{\epsilon_{\text{leptonid}}^{\text{MC}}} \cdot \frac{\epsilon_{\text{reco}}^{\text{data}}}{\epsilon_{\text{reco}}^{\text{MC}}} \cdot \frac{\epsilon_{\text{tag}}^{\text{data}}}{\epsilon_{\text{tag}}^{\text{MC}}} \quad (4.8)$$

Since trigger and id efficiencies vary for different subdetectors (we use CEM, CMU/CMP and CMX, see section 3), we have different  $\epsilon_{\text{evt}}$  in the three cases:  $\epsilon_{\text{evt}}^{\text{CEM}}$ ,  $\epsilon_{\text{evt}}^{\text{CMUP}}$  and  $\epsilon_{\text{evt}}^{\text{CMX}}$ . The determination of  $\epsilon_{\text{evt}}^{\text{MC}}$  from Monte Carlo simulations will be discussed in section 4.1.4.1. We use the following values for the trigger efficiencies and the reconstruction and identification scale factors which are derived from data [52, 53, 54]:

- $\epsilon_{z0}^{\text{data}} = 0.951 \pm 0.001 \pm 0.005$  is the  $z$  vertex cut efficiency in data [55]. In Monte Carlo we obtain  $\epsilon_{z0}^{\text{MC}} = 0.965 \pm 0.003$  (stat.) for the MadEvent samples and  $\epsilon_{z0}^{\text{MC}} = 0.967 \pm 0.003$  (stat.) for the PYTHIA samples. The correction factors therefore are:  $\frac{\epsilon_{z0}^{\text{data}}}{\epsilon_{z0}^{\text{MC}}} = 0.986 \pm 0.006$  and  $\frac{\epsilon_{z0}^{\text{data}}}{\epsilon_{z0}^{\text{MC}}} = 0.983 \pm 0.006$  respectively.

- The b-tagging efficiency differs between data and Monte Carlo. Therefore, we need to correct our acceptance calculation which is based on Monte Carlo events.  $\frac{\epsilon_{\text{tag-jet}}^{\text{data}}}{\epsilon_{\text{tag-jet}}^{\text{MC}}} = 0.82 \pm 0.06$  is the correction factor for b-tagging efficiency [56]. This correction factor is valid per tagged b-jet. If a Monte Carlo sample contained only events with one and only b-jet per event, the factor would be applicable globally. However, since there are also double-tag events the global correction factor has to be determined. One method is the counting method as described in Ref. [57]. We applied this method to our Monte Carlo samples. Each b-tagged jet is considered individually. Randomly we discard  $1 - \frac{\epsilon_{\text{tag}}^{\text{data}}}{\epsilon_{\text{tag}}^{\text{MC}}} = 18\%$  of the jets and count the remaining events with at least one b-jet. The results on the global correction factor  $K = \frac{\epsilon_{\text{tag,global}}^{\text{data}}}{\epsilon_{\text{tag,global}}^{\text{MC}}}$  are given in Table 4.7 for the case that exactly 1 b-tag ( $K_1$ ) is required.

Process	t-channel	s-channel	$t\bar{t}$	Process	anoTop
Sample	mtop0s/1s	mtop2s	ttopei	Sample	utopg0
$K_1$	$0.8304 \pm 0.06$	$0.8910 \pm 0.06$	$0.9155 \pm 0.06$	$K_1$	$0.8212 \pm 0.06$

Process	WW	WZ	ZZ
Sample	atop4x	atop0y	atop0z
$K_1$	$0.8242 \pm 0.06$	$0.8551 \pm 0.06$	$0.7714 \pm 0.06$

Table 4.7: Correction factor for b-tagging efficiency of the various samples.

#### 4.1.4.1 Determination of $\epsilon_{\text{evt}}^{\text{MC}}$

We determine the event detection efficiency based on Monte Carlo events. We apply all selection and identification cuts to our simulated data. Table 4.8 summarizes the number of remaining events in the 1-Jet bin, after b-tagging ( $N_{\text{btag}}$ ), after the additional cut on the first jet  $E_T$  ( $N_{\text{Jet}E_T}$ ) and after the  $M_{\ell\nu b}$  cut ( $N_{M_{\ell\nu b}}$ ).

#### 4.1.4.2 Determination of $\epsilon_{\text{evt}}$

To determine  $\epsilon_{\text{evt}}$  we need to know  $\epsilon_{\text{BR}}$  for each sample as well as  $\epsilon_{\text{trig}}$  and  $\epsilon_{\text{corr}}$ .  $\epsilon_{\text{BR}}$  is given in Table 4.9 and  $\epsilon_{\text{trig}}$  is given in Table 4.10. We first build  $\epsilon_{\text{evt}}^{\text{MC}} \cdot \epsilon_{\text{BR}}$  and present the results in Table 4.11.

For the calculation of  $\epsilon_{\text{corr}}$  we use the values given in Table 4.10 and follow (4.8) in section 4.1.4. We have to do the calculation for each sample separately, since the b-tagging efficiency per event depends on the sample. We calculate the errors on  $\epsilon_{\text{corr}}$  by adding the relative errors on  $\frac{\epsilon_{z0}^{\text{data}}}{\epsilon_{z0}^{\text{MC}}}$ ,  $\frac{\epsilon_{\text{leptonid}}^{\text{data}}}{\epsilon_{\text{leptonid}}^{\text{MC}}}$ ,  $\frac{\epsilon_{\text{reco}}^{\text{data}}}{\epsilon_{\text{reco}}^{\text{MC}}}$  and  $\frac{\epsilon_{\text{tag}}^{\text{data}}}{\epsilon_{\text{tag}}^{\text{MC}}}$ . We present the results on  $\epsilon_{\text{corr}}$  including the errors in Table 4.12.

Having calculated  $\epsilon_{\text{corr}}$  we can now compute  $\epsilon_{\text{evt}}$  based on (4.7). The result is presented in Table 4.13. Using the values for  $\epsilon_{\text{evt}}$  we calculate the number of expected events according to (4.6). For this calculation we need the cross section predictions, which were already mentioned in sections 4.1.3.1 and 4.1.3.2 and are listed in Table 4.19. To provide a

Process	anoTop	t-ch.	s-ch.	$t\bar{t}$	WW	WZ	ZZ
$N_{tot}$	2500000	163237	199953	398037	944969	191011	223606
$N_{obsv}$	2418225	157832	192931	384875	913775	184934	216547
CEM Electrons							
$N_{btag}$	14900	2854	2442	332	623	123	14
$N_{JetEt}$	12837	2444	2056	294	396	96	11
$N_{M\ell\nu b}$	12537	2383	1713	141	313	80	7
CMUP Muons							
$N_{btag}$	8006	1532	1322	164	348	64	28
$N_{JetEt}$	6992	1323	1128	147	248	48	16
$N_{M\ell\nu b}$	6712	1288	910	85	196	37	13
CMX Muons							
$N_{btag}$	3813	617	555	68	178	35	12
$N_{JetEt}$	3246	512	457	55	111	24	7
$N_{M\ell\nu b}$	3207	503	393	34	95	19	7
ALL							
$N_{btag}$	26719	5003	4319	564	1149	222	54
$N_{JetEt}$	23075	4279	3641	496	755	168	34
$N_{M\ell\nu b}$	22456	4174	3016	260	604	136	27

Table 4.8: Number of Monte Carlo events after event selection in the 1-jet bin.

Process	anoTop	t-channel	s-channel	$t\bar{t}$	WW	WZ	ZZ
$\epsilon_{BR}$	0.9876	0.3204	0.3204	0.9876	0.3204	0.9876	1.0

Table 4.9: Branching ratio efficiency of the various samples.

$\epsilon^{\text{data}}/\epsilon^{\text{MC}}$	CEM	CMUP	CMX
Trigger	0.9656 $\pm$ 0.0006	0.887 $\pm$ 0.007	0.954 $\pm$ 0.006
ID s.f.	0.965 $\pm$ 0.006	0.939 $\pm$ 0.007	1.014 $\pm$ 0.007
Reco s.f.	1.0 per def.	0.945 $\pm$ 0.006	0.992 $\pm$ 0.003
z0 PYTHIA,Alpgen	0.983 $\pm$ 0.006	0.983 $\pm$ 0.006	0.983 $\pm$ 0.006
z0 MadEvent	0.986 $\pm$ 0.006	0.986 $\pm$ 0.006	0.986 $\pm$ 0.006

Table 4.10: Electron and muon trigger efficiencies, ID efficiency scale (correction) factors and z vertex cut efficiency.

reference point for the anomalous top quark production channel we assume a cross section of 1.0 pb since there is no theoretical prediction, so the number of the expected anomalous top events are based on this assumption. The results are shown in Table 4.14.

#### 4.1.4.3 Non-Top Background Estimate

For the non-top background estimate (other than di-boson) we use the same cuts as in section 4.1.4.1 and obtain a certain number of events. The number of these cut scenarios



**Monte Carlo Event Detection Efficiency in %**

Process	anoTop	t-ch.	s-ch.	$t\bar{t}$	WW	WZ	ZZ
CEM Electrons							
$\epsilon_{btag}$	0.588	0.560	0.391	0.082	0.021	0.064	0.006
$\epsilon_{JetEt}$	0.507	0.480	0.329	0.073	0.013	0.050	0.005
$\epsilon_{M\ell\nu b}$	0.495	0.468	0.274	0.035	0.011	0.041	0.003
CMUP Muons							
$\epsilon_{btag}$	0.316	0.301	0.212	0.041	0.012	0.033	0.012
$\epsilon_{JetEt}$	0.276	0.260	0.181	0.036	0.008	0.025	0.007
$\epsilon_{M\ell\nu b}$	0.265	0.253	0.146	0.021	0.007	0.019	0.006
CMX Muons							
$\epsilon_{btag}$	0.150	0.121	0.089	0.017	0.006	0.018	0.005
$\epsilon_{JetEt}$	0.128	0.100	0.073	0.014	0.004	0.012	0.003
$\epsilon_{M\ell\nu b}$	0.126	0.099	0.063	0.008	0.003	0.010	0.003
ALL							
$\epsilon_{btag}$	1.055	0.982	0.692	0.140	0.039	0.115	0.024
$\epsilon_{JetEt}$	0.911	0.840	0.583	0.123	0.026	0.087	0.015
$\epsilon_{M\ell\nu b}$	0.887	0.820	0.483	0.065	0.020	0.070	0.012

Table 4.11:  $\epsilon_{\text{evt}}^{\text{MC}} \cdot \epsilon_{\text{BR}}$  for background and signal samples. The statistical error on the efficiencies is 0.01% or less.

Process	anoTop	t-channel	s-channel	$t\bar{t}$
CEM Electrons				
btag = 1	0.779±0.057	0.788±0.057	0.847±0.057	0.869±0.057
CMUP Muons				
btag = 1	0.716±0.052	0.725±0.053	0.779±0.053	0.799±0.053
CMX Muons				
btag = 1	0.812±0.059	0.822±0.060	0.883±0.060	0.906±0.059
Process	WW	WZ	ZZ	
CEM Electrons				
btag = 1	0.782±0.057	0.811±0.057	0.731±0.057	
CMUP Muons				
btag = 1	0.719±0.053	0.745±0.053	0.672±0.053	
CMX Muons				
btag = 1	0.815±0.059	0.845±0.059	0.762±0.059	

Table 4.12:  $\epsilon_{\text{corr}}$  for single top,  $t\bar{t}$  and di-boson events

are given in Table 4.15. Based on these numbers we calculate scale factors for the different scenarios which are shown in Table 4.16. We evaluate errors due to a change in jet energy scale on these scale factors. Those numbers are given in Table 4.17. The background estimate for the  $t\bar{t}$  analysis is presented in Table 4.18. The resulting number of non-top events predicted for the anomalous top analysis are given in Table 4.20.



## Event Detection Efficiency in %

Process	anoTop	t-channel	s-channel	$t\bar{t}$
CEM Electrons				
$\epsilon_{btag}$	$0.442 \pm 0.032$	$0.426 \pm 0.031$	$0.320 \pm 0.021$	$0.069 \pm 0.004$
$\epsilon_{JetEt}$	$0.381 \pm 0.028$	$0.365 \pm 0.026$	$0.269 \pm 0.018$	$0.061 \pm 0.004$
$\epsilon_{M\ell\nu b}$	$0.372 \pm 0.027$	$0.356 \pm 0.025$	$0.224 \pm 0.015$	$0.029 \pm 0.001$
CMUP Muons				
$\epsilon_{btag}$	$0.200 \pm 0.014$	$0.193 \pm 0.014$	$0.146 \pm 0.010$	$0.029 \pm 0.001$
$\epsilon_{JetEt}$	$0.175 \pm 0.013$	$0.167 \pm 0.012$	$0.125 \pm 0.008$	$0.026 \pm 0.001$
$\epsilon_{M\ell\nu b}$	$0.168 \pm 0.012$	$0.163 \pm 0.011$	$0.101 \pm 0.006$	$0.015 \pm 0.001$
CMX Muons				
$\epsilon_{btag}$	$0.116 \pm 0.008$	$0.095 \pm 0.006$	$0.075 \pm 0.005$	$0.015 \pm 0.0009$
$\epsilon_{JetEt}$	$0.099 \pm 0.007$	$0.079 \pm 0.005$	$0.062 \pm 0.004$	$0.012 \pm 0.0007$
$\epsilon_{M\ell\nu b}$	$0.098 \pm 0.007$	$0.077 \pm 0.005$	$0.053 \pm 0.003$	$0.007 \pm 0.0004$
ALL				
$\epsilon_{btag}$	$0.760 \pm 0.036$	$0.715 \pm 0.034$	$0.541 \pm 0.024$	$0.113 \pm 0.005$
$\epsilon_{JetEt}$	$0.656 \pm 0.031$	$0.611 \pm 0.029$	$0.456 \pm 0.020$	$0.099 \pm 0.004$
$\epsilon_{M\ell\nu b}$	$0.639 \pm 0.031$	$0.596 \pm 0.029$	$0.378 \pm 0.017$	$0.052 \pm 0.002$
Process	WW	WZ	ZZ	
CEM Electrons				
$\epsilon_{btag}$	$0.016 \pm 0.001$	$0.050 \pm 0.003$	$0.004 \pm 0.0003$	
$\epsilon_{JetEt}$	$0.010 \pm 0.0007$	$0.039 \pm 0.002$	$0.003 \pm 0.0002$	
$\epsilon_{M\ell\nu b}$	$0.008 \pm 0.0005$	$0.032 \pm 0.002$	$0.002 \pm 0.0001$	
CMUP Muons				
$\epsilon_{btag}$	$0.008 \pm 0.0005$	$0.022 \pm 0.001$	$0.007 \pm 0.0005$	
$\epsilon_{JetEt}$	$0.005 \pm 0.0003$	$0.016 \pm 0.001$	$0.004 \pm 0.0003$	
$\epsilon_{M\ell\nu b}$	$0.004 \pm 0.0003$	$0.013 \pm 0.0009$	$0.003 \pm 0.0002$	
CMX Muons				
$\epsilon_{btag}$	$0.005 \pm 0.0003$	$0.015 \pm 0.001$	$0.004 \pm 0.0003$	
$\epsilon_{JetEt}$	$0.003 \pm 0.0002$	$0.010 \pm 0.0007$	$0.002 \pm 0.0001$	
$\epsilon_{M\ell\nu b}$	$0.003 \pm 0.0001$	$0.008 \pm 0.0005$	$0.002 \pm 0.0001$	
ALL				
$\epsilon_{btag}$	$0.028 \pm 0.001$	$0.086 \pm 0.003$	$0.016 \pm 0.0007$	
$\epsilon_{JetEt}$	$0.018 \pm 0.0008$	$0.065 \pm 0.003$	$0.010 \pm 0.0004$	
$\epsilon_{M\ell\nu b}$	$0.015 \pm 0.0006$	$0.053 \pm 0.002$	$0.008 \pm 0.0003$	

Table 4.13:  $\epsilon_{BR} \cdot \epsilon_{evt}^{MC} \cdot \epsilon_{corr} \cdot \epsilon_{trig}$

Process	anoTop	t-channel	s-channel	$t\bar{t}$
$N_{btag}$	$1.231\pm 0.059$	$2.292\pm 0.319$	$0.775\pm 0.106$	$1.221\pm 0.246$
$N_{JetEt}$	$1.063\pm 0.051$	$1.959\pm 0.272$	$0.653\pm 0.089$	$1.073\pm 0.216$
$N_{M\ell\nu b}$	$1.035\pm 0.050$	$1.911\pm 0.266$	$0.541\pm 0.074$	$0.560\pm 0.112$
Process	WW	WZ	ZZ	di-boson
$N_{btag}$	$0.607\pm 0.034$	$0.553\pm 0.030$	$0.040\pm 0.002$	$1.200\pm 0.050$
$N_{JetEt}$	$0.397\pm 0.022$	$0.419\pm 0.023$	$0.025\pm 0.001$	$0.841\pm 0.034$
$N_{M\ell\nu b}$	$0.318\pm 0.017$	$0.340\pm 0.019$	$0.020\pm 0.001$	$0.678\pm 0.025$

Table 4.14: Number of expected events for single top,  $t\bar{t}$  and di-boson Monte Carlo samples.

Process	$Wbb$	$Wc\bar{c}$	$Wc$	Mis-tags	non-W
$N_{btag}$	9511	2229	1803	23840	513
$N_{JetEt}$	4439	1003	753	8850	271
$N_{M\ell\nu b}$	3693	827	691	8013	256

Table 4.15: Number of Monte Carlo events after event selection in the 1-jet bin.

Process	$Wbb$	$Wc\bar{c}$	$Wc$	Mis-tags	non-W
$\epsilon_{btag}$	1	1	1	1	1
$\epsilon_{JetEt}$	0.467	0.45	0.418	0.371	0.528
$\epsilon_{M\ell\nu b}$	0.388	0.371	0.383	0.336	0.499

Table 4.16: Scale factor for 1-jet bin.

Process	$Wbb$	$Wc\bar{c}$	$Wc$	Mis-tags	non-W
$N_{JetEt}$	13%	12%	13%	18%	16%
$N_{M\ell\nu b}$	11%	11%	11%	16%	15%

Table 4.17: Relative errors on scale factors for different cut scenarios.

Process	$Wbb$	$Wc\bar{c}$	$Wc$	Mis-tags	non-W
$N$	$37.0\pm 11.2$	$13.7\pm 3.4$	$34.5\pm 9.0$	$40.9\pm 6.1$	$22.9\pm 3.3$

Table 4.18: Predicted number of background events for  $t\bar{t}$  cross section analysis.

Process	anoTop	t-channel	s-channel	$t\bar{t}$
$\sigma^{\text{theo}}[\text{pb}]$	$1.0 \pm 0.0$	$1.98 \pm 0.25$	$0.88 \pm 0.11$	$6.70 \pm 1.32$
Process	WW	WZ	ZZ	
$\sigma^{\text{theo}}[\text{pb}]$	$13.300 \pm 0.39$	$3.960 \pm 0.12$	$1.570 \pm 0.05$	

Table 4.19: Cross section predictions used in our analysis to predict the number of background events.

Process	$Wbb$	$Wc\bar{c}$	$Wc$	W+HF
$N_{btag}$	$37.0 \pm 11.2$	$13.7 \pm 3.4$	$34.5 \pm 9.0$	$85.2 \pm 14.77$
$N_{JetEt}$	$17.27 \pm 5.69$	$6.165 \pm 1.69$	$14.41 \pm 4.2$	$37.845 \pm 7.27$
$N_{M\ell\nu b}$	$14.37 \pm 4.63$	$5.083 \pm 1.38$	$13.22 \pm 3.74$	$32.673 \pm 6.11$
Process	Mis-tags	non-W	$\Sigma$	
$N_{btag}$	$40.9 \pm 6.1$	$22.9 \pm 3.3$	$149.0 \pm 16.32$	
$N_{JetEt}$	$15.19 \pm 3.55$	$12.1 \pm 2.61$	$65.135 \pm 8.50$	
$N_{M\ell\nu b}$	$13.75 \pm 3.01$	$11.43 \pm 2.38$	$57.853 \pm 7.21$	

Table 4.20: Number of expected non-top events in anomalous top analysis. W+HF stands for the sum over all W+heavy flavor events.  $\Sigma$  stands for the sum over all non-top background processes (other than di-boson).

#### 4.1.4.4 Number of Expected Events

We now are able to compare the number of expected events of the anomalous top quark production (for the assumption of  $\sigma_{ano}^{\text{theo}} = 1.0$  pb) to those of the various background channels. We chose four major categories in which we arranged the background channels. The first is the standard model top production, in which we added the events of the single top and the  $t\bar{t}$  production. The second consists of the sum over the W+heavy flavor channels added to the sum over the di-boson events. The third category are the non-W events and in the last category we put the mis-tags. The total background sums up to  $61.334 \pm 7.22$  expected events in the 1-jet bin, whereas for the anomalous top production  $1.035 \pm 0.050$  events are expected. The analytical results for each of the categories mentioned above are to be found in Table 4.21.

#### 4.1.4.5 Top Mass Templates

Figure 4.1 shows the stacked histograms of each process summed up to a category, see section 4.1.4.4, after cutting on the reconstructed top-mass. In order to add the sum of the di-boson histograms to those of the W+heavy flavor processes (Figure 4.1, bottom right), we extracted the shape of the WW channel and used it as the shape for all the di-boson processes, since the error would be negligible. One can see how good the approximation is on Figure 4.1 (bottom left), where the shape of each di-boson process is shown. Figure 4.2 presents the added histograms of each background category (section 4.1.4.4) compared to the expected signal (anomalous top production process).

Process	N events
SM top production	$3.012 \pm 0.29$
W+HF + di-boson	$33.142 \pm 6.11$
non-W QCD	$11.43 \pm 2.38$
Mistags	$13.75 \pm 3.01$
Total Background	$61.334 \pm 7.22$
anomalous top	$1.035 \pm 0.050$

Table 4.21: Number of background and signal events in the 1-jet bin. SM top production stands for the standard model predicted  $t\bar{t}$  pair and the two single top production channels. W+HF stands for 'W+heavy flavor', di-boson stands for WW, WZ, ZZ.

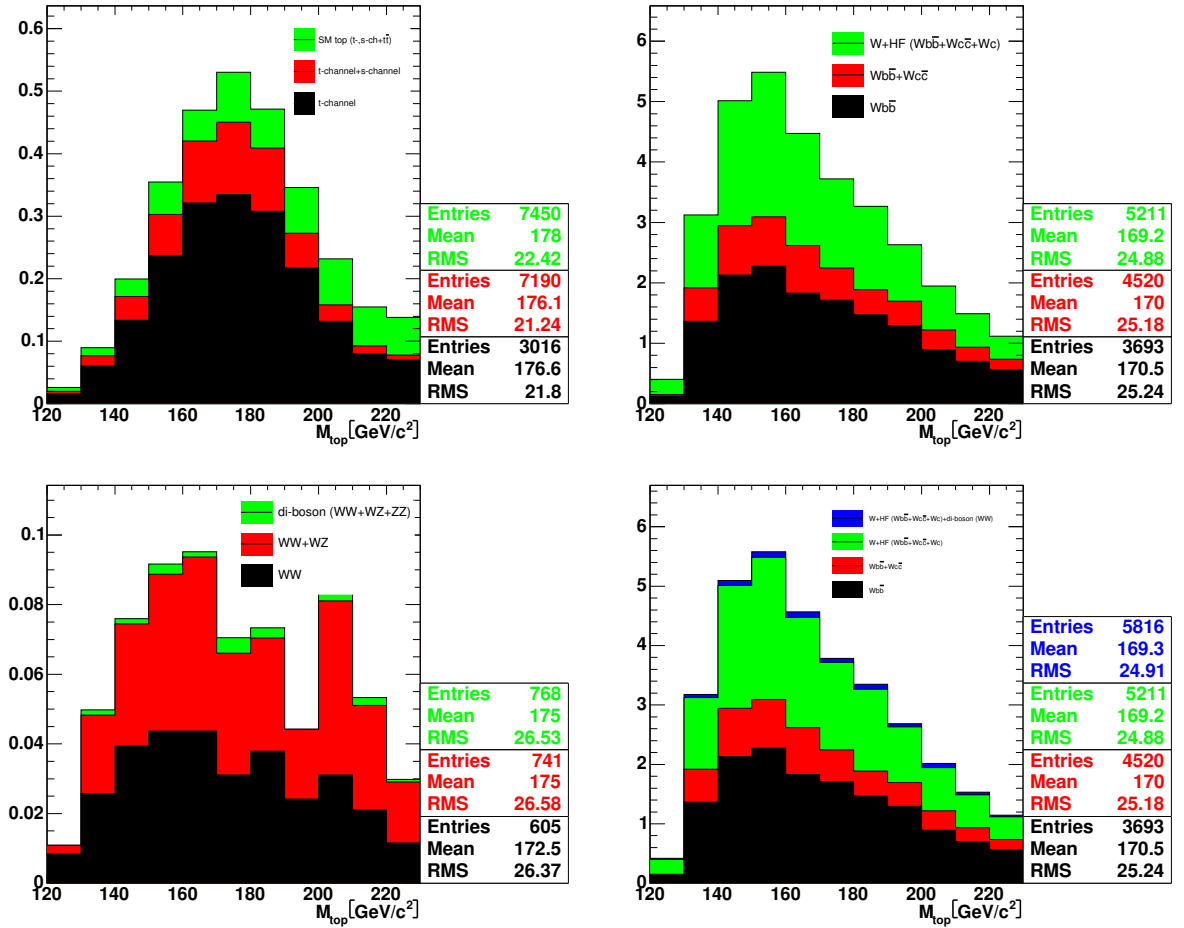


Figure 4.1: Top-mass templates of the SM top production (top left), the W+heavy flavor channels (top right), the di-boson channels (bottom left) and the sum over the W+heavy flavor channels added to the di-boson channels (bottom right).

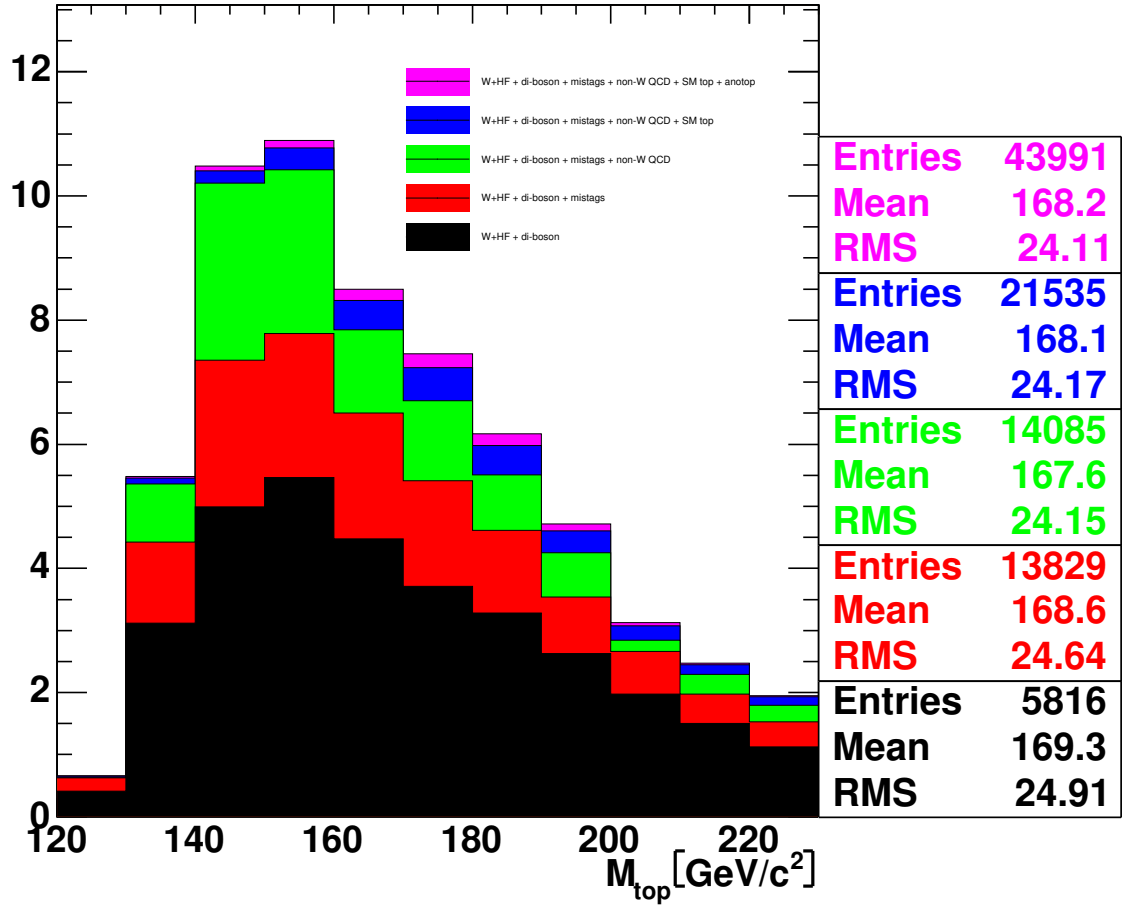


Figure 4.2: Top-mass templates of all the involved background channels compared to the anomalous top production.

## 4.2 Likelihood Fit

In order to extract the signal content we use a maximum likelihood technique, following [60, 61]. For this method we need to find a suitable variable where expected signal and background events are easy to distinguish. At parton level study, see chapter 2, the most prominent difference in kinematics occurred in the variable  $Q \cdot \eta$  of the top quark, shown in Figure 2.6. According to the pure Monte Carlo study at parton level, this distribution was initially thought to be helpful for the fitting part of our analysis, but after plotting  $Q \cdot \eta$  in the detector simulation, it turned out to be unsuitable for our purposes. This can be seen in Figure 4.3, where  $[Q \cdot \eta]^{MC}$  is shown compared to the detector simulation of this variable  $[Q \cdot \eta]^{rec}$ .

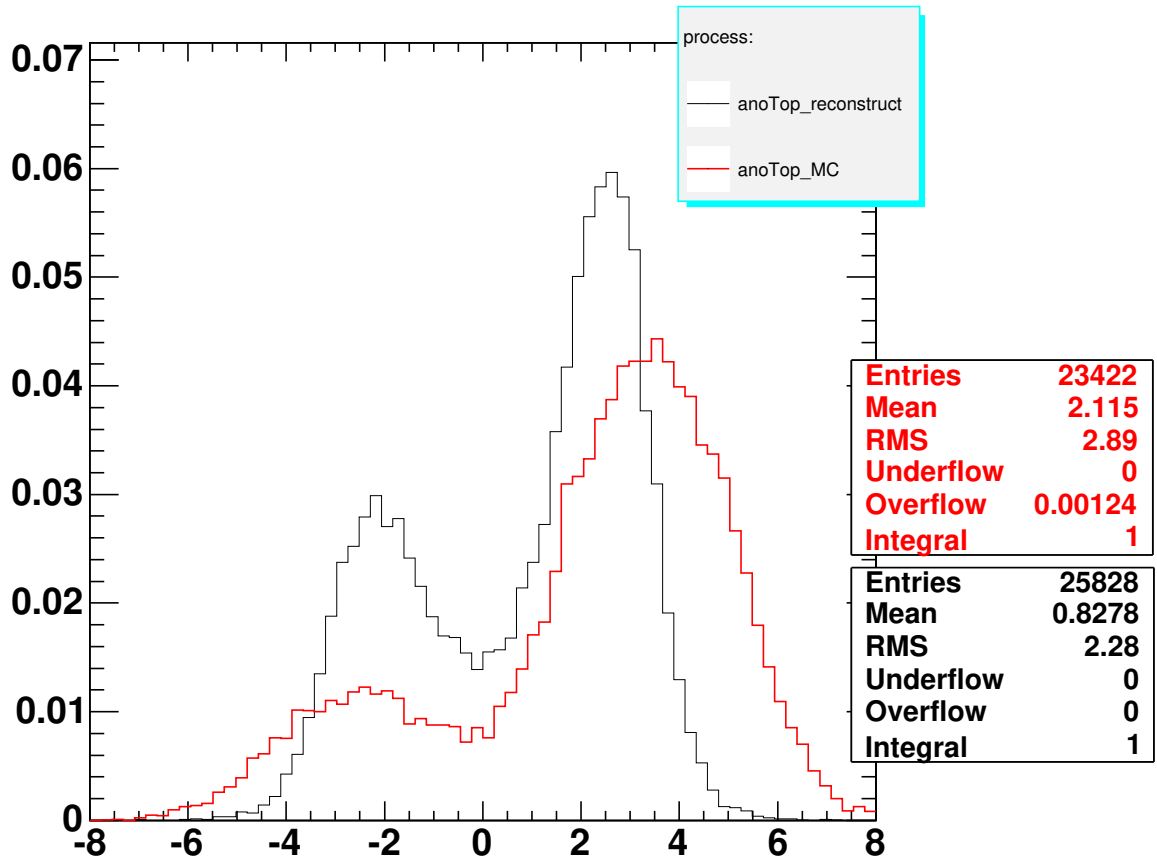


Figure 4.3:  $Q \cdot \eta$  of the top quark gained from pure MC study compared to the same variable as seen in the detector simulation.

We went on testing further variables like those shown and explained in Appendix A and ended up with the decision that the signal was easier to distinguish when choosing the reconstructed mass of the top quark in the region of  $120 \text{ GeV} < M_{\ell\nu b} < 230 \text{ GeV}$ . The stacked Monte Carlo top mass templates are shown in section 4.1.4.5, while Figure 4.4 (left) shows once again the top mass distributions in the region of  $120 \text{ GeV} < M_{\ell\nu b} < 230 \text{ GeV}$  (not stacked histograms).

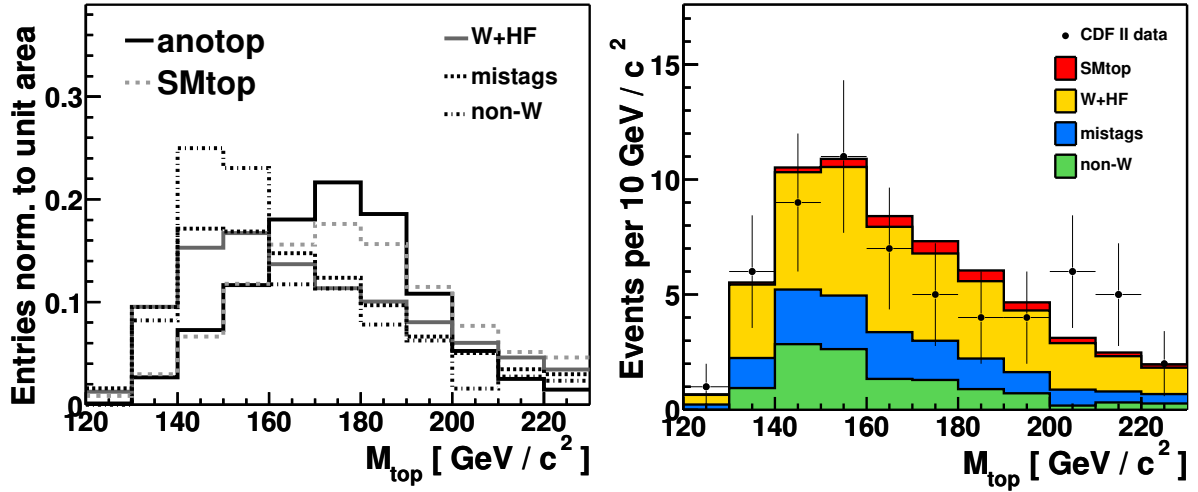


Figure 4.4: On the left: Top mass distributions of the signal and background processes in the region of  $120 \text{ GeV} < M_{\ell\nu b} < 230 \text{ GeV}$ . On the right: Data versus stacked Monte Carlo templates weighted by the number of expected events.

In Figure 4.4 (right) we show the data versus stacked Monte Carlo templates weighted by the number of expected events.

### 4.2.1 Likelihood Function

In the next step we define a maximum likelihood function for the top mass distribution and the number of events in the 1-tag-bin. Five signal and background processes are considered and numbered by the index  $j$  and are shown in Table 4.22: The cross sections  $\sigma_j$  enter

Process	anomalous top	SM top	W+HF	mistags	non-W
Index $j$	1	2	3	4	5

Table 4.22: Signal and background processes considered in the likelihood function.

as normalized parameters  $\beta_j = \sigma_j / \sigma_{SM,j}$  in the likelihood function. The normalization is with respect to the Standard Model expectation  $\sigma_{SM,j}$ . For the anomalous top channel we assume a  $\sigma_{ano} = 1.0 \text{ pb}$ , see section 4.1.4.2, since there is no Standard Model expectation. In order to have a comparance to other possible cross section values, we also set  $\sigma_{ano} = 5.0 \text{ pb}$  and  $\sigma_{ano} = 10.0 \text{ pb}$ . The  $\beta_j$  of the backgrounds are constrained by Gaussian priors  $G(\beta_j, 1.0, \Delta_j)$ . The cross section uncertainties  $\Delta_j$  are given in Table 4.23. For this

Process	anomalous top	SM top	W+HF	mistags	non-W
Errors on $\sigma$	0	0.1	0.18	0.22	0.21

Table 4.23: Cross section uncertainties for each process.

analysis we used approximately the same systematic uncertainties as used in the single

top analysis [61], but it has to be mentioned that they are not reliable. Since our purpose is to get an idea of the limit for our cross section, we will use these values nevertheless and correct them in a future and more improved analysis. Seven categories of systematic uncertainties are considered:

- parton distribution functions (PDF)
- initial state radiation (ISR)
- final state radiation (FSR)
- jet energy scale
- the top quark mass
- the choice of Monte Carlo generator
- trigger and identification efficiencies and the luminosity

The relative strength of a systematic effect due to the source  $i$  is parametrized by the variable  $\delta_i$ . Systematic effects influence the acceptance as well as the shape of the top mass distribution. The  $\pm 1\sigma$  changes in the acceptance of process  $j$  due to an effect  $i$  are denoted by  $\epsilon_{ij+}$  and  $\epsilon_{ij-}$ . The numerical values of those parameters for the signal are given in Table 4.24. For backgrounds most of the systematic uncertainties are absorbed

Syst. Sources	PDF	ISR	FSR	jet energy scale	top mass	generator	acceptance
$\epsilon_{ij+}$	0.05	0.01	0.02	0.03	0.02	0.05	0.1
$\epsilon_{ij-}$	0.05	0.01	0.02	0.07	0.02	0.05	0.1

Table 4.24: Systematic uncertainties for the signal.

into the cross section uncertainties  $\Delta_j$ . In total, the likelihood function  $L$  has 12 variables and is given by:

$$L_s(\beta_1, \dots, \beta_5) = \left\{ \prod_{k=1}^B \frac{e^{-\mu_k} \cdot \mu_k^{n_k}}{n_k!} \right\} \cdot \prod_{j=1}^5 G(\beta_j, 1.0, \Delta_j) \cdot \prod_{i=1}^7 G(\delta_i, 0, 1) \quad (4.9)$$

where  $s$  denotes the signal process, which is the anomalous top quark production. The  $\mu_k$  are the mean number of events in bin  $k$  of the top mass histogram. All variables except of the signal cross section  $\beta_s$  are considered nuisance parameters and are constrained to their expected values by Gaussian functions  $G(x, x_0, \sigma_x)$ . The parameter  $\mu_k$  is defined as follows:

$$\mu_k = \sum_{j=1}^5 \beta_j \cdot \nu_j \cdot \left\{ \prod_{i=1}^7 (1 + |\delta_i| \cdot (\epsilon_{ij+} H(\delta_i) + \epsilon_{ij-} H(-\delta_i))) \right\} \quad (4.10)$$

Here  $\nu_j$  are the acceptances for process  $j$  in the 1-tag-bin.  $H$  denotes the Heavyside function, needed to incorporate asymmetric errors. Systematic source number 7 comprises uncertainties due to the trigger efficiency, lepton identification efficiency, b-tagging



efficiency and luminosity measurement, which are added in quadrature and define  $\epsilon_{7j}$ . Since all these uncertainties contribute only to the normalization (the number of expected events), they do not change the template distribution.

To obtain the probability distribution  $p(\beta_s)$  for the signal cross section  $\beta_s$ , we first integrate out all nuisance parameters (i.e. all variables except  $\beta_s$ ) from the likelihood function  $L_s(\beta_1, \dots, \beta_5)$  and thereby construct the marginalized likelihood  $L_s^*(\beta_s)$ , which only depends on the signal cross section.

### 4.2.2 A-priori Limits

To obtain a measure for our a-priori sensitivity we perform Monte Carlo experiments based on the assumed signal cross sections (1.0 pb, 5.0 pb, 10.0 pb). For each experiment we calculate the 95% C.L. (confidence level) upper limit. We define the median of all Monte Carlo experiments as our sensitivity. We obtain:

- $\sigma_{apriori}^{95} = 19.54$  pb ( $\beta_{apriori}^{95} = 19.94$ ) for the assumption of  $\sigma_{ano} = 1.0$  pb
- $\sigma_{apriori}^{95} = 24.9$  pb ( $\beta_{apriori}^{95} = 5.13$ ) for  $\sigma_{ano} = 5.0$  pb
- $\sigma_{apriori}^{95} = 30.1$  pb ( $\beta_{apriori}^{95} = 3.08$ ) for  $\sigma_{ano} = 10.0$  pb

The a-priori sensitivity for each  $\sigma_{ano}$  value are shown in Figure 4.5.

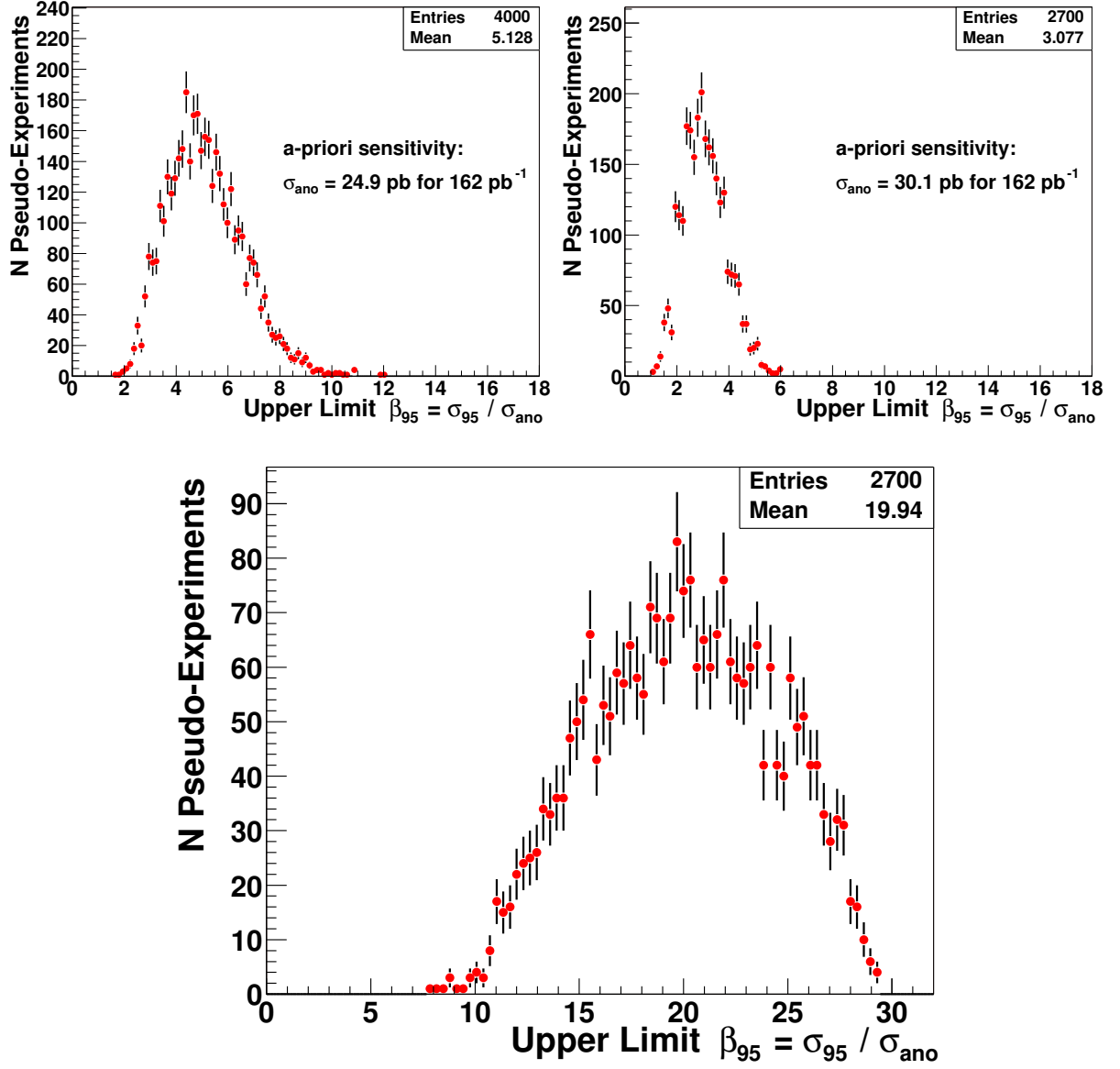


Figure 4.5: A-priori sensitivity for  $\sigma_{ano} = 5.0$  pb (top left), for  $\sigma_{ano} = 10.0$  pb (top right) and for  $\sigma_{ano} = 1.0$  pb (bottom).

In Figure 4.6 the most probable value (MPV), an alternative measure to sensitivity, is presented. MPV is the distribution of the maxima of the likelihood function.

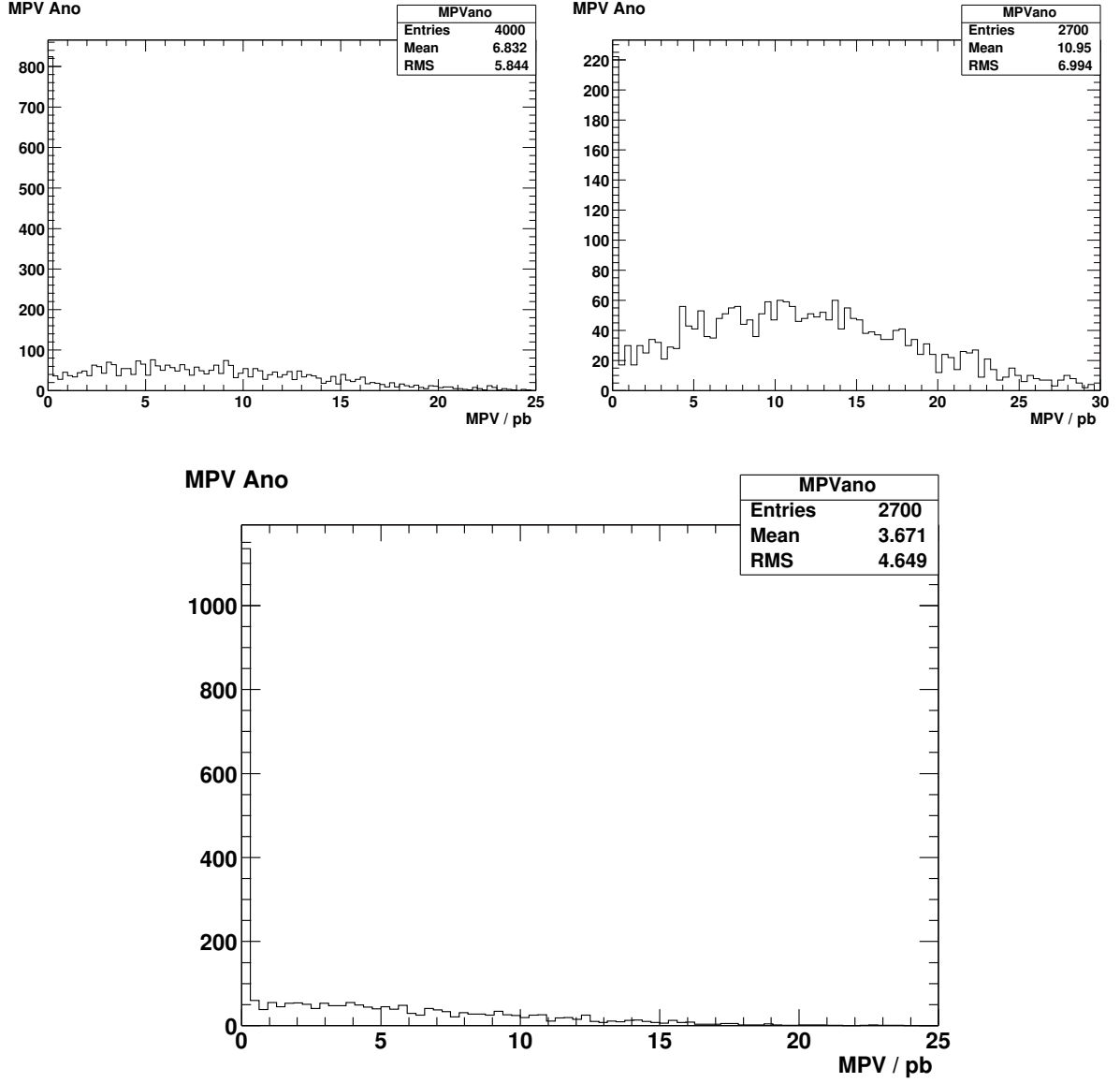


Figure 4.6: The most probable value for  $\sigma_{ano} = 5.0$  pb (top left), for  $\sigma_{ano} = 10.0$  pb (top right) and for  $\sigma_{ano} = 1.0$  pb (bottom).

### 4.2.3 Data

The resulting probability density  $p(\beta_s)$  for CDF II data are shown in Figure 4.7. The maxima of the probability densities give the most probable values for the cross sections. The maximum of the anomalous top quark production occurs at negative values for  $\sigma$ . Since this is not a physical solution, we interpret the maximum as 0 pb and then set upper limits on the cross section of the anomalous top quark production. To obtain the upper limit, we integrate the probability density from 0 to a value  $\sigma_{ano}^{95}$  for which the

integral is 0.95. We call  $\sigma_{ano}^{95}$  the upper limit on the cross section of the anomalous top quark production at 95% C.L. We find an upper limit of 14.7 pb at 95% C.L.

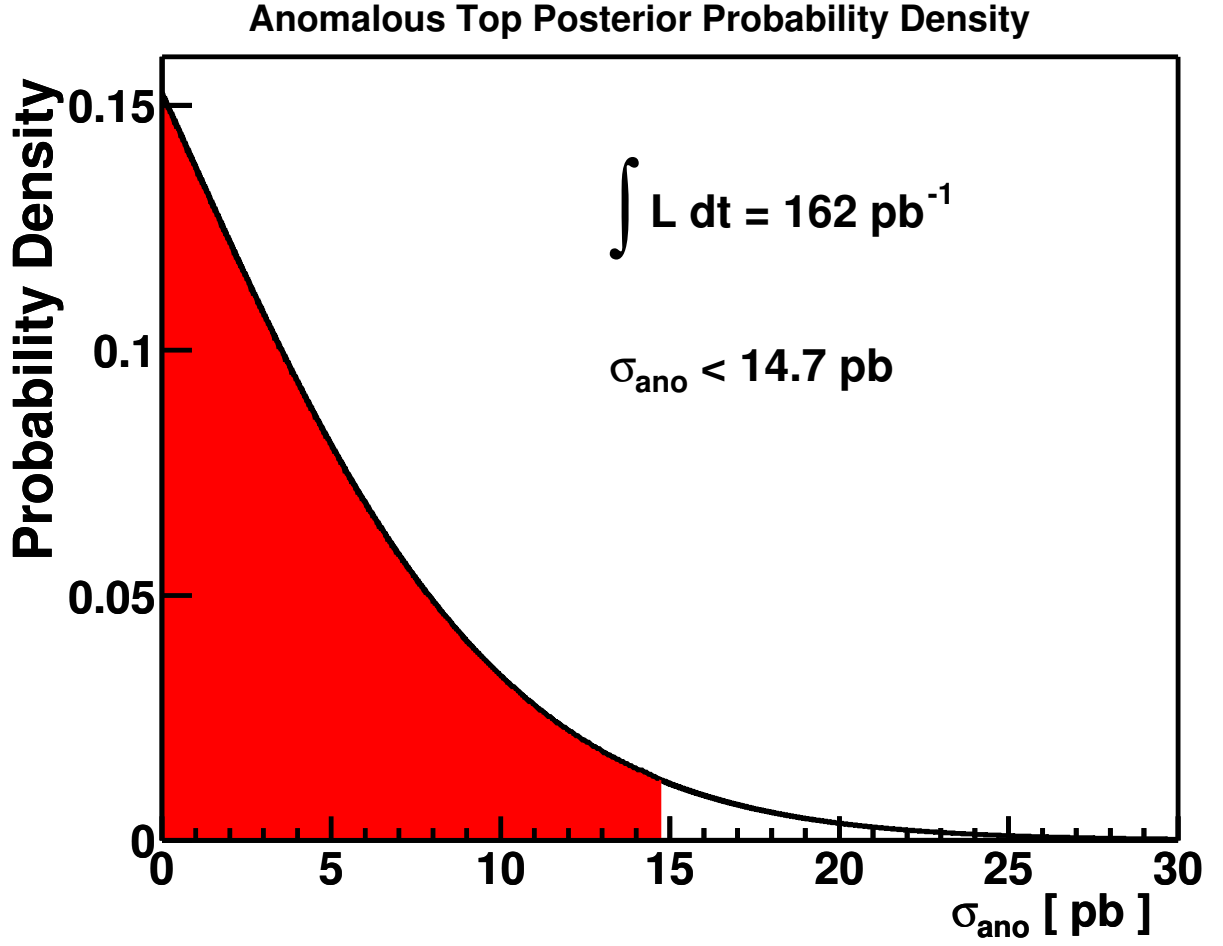


Figure 4.7: Posterior probability density for the anomalous top quark production.

# Chapter 5

## Conclusion and Outlook

In this diploma thesis we searched for the anomalous FCNC top production mode  $u+g \rightarrow t$  in  $162 \text{ pb}^{-1}$  of CDF II data, motivated by theoretical predictions to find clues for new physics, this means physics beyond the Standard Model. Our aim was to set an upper limit on the  $u+g \rightarrow t$  production cross section, which would allow the deduction of an upper limit for  $\kappa_u/\Lambda$  in a future analysis.

We first studied the anomalous process at parton level by modifying the excited up quark process that was already implemented in the Monte Carlo event generator PYTHIA, since  $u+g \rightarrow t$  was not contained in the SM interactions at tree level. Through a certain modification, suggested by the main author of PYTHIA T. Sjöstrand, we managed to simulate the anomalous process correctly. We proved this by comparing the top mass distribution and the decay polarization to the corresponding ones of the SM channels. As expected, the latters were found similar, so we concluded that the PYTHIA event generator would be a useful tool for our purposes.

After applying the PYTHIA code to the CDF software we were able to simulate our anomalous process in the detector. Assuming the same background as used for the single top analysis (including the single top channels), we searched within a variety of kinematic distributions in order to find a proper variable that would be able to best distinguish our signal from the background. The promising variable  $Q \cdot \eta$  (charge of lepton times pseudorapidity) in the parton study had to be rejected, since it lost its potential after including detector simulation. Therefore, we turned to the top mass distribution which seemed to be appropriate in the region of  $120 < M_{\ell\nu b} < 230 \text{ (GeV/c}^2\text{)}$ . We applied our cuts taking this into account and searched for anomalous FCNC ( $u+g \rightarrow t$ ) events in that area, following the method used by the single top group. We found that the number of expected events was  $1.035 \pm 0.050$  for the anomalous top production (assuming  $\sigma_{ano}^{\text{theo}} = 1.0 \pm 0.0 \text{ pb}$ ), while the total background amounted  $61.334 \pm 7.22$  events in the 1-jet-bin.

In the last step of our analysis, we used a maximum likelihood technique developed by the single top group, in order to extract the signal content. We considered five signal and background processes and seven systematic uncertainties (taken from the single top analysis) and so came up with 12 parameters, included in the likelihood function. We set a-priori limits by performing Monte Carlo experiments based on three assumed values for signal cross sections (1.0 pb, 5 pb, 10 pb) since there is no theoretical prediction for the cross section of the anomalous top quark production. Further on, we searched in a CDF II data sample and found an upper limit of 14.7 pb at 95% C.L. on the cross section of  $u+g \rightarrow t$ . This value makes sense considering the SM single top limits for

Tecatron energies [62]. We expect more promising results at higher integrated luminosity and especially at the LHC (CERN).

The next step would be to use the information of the upper limit on the cross section in order to extract the upper limit on  $\kappa_u/\Lambda$ . This is possible and can be easily obtained in a future analysis.

# Bibliography

- [1] *Phys. Rev. D* 50, 2966 (1994).
- [2] *Phys. Rev. Lett.* 73, 225 (1994).
- [3] *Phys. Rev. Lett.* 74, 2632 (1995)
- [4] Th. Müller:  
*'Die Suche nach den Fundamentalen Bausteinen der Natur',*  
*Talk given at the 'Physik am Samstag'-lecture series in Karlsruhe, Germany (2003).*
- [5] M. Kobayashi and T. Maskawa:  
*'CP Violation in the Renormalizable Theory of Weak Interaction';*  
*Prog. Theor. Phys.* 49 (1973) 652.
- [6] Grzadkowski, J.F. Gunion, and P. Krawczyk:  
*Phys. Lett. B* 268, 106 (1991).
- [7] G.Eliam, J.L. Hewett and A. Soni:  
*Phys. Rev. D* 44, 1473 (1991).
- [8] M.Luke and M.J. Savage:  
*Phys. Lett. B* 307, 387 (1993).
- [9] G. Couture, C. Hamzaoui and H. König:  
*Phys. Rev. D* 52, 1713 (1993).
- [10] Jorge L. Lopez, D.V. Nanopoulos and Raghavan Rangarajan:  
*Phys. Rev. D* 56, 3100 (1997).
- [11] T.P. Cheng and M. Sher:  
*Phys Rev. D* 48, 3484 (1987).
- [12] W.S. Hou:  
*Phys. Lett. B* 296, 179 (1992).
- [13] L.J. Hall and S. Weinberg:  
*Phys. Rev. D* 48, 979 (1993).
- [14] D. Atwood, L. Reina and A. Soni:  
*ibid.* 53, 1199 (1996).
- [15] C.T. Hill:  
*Phys. Lett. B* 266, 419 (1991); 345, 483 (1995).

- [16] B. Holdom:  
*ibid.* 339, 114 (1994); 351, 279 (1995).
- [17] H. Georgi, L. Kaplan, D. Morin and A. Schenk:  
*Phys. Rev. D* 51, 3888 (1995).
- [18] X. Zhang:  
*Phys. Rev. D* 51, 5309 (1995).
- [19] J. Berger, A. Blotz, H.-C. Kim and K. Goeke:  
*ibid.* 54, 3598 (1996).
- [20] T. Han, K. Whisnant, B.-L. Young and X. Zhang:  
*Phys. Lett. B* 385, 311 (1996).
- [21] Ehab Malkawi and Tim Tait, 'Top-Charm Strong Flavor-Changing Neutral Currents at the Tevatron', October 1995  
*hep-ph/9511337* (1995).
- [22] M.Hosch, K.Whisnant and B.-L.Young:  
'Direct top quark production at hadron colliders as a probe of new physics',*Phys.Review D*56(1997)9.
- [23] Tim M.P. Tait and C.-P. Yuan:  
'Single Top Production as a Window to Physics Beyond the Standard Model'  
*hep-ph/0007298* (2000).
- [24] E. Kolb, M. Turner:  
'The Early Universe, Addison Wesley (1990).
- [25] S. Eidelman et al.:  
'Review of Particle Physics', *Phys. Lett. B* 592, 1 (2004),  
Available at <http://pdg.lbl.gov> .
- [26] T.Sjöstrand et al.: *Comp. Phys. Commun.* 135, 238 (2001);  
*hep-ph/0108264*.
- [27] M.Beneke, I.Efthimiopoulos, M.L.Mangano, J.Womersley:  
'Top Quark Physics', to appear in the Report of the 1999 CERN Workshop on SM physics (and more) at the LHC.
- [28] K.Hagiwara et al.:  
*Phys. Rev. D* 66, 010001 (2002).
- [29] B.Tweedie et al.:  
'A Study of Simulated Measurements of W-Boson Helicity in the Decay  $t \rightarrow Wb$  at CDF', October 2002.
- [30] D.Amidei et al.: 'W polarization sensitivity studies',*CDF Note 6969*(2004).
- [31] The CDF II Collaboration:  
*The CDF II Detector Technical Design Report,*  
*FERMILAB-PUB-96-390-E.*



- [32] T.Nelson:  
*The CDF Layer 00 Detector, CDF Note 5780.*
- [33] COT group, A. Mukherjee, R. Wagner:  
*CDF Central Outer Tracker, CDF Note 6267.*
- [34] H. Frisch, M. Shochet, G. Sullivan, D. Toback, J. Wahl, P. Wilson, M. Campbell:  
*Conceptual Design of a Deadtimeless Trigger for the CDF Trigger Upgrade, CDF 2038 (1994).*
- [35] H.Bachacou et al.,  
*CDF Note 6084:  $t\bar{t}$  Event Selection and Detection Efficiency for Winter 2003 Lepton + Jets Analyses.*
- [36] P. Nason, S. Dawson and R.K. Ellis:  
*Nucl. Phys. B 327, 607-633, 1988.*
- [37] W.Beenakker, H. Kuijf, W.L. van Neerven and J. Smith:  
*Phys. Rev. 40, 54-82, 1989.*
- [38] R. Bonciani, S. Catani, M.L. Mangano and P. Nason:  
*Nucl. Phys. B 529, 424, 1998.*
- [39] M.Cacciari, S. Frixione, M.L. Mangano, P. Nason and G. Ridolfi:  
*hep-ph/0303085, 2003.*
- [40] E.L. Berger and H. Contopanagos:  
*Phys. Rev. D 57, 253-264, 1998.*
- [41] N. Kidonakis and R. Vogt:  
*Phys. Rev. D 68, 114014 (2003), hep-ph/0308222.*
- [42] B.W. Harris et al.:  
*Phys. Rev. D 66, 054024 (2002).*
- [43] T. Stelzer, Z. Sullivan and S. Willenbrock:  
*Phys. Rev. D 56, 5919 (1997);*  
*Phys. Rev. D 58, 094021 (1998).*
- [44] J.M. Campbell and R.K. Ellis:  
*Update on vector boson pair production at hadron colliders,*  
*Phys. Rev. D 60, 113006 (1999).*
- [45] H.Bachacou, J. Nielsen and W. Yao:  
*Optimized Measurement of the  $t\bar{t}$  Production Cross Section in the SECVTX Tagged Sample,*  
*CDF note 6902, Version 3.0, March 2004.*
- [46] : F.Maltoni and T.Stelzer, hep-ph/0208156.  
*T.Stelzer and W.F. Long, Phys. Commun. 81 (1994) 357-371.*

- [47] : M.L. Mangano, M. Moretti, F. Piccinini, R. Pittau, A. Polosa:  
*ALPGEN, a generator for hard multiparton processes in hadronic collisions,*  
*JHEP 0307:001,2003, hep-ph/0206293.*
- [48] E. Thomson et al.:  
*CDF Note 5947: Top and ElectroWeak Event Classification Module for CDF Run II.*
- [49] C.Ciobanu, Th. Junk, Th. Müller, P. Savard, B. Stelzer, W. Wagner, Th. Walter:  
*Event detection efficiency for single top events in CDF,*  
*CDF Note 7057 (2004).*
- [50] C.Ciobanu, Th. Junk, Th. Müller, P. Savard, B. Stelzer, W. Wagner, Th. Walter:  
*Non-Top Background Estimate for Single Top in  $162 \text{ pb}^{-1}$ ,*  
*CDF Note 7062 (2004).*
- [51] E.J. Weinberg et al.:  
*Review of Particle Physics, Phys. Rev. D 66, 010001-284.*
- [52] Y.-K. Kim, J. Nielsen, L. Tompkins, G. Veramendi:  
*Trigger Efficiencies for High  $P_T$  Electrons, CDF Note 6234, Version 3.1 (2004).*
- [53] M. Coca, E. Halkiadakis, S. Lockwitz:  
*Central Electron Identification Efficiencies for the  $200 \text{ pb}^{-1}$  Run 2 Dataset,*  
*CDF Note 6580 (2004).*
- [54] V. Martin and L. Cerrito:  
*Muon Cuts and Efficiencies for 4.11 Analyses, CDF Note 6825, Version 0.1 (2004).*
- [55] W.K. Sakumoto and A. Hocker:  
*CDF Note 6331: Event  $|Z_{vtx}| \leq 60 \text{ cm}$  Cut Efficiency for Run II.*
- [56] H. Bachacou, W. Yao, T. Wright:  
*CDF Note 6904, Version 1.3,*  
*Efficiency of SecVtx B-Tag Used for 2004 Winter Conferences.*
- [57] D. Amidei et al.:  
*CDF Note 6329:*  
*Measurement of the  $p\bar{p} \rightarrow t\bar{t}$  cross section in the  $\ell + \text{jets}$  SECVTX tagged sample.*
- [58] B.W. Harris et. al.:  
*Phys. Rev. D 66, 054024 (2002).*
- [59] Z. Sullivan:  
*hep-ph/0408049.*
- [60] C. Ciobanu, T. Junk, Th. Müller, P. Savard, B. Stelzer, W. Wagner, Th. Walter:  
*CDF Note 7106,*  
*Likelihood Function for Single Top Search with  $162 \text{ pb}^{-1}$ .*
- [61] CDF collaboration: *CDF Note 7129,*  
*Search for electroweak single-top-quark production in  $p\bar{p}$  collisions at  $1.96 \text{ TeV}$ .*

- [62] By CDF Collaboration (D. Acosta et al.):  
*SEARCH FOR ELECTROWEAK SINGLE TOP QUARK PRODUCTION IN P  
ANTI-P COLLISIONS AT  $S^{*}(1/2) = 1.96\text{-TEV}$ ,  
FERMILAB-PUB-04-340-E, Oct 2004. 7pp.  
Submitted to Phys.Rev.Lett.  
e-Print Archive: hep-ex/0410058.*

# Appendix A

## Appendix

About the helicity angle  $\theta^*$  (note that the angle is mentioned as  $\alpha$  in the thesis): Helicity is the projection of spin along the direction of motion. This is defined by the helicity operator:  $H = \vec{\sigma} \cdot \hat{p}$ . Helicity value for the  $W$  left and right-handed ( $\vec{\epsilon}_L$  and  $\vec{\epsilon}_R$ ) polarization states are then -1 and +1, respectively (transverse  $W$ ). Assume that the direction of motion is  $\hat{z}$ , then a  $W$  with a polarization of  $\vec{\epsilon}_z$  has helicity 0 (longitudinal  $W$ ). Squares of the various helicity amplitudes:

$$|\mathcal{M}(W_{h=-1}^+)|^2 = |\mathcal{M}(W_{h=+1}^-)|^2 = \frac{1}{4} (1 - \cos \theta^*)^2 \quad (\text{A.1})$$

$$|\mathcal{M}(W_{h=+1}^+)|^2 = |\mathcal{M}(W_{h=-1}^-)|^2 = \frac{1}{4} (1 + \cos \theta^*)^2 \quad (\text{A.2})$$

$$|\mathcal{M}(W_{h=0}^+)|^2 = |\mathcal{M}(W_{h=0}^-)|^2 = \frac{1}{2} (1 - \cos^2 \theta^*) \quad (\text{A.3})$$

The angle  $\theta^*$  is defined as the angle between charged-lepton momentum in  $W$  rest frame and the  $W$  momentum in the top rest frame: Explicitly:

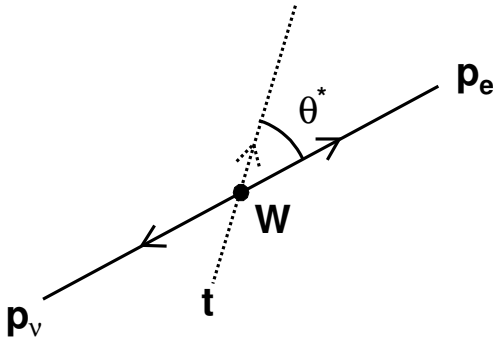


Figure A.1: helicity angle  $\theta^*$ .

$$\cos \theta^* = \frac{\vec{p}_\ell^W \cdot \vec{p}_W^{top}}{|\vec{p}_\ell^W| \cdot |\vec{p}_W^{top}|} \quad (\text{A.4})$$

Figure A.2 shows the different variables which were tested in the detector simulation in order to determine their capability in distinguishing the signal from the background. From top to bottom and left to right:

- jet1Et stands for the transverse energy of the first jet
- bJetEt stands for the transverse energy of the b jet
- HT stands for the scalar transverse energy sum
- eta-top stands for the pseudorapidity of the top quark
- lepEt stands for the transverse energy of the lepton
- jet1Eta stands for the pseudorapidity of the first jet
- Weta stands for the pseudorapidity of the W boson
- topPt stands for the transverse momentum of the top quark

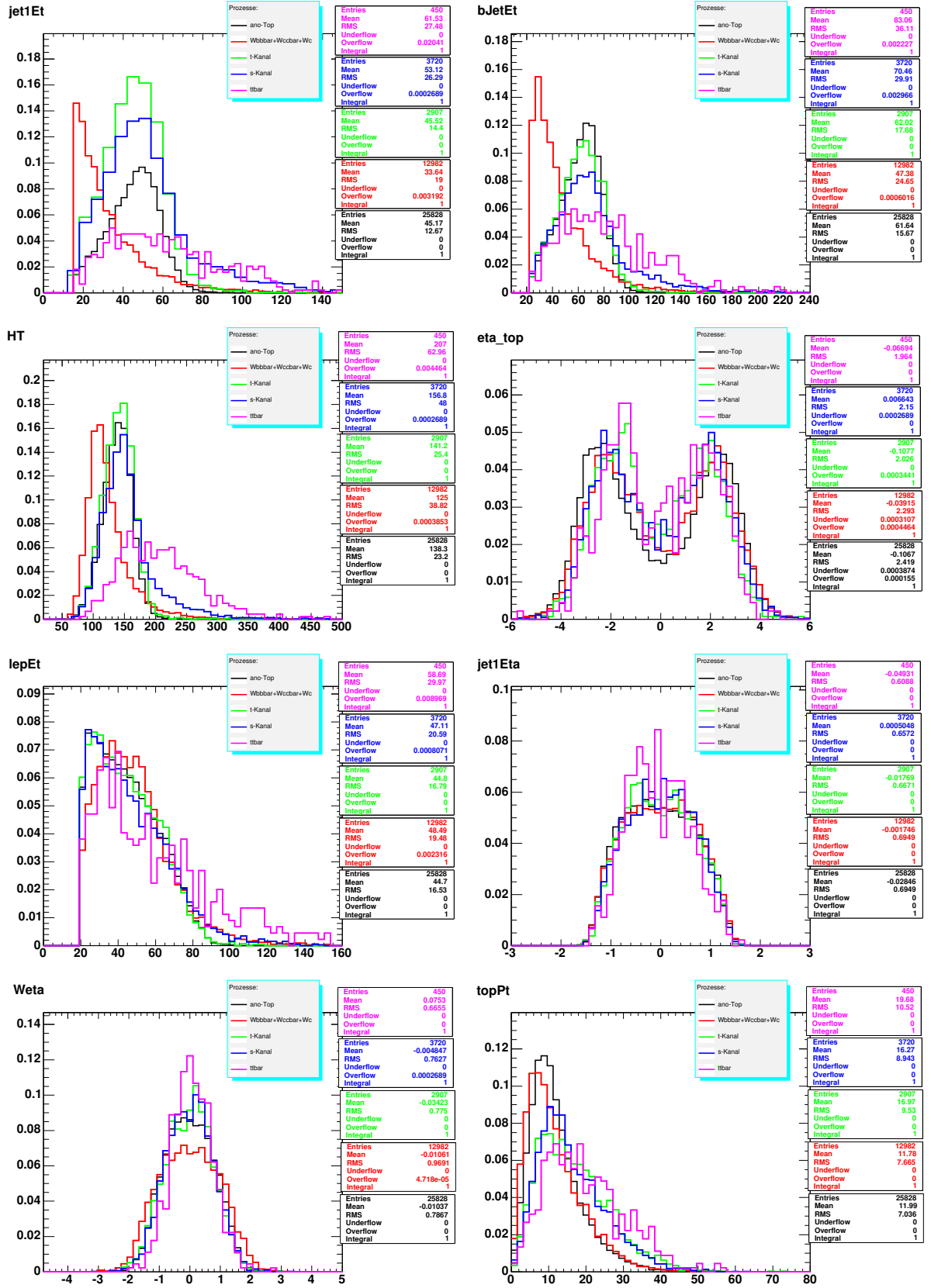


Figure A.2: Some of the variables that were at first considered as possible for the fit, see section 4.2.

# Danksagung

Ich möchte mich an dieser Stelle bei allen bedanken, die zur Vollendung dieser Diplomarbeit beigetragen haben.

Zuerst will ich mich bei Herrn Prof. Dr. Thomas Müller bedanken, der mich in seine 'Top'(-Quark)-Gruppe aufgenommen hat und damit mir die Möglichkeit gegeben, mich mit einem so interessanten Thema zu beschäftigen. Obwohl ich am Anfang der Diplomarbeitszeit meine Zweifel hatte, ob die Analyse geeignet für meine Kenntnisse wäre, habe ich während der Durchführung neue Sachen kennengelernt, was dazugeführt hat, dass ich neue Interessen im Bereich der Physik entwickelte. Das habe ich hauptsächlich Herrn Müller zu verdanken, der mich jede Woche mit seinen Fragen und Kommentaren während den Sitzungen der Arbeitsgruppe motivierte.

Ich wollte Herrn Prof. Dr. Michael Feindt dafür danken, dass er das Korreferat übernommen hat und mich für die etwas verspätete Abgabe der Arbeit bei ihm entschuldigen.

Herrn Professor Dr. Dieter Zeppenfeld möchte ich für seine Beireitschaft danken, die theoretische Aspekte meiner Diplomarbeit zu diskutieren.

Besonders möchte ich mich bei Dr. Wolfgang Wagner bedanken, der mich während der Durchführung der Diplomarbeit betreut hat. Ohne seine Geduld und Kenntnisse wäre alles bestimmt schwieriger, wenn nicht unmöglich, für mich zu schaffen. Der war stets für mich da gewesen, wenn ich Fragen hatte und hat mir weitergeholfen in Momenten, wo alles so hoffnungslos aussah.

Dominic "Du kannst mich immer fragen" Hirschbühl möchte ich für die wunderbare Atmosphäre im Zimmer danken. Der hat immer Zeit für meine Fragen jeglicher Art gehabt und hat mir wichtige Ratschläge gegeben.

Yves " $6 \times 7 = 42$ " Kemp möchte ich sowohl für eine schöne Atmosphäre im Zimmer, als auch für die gute Musik aus Chicago danken. Der hat mich mit seinem Sinn für Humor und seinen Kenntnissen in *linux* in meinen dunklesten Zeiten erleichtert.

Matthias Kirsch möchte ich ebenfalls für eine angenehme Atmosphäre in den ersten Monaten der Einarbeitungszeit danken. Der hat mir sowohl bei technischen als auch bei Anpassungsproblemen geholfen und meinen Respekt als Mensch erworben.

Thorsten "... " Walter möchte ich für seine Hinweise und Hilfe danken. Zusätzlich für die inspirierende Atmosphäre im Zimmer.

Jan Lück danke ich für eine freundliche Atmosphäre in und ausserhalb des Instituts. Die Zeit mit ihm hat mich weitergebracht als Persönlichkeit.

Andreas "machst Du 'ne Pause?" Glatt möchte ich sowohl für die schönen und inspirierenden Diskussionen, als auch für das Schach-spielen in den Pausen danken.

Ich möchte mich auch bei den anderen Mitglieder der Top-Gruppe bedanken, die mich bei meiner Arbeit auf irgendeiner Weise unterstützt haben: Prof. Dr. Martin Erdmann, Svenja Richter und Thorsten Scheidle.

Des Weiteren bedanke ich mich beim gesamten EKP-Institut für die aussergewöhnlich angenehme Atmosphäre und Freundlichkeit der Kollegen. Besonders danke ich Frau Weissmann für ihre organisatorischen Anstregungen und Höflichkeit, den Systemadministratoren für die funktionsfähige Computerinfrastruktur und schliesslich den Kollegen, mit denen ich sportliche Aktivitäten wie Basketball und Fussball unternommen habe.

Für die Korrekturvorschläge dieser Diplomarbeit will ich folgenden Personen danken: Wolfgang, Dominic, Yves, Jan und Andreas. Sie haben allesamt die Diplomarbeit wesentlich verbessert.



Ausserhalb von der Universität wurde ich von einer Menge von Leuten ebenfalls unterstützt und diesen danke ich auch. Das sind meine Freunde hier und in Griechenland. Insbesondere danke ich Φωτεινή dafür, dass sie mich in guten und schlechten Zeiten unterstützt und glücklich gemacht hat.

Meinen Eltern danke ich sowohl für die moralische als auch für die finanzielle Unterstützung im Leben. Diese Diplomarbeit wäre nie realisiert, wenn sie nicht ständig dafür gesorgt hätten, dass mir nichts fehlt.

Meinem Bruder danke ich für seine Hilfe und seine Inspirierung in allen für mich wichtigen Bereichen des Lebens.

Hiermit versichere ich, die vorliegende Arbeit selbständig verfasst und nur die angegebenen Hilfsmittel verwendet zu haben.

Adonis Papaikonomou

Karlsruhe, 12. Januar 2005